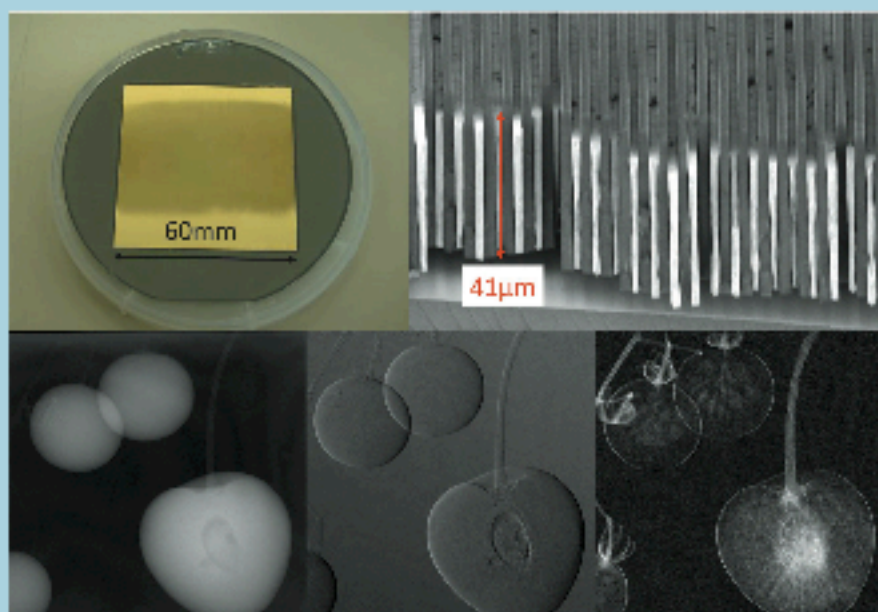


# LASTI Annual Report

*Laboratory of Advanced Science & Technology for Industry  
University of Hyogo*

Vol.11 (2009)



## PREFACE

This annual report reviews the research activities of the Laboratory of Advanced Science and Technology for Industry (LASTI) in the academic year of 2009 (April 2009 –March 2010) including activities using a 1.5GeV synchrotron radiation facility “ NewSUBARU ” at the site of Spring-8 and other research activities of the micro and nanoscale are carried out energetically in CAST building.

Topics of the NewSUBARU research activities of this year are as follows. First is the basic characteristic research of NewSUBARU electron storage ring and imaging with laser Compton scattering Gamma-ray. The second is EUV (extreme ultraviolet) activities that are a mask observation using a coherent EUV scattering microscope, nanostructure pattern replication by newly developed EUV interference lithography system, and development of new EUV resist with low LER(Line edge Roughness). BL09C beamline was branched from BL09B beamline for usage of the EUV interference lithography for evaluation of the exposure characteristics of EUV resist. Third is micro- and nano-devices such as a high-aspect ratio micro-coil, three-dimensional lab-on-CD and X-ray grating for X-ray Talbot interferometer. Fourth is the material science for various materials such as hydrogenated DLC, a-C:H and BN.

Furthermore, the performance of analysis beam line BL5 for industrial enterprises was evaluated by NEXAFS spectra measurements using the standard samples of graphite, BN, LiCl and MgO.

Most of our research activities are being conducted in collaboration with industries, government research institutes and other universities.

We will continue to respond to the community’s demand by offering new science and technologies.



A handwritten signature in black ink that reads "S. Matsui". The signature is written in a cursive, flowing style.

Shinji Matsui  
Director of LASTI

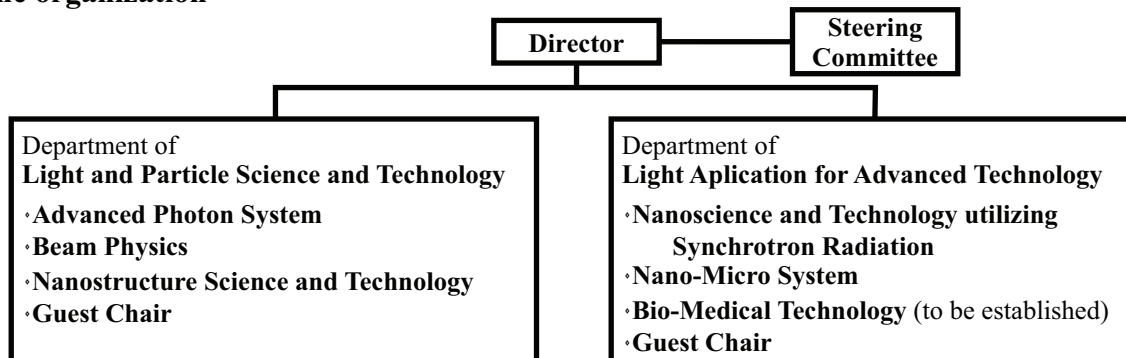


# CONTENTS

<b>PREFACE</b> .....	i
<b>CONTENTS</b> .....	iii
<b>ORGANIZATION</b> .....	iv
<b>CURRENT STATUS OF NewSUBARU</b>	
<i>NewSUBARU Storage Ring</i> .....	1
<i>Beamlines</i> .....	2
<i>Improvement of beam injection using the injection bump waveform monitor at NewSUBARU</i> .....	9
<i>Development of automatic tune measurement and correction system at NewSUBARU storage ring</i> .....	11
<b>RESEARCH ACTIVITIES</b>	
<i>Laser-Compton Gamma-Ray Source by using 2<math>\mu</math>m Tm-Laser</i> .....	13
<i>Imaging for Stress Corrosion Cracking in Stainless Steel with Laser Compton Scattering Gamma Ray</i> .....	15
<i>Study of <math>^{12}\text{C}(\gamma, 2\alpha)^4\text{He}</math> with NewSUBARU laser Compton scattered <math>\gamma</math>-ray beam</i> .....	17
<i>Laser-plasma debris from a rotating cryogenic-solid-Xe target</i> .....	20
<i>Mitigation by argon buffer gas of fast debris from cryogenic xenon laser plasma EUV light source</i> .....	22
<i>Mitigation effect of plasma debris from cryogenic xenon target by argon jet</i> .....	24
<i>Propose of Three-dimensional Micro Fluidics Device Using Centrifugal Force</i> .....	26
<i>Fabrication of electrodes for multiplex neural interface</i> .....	28
<i>Efficiency Microfluidic Reactor Chip Operated only using Surface-Acoustic-Wave</i> .....	30
<i>High-sensitive enzyme-linked immunosorbent assay in three-dimensional lab-on-a-CD</i> .....	32
<i>Mask Observation Results using a Coherent EUV Scattering Microscope at NewSUBARU</i> .....	34
<i>Imaging Performance Improvement of an Extreme Ultraviolet Microscope</i> .....	42
<i>Development of the Extreme Ultraviolet Interference Lithography System</i> .....	50
<i>High-Precision Analysis for Material Analysis Beamline at BL05 for Industrial Enterprises</i> .....	58
<i>Effect of the Soft X-ray on the Highly-Hydrogenated Diamond-Like Carbon Film</i> .....	60
<i>Photoemission Study of Hydrogenated Amorphous Carbon Thin Films as a Function of Annealing Temperature</i> .....	61
<i>Control of Oxygen Contamination in BN Thin Film Prepared by Reactive Magnetron Sputtering</i> .....	63
<i>Semi-quantitative analysis of carbon contamination on MLMs using high power EUV light</i> .....	65
<i>Electronic State of Ti in Ultra-fine Grained SUS316L-1%TiC</i> .....	67
<i>Fabrication of High Aspect Ratio Microcoils</i> .....	69
<i>Fabrication of X-ray Grating Using X-ray Lithography for X-ray Talbot Interferometry</i> .....	71
<i>Fabrication of High Hardness Ni Mold with Electroless Ni-B Thin Layer</i> .....	73
<i>Fabrication of Light Guide Plate for Ultraviolet Range</i> .....	75
<i>Fabrication of Micro Capacitive Inclination Sensor by Resin Molding Method</i> .....	77
<b>LIST OF PUBRICATIONS</b>	
<i>Papers</i> .....	79
<i>International Meetings</i> .....	83
<i>Awards</i> .....	90
<b>ACADEMIC DEGREES</b> .....	91
<b>EDITORIAL BOARD</b> .....	92

# The Organization of Laboratory of Advanced Science and Technology for Industry University of Hyogo

## The organization



## Stuff (FY 2009)

### Research and faculty staff

MATSUI Shinji, Professor, Director  
 MOCHIZUKI Takayasu, Professor  
 MIYAMOTO Shuji, Professor  
 KINOSHITA Hiroo, Professor  
 HATTORI Tadashi, Professor  
 WATANABE Takeo, Associate Professor  
 SHOJI Yoshihiko, Associate Professor  
 NIIBE Masahito, Associate Professor  
 KANDA Kazuhiro, Associate Professor  
 UTSUMI Yuichi, Associate Professor  
 AMANO Sho, Research Associate  
 HASHIMOTO Satoshi, Research Associate  
 HARADA Tetsuo, Research Associate  
 HARUYAMA Yuichi, Research Associate  
 NODA Daiji, Research Associate  
 OHOKUMA Haruo, Professor (Guest)

### Administrative staff

MUREI Masatoshi, General Manager  
 YOSHIDA Yasukazu, Manager  
 MIYAMOTO Ken-ichi, Chief  
 YOKOYAMA Yuka, CAST  
 OGATA Hitomi, CAST  
 UEHIRO Ayumi, CAST  
 KANATANI Naoko, NewSUBARU  
 KAMIYA Miki, NewSUBARU  
 MORIGUCHI Miyuki, Harima Forum of  
 Science and Technology for 21st Century

### Open Advanced Research Facilities Initiative

TERASAWA Mititaka  
 MOTOYAMA Muneyuki  
 KUROZUMI Ryouta  
 MIYAHARA Yoshikazu  
 ISHIKAWA Kazuko

## Contact address

CAST:3-1-2 Kouto, Kamigori-cho, Ako-gun,  
 Hyogo, 678-1205 JAPAN  
 TEL:+81-791-58-0249  
 FAX:+81-791-58-0242  
 NewSUBARU: 1-1-2 Kouto, Kamigori-  
 cho, Ako-gun, Hyogo, 678-1205 JAPAN  
 TEL:+81-791-58-2503  
 FAX:+81-791-58-2504

### Web URL

<http://www.lasti.u-hyogo.ac.jp/>

### e-Mail

[lasti@lasti.u-hyogo.ac.jp](mailto:lasti@lasti.u-hyogo.ac.jp)

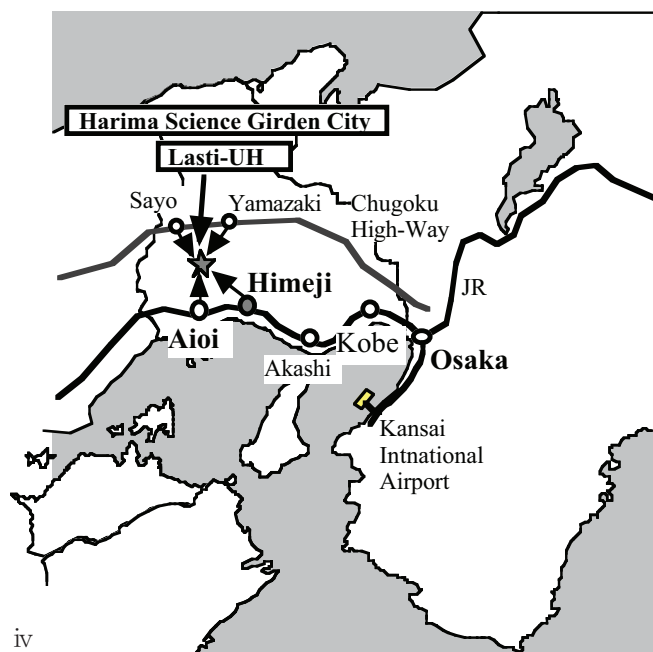
## Access

by JR (railway station)

1. JR Aioi station  
a half hour from Aioi by bus
2. JR Himeji station  
one hour from Himeji by bus

by car

1. 5 min from Harima-Shingu IC on the Sanyo-high-way.
2. 30 min from Yamazaki or Sayo IC on the Chugoku high-way.



# **Current Status of NewSUBARU**



# NewSUBARU Storage Ring

Y. Shoji

## Storage Ring Parameters

The machine parameters of the 1.5 GeV storage ring remain the same as those of the previous year. They are listed in Table I.

Table I Main parameters of the NewSUBARU storage ring in FY2009.

Circumference	118.73 m
Bending lattice type	modified DBA
Number of bending cells	6
Straight sections	4m X 4, 15m X 2
Bending radius	3.22 m
Injection energy	1.0 GeV
Maximum energy	1.5 GeV
RF frequency	499.955 MHz
Betatron tune	6.30 (H), 2.21 (V)
Momentum compaction factor	0.0014
Electron energy	1.0 GeV 1.5 GeV
RF voltage	140 kV 260 kV
Natural energy spread	0.047% 0.072 %
Natural emittance	38 nm 67 nm
Maximum beam current	500 mA

## Operation Status

The ring has two user-time operation modes, 1.0 GeV top-up operation mode and 1.5 GeV operation mode. Basic operation time is 9:00 - 21:00 of weekdays. Monday is for machine R&D, Tuesday is for 1.5 GeV user time, Wednesday and Thursday are for 1.0 GeV top-up user time, Friday is for 1.0 GeV or 1.5 GeV user time. Night period or weekend is used for machine study and user time with the special mode, single bunch operation and Laser-Compton Gamma ray, if necessary.

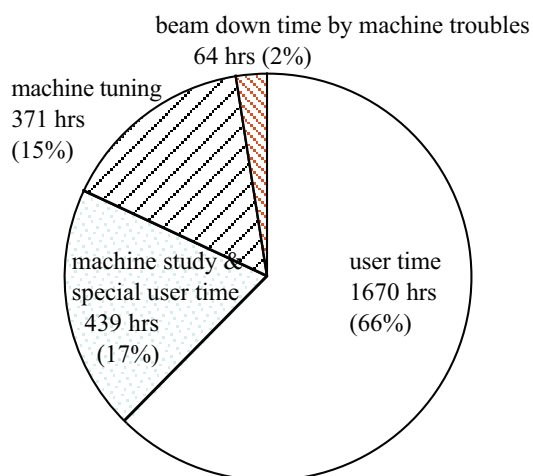


Fig. 1 Operation time in FY2009.

The total operation time in FY2009 was 2544 hrs, 105% of that of FY2008, including the beam down time. Fig. 1 shows the breakdown. The beam down time includes not only the down by a failure, but also off-beam periods by a beam abort or others due to the beam instability. The normal user time in this FY, 1670 hrs, was about 109% of that in FY2008. Time for machine study and special users was 80% of that in FY2008.

## Machine Troubles

The machine troubles in FY2009 are listed in Table II. Many of sources of the failures in FY2008 were eliminated. The biggest failure was a vacuum break down by a miss-operation at BL09.

## Machine Study and Special User Time

Table III shows the list of machine studies in FY 2009. One special theme, a research related to a production of Laser-Compton backscattering  $\gamma$ -ray and its use, took about 1/3 of the machine study time.

Most of the study reports are open to the public on the home page of NewSUBARU.

## Accelerator Improvements

The ring had several improvements in FY2009.

Bunch current monitor, installed in FY2008 was organized to a new bucket filling control system. It controls the bucket-selector for the injection and realizes a wanted bucket filling.

The wave form monitor system, using LabView, is installed for the pulse bump magnet. The system can detect very rare miss-firing and abnormal wave deformation of pulse magnets.

The KEK-type XBPM was installed at BL10. It monitors vertical x-ray position from the bending magnet. It is expected to give information for the improvement of stability of the synchrotron radiation at beam lines.

The COD correction system started continuous working. It operates slow COD correction routine for every one minutes. The software has many sub-programs, which stops the continuous operation. They automatically stop the COD correction during the rapid injection, during the acceleration, and when the correction does not work properly by unknown reasons.

The visible light port SR5 for beam diagnostics, built in FY2008, was upgraded. It enables the detection of THz radiation at outside of the radiation shield. The corona graph elements were installed as a beam halo monitor.

Table II Machine trouble in FY2009.

Group	Failure/trouble	beam down time (hr)
Operation	Miss-operation	2
	Beam loss by a beam instabilities	3.6
RF	Interlock of circulator arc	0.3
	Interlock of klystron vacuum	6
	Klystron window chiller	1
Beam transport	Orbit feed-back	1
Vacuum	Vacuum leak at BL09	42
Radiation safety	Failure at BL02	2

Table III List of machine studies in FY2009. The unit of study time is counted by shifts (typically 12 hrs).

R&D theme and special user mode	responsible person	study shift
Parameter tuning for 1.5 GeV acceleration	S. Hashimoto	3
Negative alpha-p operation	S. Hashimoto	2
Test of wave form monitor for pulse bump magnets	S. Hashimoto	1
Betatron tune feedback system	S. Hashimoto	6
Test of new COD control system	Y. Minagawa	1
Test of new filling control system	Y. Minagawa	1
Laser-Compton backscattering $\gamma$ -rays (incl. Nuclear Transmutation)	S. Miyamoto	19
Test of bunch-by-bunch feedback system	T. Nakamura	1
Radiation shield for L4BT beam profile monitor	Y. Shoji	1
Vertical beam oscillation at the beam injection	Y. Shoji	1
Commissioning of new profile monitor port SR5	Y. Shoji	2
Commissioning of sextupole windings in the invert bends	Y. Shoji	8
Transverse beam matching at the beam injection	Y. Shoji	7
Effect of the magnetic shield for the DC septum stray field	Y. Shoji	1
Stored current dependence of COD	Y. Shoji	1

# Beamlines

Takeo Watanabe and Hiroo Kinoshita

Total eight beamlines are operating in the NewSUBARU synchrotron facility. Four beamlines of BL01, BL03, BL06 and BL11 were constructed until 1999. Three beamlines of BL07, BL09 and BL10 were started the operation from 2000.

BL03B beamline branched from the BL03 beamline propose for the usage of the EUVL (extreme ultraviolet lithography) microscope for the EUVL finished mask inspection.

BL09B beamline branched from BL09 beamline propose for the usage of the advanced point diffraction interferometry for the test alignment of the EUVL imaging

optics for practice use. Furthermore, BL09C beamline branched from BL09B for the usage of the EUV interference lithography to evaluate and develop EUV resist.

BL02 beamline was constructed for the usage of LIGA in 2003.

BL05 beamline was constructed in response to a demand in the industrial world, that is enhancement of the analysis ability in the soft X-ray region with the development of nanotechnology.

The arrangement of the beamlines in the NewSUBARU synchrotron radiation facility is shown in Fig.1.

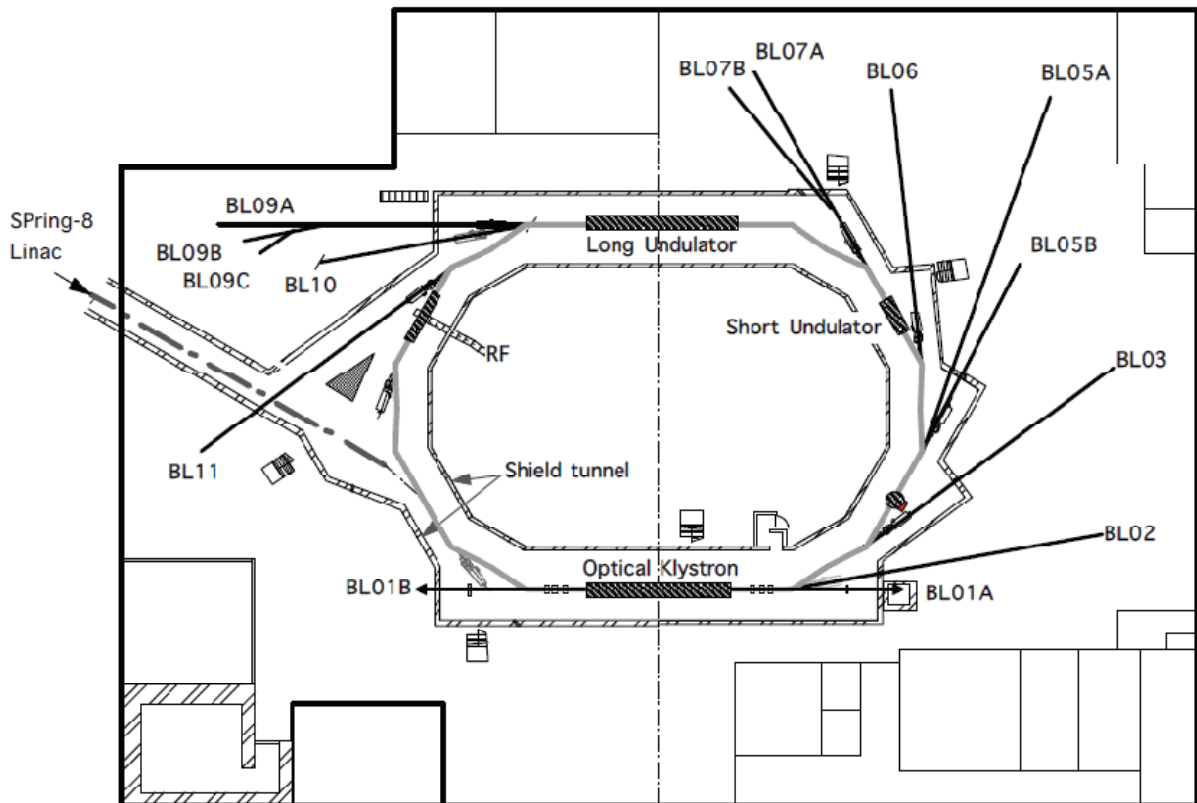


Fig. 1 Beamline arrangement in NewSUBARU.

## I. BL01

BL01 is a beamline for research and developing new light sources. This beamline is one of two long straight section on NewSUBARU. Optical klystron

was installed at this straight section. Upstream side of this beamline (BL01B) is intended to be used for visible and infrared light generated from FEL or SR.

Downstream side of this beamline (BL01A) is used for laser Compton scattering gamma-rays source. Gamma-ray beamline hutch just outside of the storage ring tunnel was constructed in 2004 for

gamma-ray irradiation experiments. Specifications of this gamma-ray source are listed in Table 1.

**Table 1.** Specification of BL01 gamma beam

CO <sub>2</sub> laser 10.52 μm 5W	Gamma energy : 1.7 - 4 MeV Gamma flux* : 9 x10 <sup>6</sup> γ/s : 6 x10 <sup>5</sup> γ/s (1.5-1.7 MeV) (with 3mmφ collimator)
Nd laser 1.064 μm 0.532 μm 5 W	Gamma energy : 17 - 40 MeV Gamma flux* : 7.5 x10 <sup>6</sup> γ/s : 3 x10 <sup>5</sup> γ/s (15-17 MeV) (with 3mmφ collimator)

\*Electron beam energy : 1-1.5 GeV

\*Electron beam current : 250 mA

gamma-ray beam divergence : 0.5 mrad

## II. BL02

The LIGA (abbreviated name of Lithographic, Galvanoformung and Abformung) process which consists from deep x-ray lithography, electroforming, and molding process is one of the promising candidates for such 3D microfabrication. More than hundreds aspect ratio for microstructure can be attained by the use of the higher energy x-rays (4-15 keV) from synchrotron radiation (SR) with deeper penetration depth to the photosensitive resist. In this system we have succeeded to enlarge the exposure area up to A4 size and the fabrication dimension from submicron to millimeter by varying the energy of the x-ray source in accordance with the size of desired microparts. Microstructure with high aspect ratio over several hundreds will be achieved using the x-rays over 10 keV since high energy x-ray has deep penetration depth to the photo-sensitive resist materials. Whereas, in the case of lithography for low energy x-rays from 1 keV to 2 keV, submicron structures with high aspect ratio will be achieved using the x-rays mask with precise line-width and thinner absorber, since low energy x-rays has low penetration depth. Based on this principle, the beamline for x-ray exposure have constructed with continuous selectivity of x-rays from 100 eV to 15 keV by using the

x-ray mirrors (plane and cylindrical mirror) and Be film filters. The horizontal angle of the outgoing SR could be obtained up to 12.5 mrad, which corresponds to the horizontal size of 220 mm (A4 horizontal size) at the exposure position. The second characteristic performance of the beamline is the high efficiency differential pumping system. This was necessary for maintain the vacuum difference between the storage ring (<10<sup>-9</sup> Pa) and the end-station (<10<sup>-9</sup> Pa) at which gasses for substrate cooling will be introduced in the exposure apparatus.

The flexibility for the shapes and functions of microstructure will be enlarged by achieving 3D microfabrication process using multi step exposure at various configuration between x-ray mask and substrates. The relative positions between x-ray mask and substrates, tilt and rotation angle to the SR incident direction can be moved simultaneously during SR exposure using 5 axis stages. The movement of each axis is controlled by the PC in terms of the scanning speeds, scanning length, and repetition number. In order to decrease the heat load of sample substrate suffered during SR irradiation helium introduction and substrate cooling mechanism were also equipped. Specification of spectrometer is listed in Table 2.

**Table 2.** Specification of the LIGA exposure system

Optics	Plane and cylindrical mirror, Be filters
Exposure energy	100 - 2 keV, and 4 - 15 keV
Exposure method	Proximity and multi step exposure
Wafer size	A4 or 8 inch
Exposure area	230 mm(H) × 300 mm(V)
Exposure environment	< 1 atm (He-gas)

### III. BL03

BL03 is a beamline for the developing the next generation lithographic technology so called extreme ultraviolet lithography (EUVL). The exposure tool is installed at the end station. Using this exposure tool, the research and development of the next generation lithography such as the less than 70 nm node is going on process. The exposure wavelength is 13.5 nm.

The semiconductor industry plays a very important role in the information technology (IT). In 2006, 256 Gbit DRAM with a gate length of 70 nm will be demanded in the IT industry. The extreme ultraviolet lithography (EUVL) is a promise technology for fabricating a fine

pattern less than 70 nm. To meet this schedule, this technology has to be developed in the pilot line until 2004. As for the practical use, it is very important that both to achieve large exposure area and to fabricate fine patterns. Therefore, at Himeji Institute of Technology, large exposure field EUV camera consists of three aspherical mirrors was developed. First in the world, we fabricated 60 nm line and space pattern in the large exposure area of 10 mm×10 mm on a wafer. Furthermore, BL03B beamline branches from the BL03 beamline propose for the usage of the EUVL microscope for the EUVL finished mask inspection.

**Table 3.** Specification of the exposure tool (ETS-1)

Imaging optics	Three aspherical mirrors
Exposure wavelength	13.5 nm
Numerical aperture	0.1
Demagnification	1/5
Resolution	60 nm
Depth of focus	0.9 μm
Exposure area (static)	30 mm×1 mm
Exposure area (scanning)	30 mm×28 mm
Mask size	4 inch, 8 inch, and ULE 6025
Wafer size	8 inch
Exposure environment	In vacuum

### IV. BL05

BL05 was constructed in response to a demand in the industrial world, that is enhancement of the analysis ability in the soft x-ray region with the development of nanotechnology. BL05 consists of two branch lines for use in the wide range from 50 eV to 4000 eV. BL05A and BL05B are designed to cover the energy range of 1300-4000 eV and 50-1300 eV, respectively. The incident beam from the bending magnet is provided for two branch lines through different windows of a mask. Therefore, these two branch lines can be employed simultaneously.

1) The double crystal monochromator was installed at the BL05A. InSb crystals and Si crystals are prepared for a double-crystal monochromator. Toroidal mirrors are used as a pre-mirror and a focusing mirror of BL05A. XAFS measurement in the total electron yield mode and fluorescence XAFS measurement using SSD (SII Vortex) can be performed. The fluorescence XAFS spectra can be measured for samples at the end station filled with He gas.

**Table 4.** Monochromator specification

Monochromator	Double crystal monochromator
Monochromator crystals	InSb(111), Si(111)
Energy range	1300-4000 eV
Resolution	$E/\Delta E=3000$

2) The constant-deviation monochromator consisting of a demagnifying spherical mirror and a varied-line-spacing plane grating (VLSPG), which can provide high resolution, simple wavelength scanning with fixed slits, was mounted on BL05B. The optical system consists of a first mirror

(M0), a second mirror (M1), an entrance slit (S1), a pre-mirror (M2), and three kinds of plane grating (G), an exit slit (S2) and a focusing mirror (M3). The including angle of the monochromator is 175°. Two measurement chambers are prepared at the end station of BL05B. The

XAFS spectra in the total electron yield mode and fluorescence XAFS spectra using SDD (EDAX) can be measured in a high vacuum chamber. In addition, the photoelectron spectrum can be measured using spherical

electron analyzer (VG Sienta, R3000) in an ultra high-vacuum chamber. The chambers can be replaced by each other within 1 hour.

**Table 5.** Monochromator specification

Monochromator	Varied-line-spacing plane grating monochromator
Grating	100 l/mm, 300 l/mm, 800 mm/l
Energy range	50-1300 eV
Resolution	$E/\Delta E=3000$

#### V. BL06

BL06 has been mainly developed for irradiation experiments such as photochemical reaction, SR-CVD, photo-etching, surface modification. The white radiation beam from bending magnet is introduced to the sample stage using a pair of mirror, whose incident angle was  $3^\circ$ . The SR at BL06 sample stage had a continuous spectrum from IR to soft x-ray, which was lower than 1 keV. A

differential pumping system can be utilized for experiments in a gas atmosphere, which is difficult in the soft x-ray region. A sample holder can install four pieces of samples at a time. By using heater set in the sample holder, the sample can be heated from room temperature to 220°C. The temperature of sample is monitored using a Cr-Al thermocouple mounted on the sample holder.

#### VI. BL07A and BL07B

This beamline was designed for the development of new materials by SR technology. This beamline consists of two branch lines, which are provided with an incident beam from a 3-m undulator by switching the first mirror. One of them is a high photon-flux beamline with a multilayered-mirror monochromator for the study of SR-process (BL07A) and another is a high-resolution beamline with a varied line spacing grating monochromator for the evaluation of nano-structure characteristics by SR-spectroscopy (BL07B). The useful range of emitted photons from 50 to 800 eV is covered at both beamlines. The light source of BL07 is a 3-m length planar undulator, which consists of 29 sets of permanent magnets, a period length of which is 76 mm. The incident beam from the undulator is provided for two branch lines by translational switching of first mirror.

##### 1) BL07A

The multilayered-mirror (MLM) monochromator, which has high reflectivity in the soft X-ray region, was installed at the BL07A. It consists of a switching mirror chamber, a slit chamber, a MLM monochromator, a filter chamber and a reaction chamber. To obtain a large photon flux, we decided to use only first mirror (switching mirror), M0, for focusing. The MLM monochromator is designed to cover an energy range of up to about 800 eV by combination of three kinds of mirror pairs with 4 kinds of filter. The flux delivered by this design is estimated to be between a maximum of  $10^{17}$  photons/s at 95 eV and a minimum  $2 \times 10^{14}$  photons/s at 300 eV for a 500 mA ring current.

**Table 6.** Summary of BL07A.

Energy range (eV)	Multilayer mirror					Filter	
	Material	spacing	Thickness Ratio	number of layers	$\Delta E/E$	material	thickness
50-60	Mo/Si	20 nm	0.8	20	6.2 %	Al	100 nm
60-95						None	—
90-140	Mo/B <sub>4</sub> C	11 nm	0.5	25	3.3 %	Ag	100 nm
140-194						Cr	500 nm
190-400	Ni/C	5 nm	0.5	60	2.5 %	Ni	500 nm
400-560							
550-800							

## 2) BL07B

The constant-deviation monochromator consisting of a demagnifying spherical mirror and varied line spacing plane grating (VLSPG), which can provide to high resolution, simple wavelength scanning with fixed slits, was mounted on BL07B. The optical system consists of a first mirror (M0), a entrance slit (S1), a premirror (M1), and three kinds of plane grating (G), an exit slit (S2) and a

focusing mirror (M2). The monochromator is designed to cover the energy range 50-800 eV with three gratings, of which including angle are 168°. The VLSPG has been well known to obtain high resolution in extreme ultraviolet region by diminishing various kinds of aberration. The total resolving power about 3000 can be realized in the whole energy region.

**Table 7.** Monochromator specification

Mount type	Hettrick-Underwood type
Grating G1, G2, G3	Plane VLS (600 l/mm, 1200 l/mm, 2400 l/mm)
Energy range	50-150 eV, 150 – 300 eV, 300-800 eV
Resolving power (E/ Δ E)	~3000

## VII. BL9

A purpose of this beamline is studies on a soft x-ray interferometry or a holographic exposure experiment with making use of highly brilliant and coherent photon beams radiated from 11 m long undulator in NewSUBARU.

BL09 consists of M0 mirror, M1 mirror, G grating and M2 and M3 mirror. M0 and M3 mirrors are used for horizontal deflection and beam convergence, M1 is used for vertical beam convergence at the exit slit, and M2 is used for vertical deflection and beam convergence. A monochromator is constructed by M1 and a plane grating. The maximum acceptance of the undulator beam is 0.64 mrad in horizontal and 0.27 mrad in vertical. The

acceptance can be restricted by 4-jaw slits equipped at upstream of the M0 mirror.

BL09B beamline branched from BL09 beamline for the usage of the advanced point diffraction interferometry for the test alignment of the EUVL imaging optics for practice use.

BL09C beamline branched from BL09B beamline for the usage of the EUV interference lithography for the evaluation of the exposure characteristics of EUV resist. Coherence length of 1 mm at the resist exposure position was achieved using BL09C beamline.

**Table 8.** Monochromator specification

Mount type	Hettrick-Underwood type
Grating	Plane VLS (900 l/mm)
Energy range	50 – 600 eV
Resolving power (E/ Δ E)	~3000

**Table 9.** Specification of the BL09 End Station

Function	Extreme ultra-violet (EUV) point diffraction interferometry
Sample	EUV imaging optics. Presently, Schwarzschild optics.
Beam size	80(w) x 120(h) μ m
Degree of Vacuum	$5 \times 10^{-4}$ Pa (differential evacuation system, upstream)
Photon number	$1.2 \times 10^{13}$ photons/sec, at 95 eV, Ie=40mA

## VIII. BL10

BL10 is for the global use in the Himeji Institute of Technology. M0 mirror is used for horizontal deflection and beam convergence, M1 is used for vertical beam convergence at the exit slit, and M2 is used for vertical deflection and beam convergence. A monochromator is

constructed by M1 and a plane grating. At the beginning, the multilayers reflectivity measurement was carried out at this beamline. The characteristics of this beamline and the result of the Mo/Si multilayers measurement are carried out for the development of the EUVL mask

technology.

BL10 utilizes a monochromator of the varied line spacing plane grating monochromator (VLS-PGM). The line density of the monochromator in central region of the grating is 600 lines/mm. The reflectometer is a two axis vacuum goniometer using two Huber goniometers. One axis carries the sample, which may for example be a mirror at the center of the reflectometer vacuum tank

( $\theta$ -motion). The other ( $\varphi$ -motion) carries the detector on a rotating arm. In addition there are through-cacuum linear motions to translate the sample in two orthogonal directions (x,y). All motors are controlled by computer. The sample itself is mounted on a kinematic holder. The controlstage monochromator rotation, and data analysis were program using LABVIEW software. The reflectivity result obtained at BL10 has a good agreement with that at LBNL.

**Table 10.** Monochromator specification

Mount type	Hettrick-Underwood type
Grating	Plane VLS (600 l/mm)
Energy range	50 – 600 eV
Resolving power (E/ $\Delta$ E)	$\sim$ 1000

### IX. BL11

A beam line BL11 is constructed for exposure Hard X-ray Lithography (DXL) in the LIGA (German acronym for Lithographite Galvanoformung and Abformung) process. LIGA process, that utilizes a useful industrial application of SR, is one of the promising technologies for fabrication of extremely tall three-dimensional microstructures with a large aspect ratio. This process was invented at the Institut Fur Mikrostrukturtechnik (IMT) of the Karlsruhe Nuclear Center (KfK) in 1980. Microstructures with height of over a few hundreds  $\mu$ m have been widely applied to various fields such as micro-mechanics, micro-optics, sensor and actuator technology, chemical, medical and biological engineering, and so on. This beam line was designed by the criteria ; photon energy range 4 keV to 6 keV, a beam spot size on the exposure stage  $\geq 50 \times 5$  mm<sup>2</sup>, a density of total irradiated photons  $\geq 10^{11}$  photons/cm<sup>2</sup>. BL11 of an absorber chamber, a first-mirror chamber (M1), a second-mirror chamber (M2), a 4-way slit chamber, a Be window chamber, and an exposure chamber. The second pre-mirror is bent elliptically using a bending mechanism.

Fine bending adjustment of the M2 mirror can be made in the UHV by the pulse motor. The LIGA process needs the photon energies of 3 keV to 6 keV, the optics of a LIGA beam line generally employ a Pt monolayered-mirror and a Be window, which cuts off low-energy photons. The reflectivity of a Pt-coated mirror is about 55 % in the range of photon energy from 2 keV to 4 keV, however, it drops to 30 % at the photon energy of 6 keV. Therefore, new materials with a high reflectivity must to be found for Deep X-ray lithography (DXL) in this energy range. We propose the use of a Ni/W/C multilayered-mirror with a graded d-spacing in the range of photon energy from 3 eV to 6 keV. The calculated reflectivity of the Ni/W/C multilayered-mirror is higher than 56 % at the photon energy of 6 keV with a glazing incident angle of 0.8 degrees, and photons that have higher photon energy than 6 keV can be removed A 200  $\mu$ m-thick beryllium (Be) window in a Be window chamber is used to separate the ultra-high vacuum part from the low vacuum part and to cut off low-energy photons.

**Table 11.** Specification of the LIGA exposure system

Exposure method	Proximity exposure
Wafer size	4 inch
Exposure area	50 mm(H) $\times$ 80 mm(V)
Exposure environment	< 1atm (He-gas)

# Improvement of beam injection using the injection bump waveform monitor at NewSUBARU

S. Hashimoto, T. Shinomoto<sup>#</sup>, Y. Minagawa<sup>#</sup>, S. Miyamoto  
 LASTI, University of Hyogo  
<sup>#</sup>JASRI / SPring-8

## Abstract

Although stable beam injections are necessary for the top-up operation of a storage ring, timing jitters and misfires were often observed in injection bump waveforms in NewSUBARU storage ring. Using a bump waveform monitor, we could find that timing jitters come from a timing signal module. By replacing this module, timing jitters can be drastically reduced from 1.9 % to 0.2 %. And no misfire of bump waveforms is observed now, although it occurred about ten times a day before. We are now always watching the waveforms of injection bump magnets by this monitor system to keep the stable top-up operation.

## Introduction

In the NewSUBARU facility the top-up operation has been performed in the 1.0 GeV user time. The efficiency of beam injection has to be stably high for keeping the stored current constant. To realize this purpose, many kinds of stabilities are required, that is, stabilities of injection beam from linac, a pulse septum magnet, and injection bump magnets and so on.

In general, electron beams are injected to a storage ring using four pulse magnets called “bump” magnets, which make closed orbit of circulating beams at the injection point to shift horizontally for a very short period so that a beam from an injector can be successfully injected.

In the NewSUBARU storage ring, the number of beam injection exceeds over one thousand a day. Looking at bump waveforms in detail, little discrepancies in waveforms can be found. We developed bump waveform monitor [1,2] to watch bump waveforms. In this paper we report the improvement of the timing jitter and the misfire of bump waveforms by using this monitor.

## Injection bump waveform monitor system

To get bump waveforms, an oscilloscope (Agilent TDS3054B) acquires monitor outputs of power supplies for bump magnets as shown in Fig. 1. Signals are externally triggered with beam injection pre-trigger signal. The oscilloscope is connected to a GPIB-Ethernet converter. A PC in the control room can communicate with the oscilloscope through local area network.

A software program developed with LabVIEW acquires, inspects in real-time and saves waveform data (Fig. 2). The other program analyzes each waveforms saved in PC and makes statistical analysis. This program can calculate a rise time (10-90%), peak-height, peak-position of each wavelength and show these distributions. Because bump is a high-voltage and pulsed magnet, acquired signals may be noisy. For noise reduction, data smoothing can be used

before waveform analyzing.

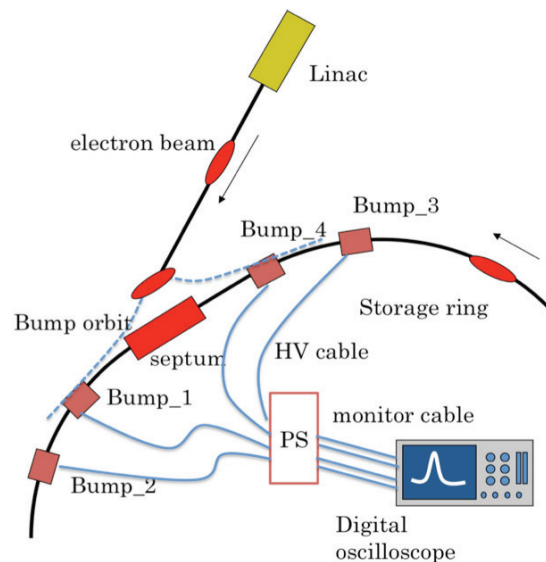


Fig.1. Electron beam injection from the SPring-8 linac to the NewSUBARU storage ring using four bump magnets.

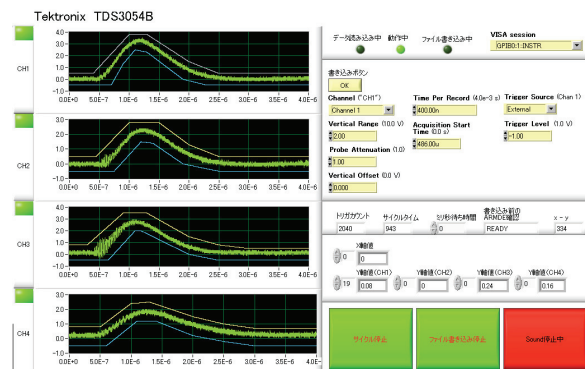


Fig.2. Front panel of the program for data acquisition, real-time inspection and data save.

### Finding a trouble source with the monitor

The timing jitter and the misfire of bump waveforms may come from those of timing signals, in addition to failures of power supplies for bump magnets. To find the trouble source in timing signals, we checked signals from several NIM modules such as counter, FAN in/out, logical delay, and so on with the waveform monitor. The upper and lower limits in the monitor are correctly configured for testing digital signal waveforms.

As results, we found that a counter module (508 MHz, 30 bit counter) was a trouble source. After the new module replaced this one, no misfire of trigger signal from the module was observed.

### Improvement of timing jitter of bump waveform

Peak-height, peak-position (timing jitter) and rise-time before and after the replacement of the troubled counter module are shown in Fig. 3. Standard deviations of these distributions are also shown in Table. I.

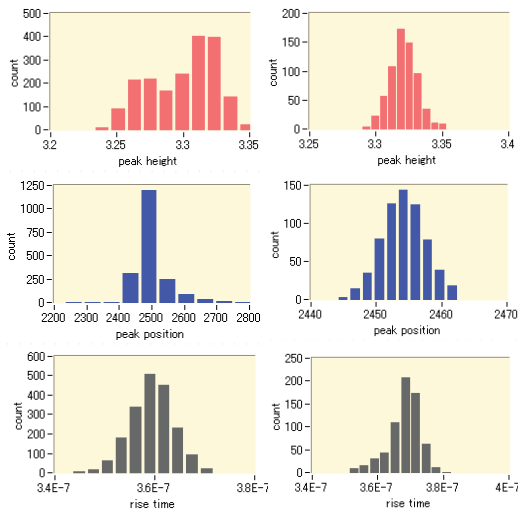


Fig.3. Discrepancies of bump waveforms in one day. Peak-height (top), peak-position (middle) and rise-time (bottom) are shown before (left) and after (right) replacement of the counter module. After the replacement, timing jitters of bump waveforms were drastically reduced.

Standard deviation (%)	Before	After
Peak position	1.9	0.2
Peak height	0.8	0.3
Rise time	1.2	0.9

Table I. Standard deviation of peak-position, peak-height and rise-time of bump waveforms before and after the replacement of the troubled timing module.

Although the standard deviation of peak-position was 1.9 % before the replacement, after the replacement its distribution became very

narrow and its standard deviation was 0.2 %. Thus the timing jitter was drastically improved by replacement of the troubled module.

### Improvement of misfire of bump waveform

Although no misfire was observed at the new module after the replacement, misfire of bump waveforms was still observed about ten times a day. However, misfire of bump magnets suddenly disappeared in March 2010. We suspicious that it was due to some troubles in the other modules or a loose connection of cables.

### Summary

Various kinds of high stabilities are necessary for the stable top-up operation of storage rings. In the NewSUBARU storage ring we could find the source of timing jitter and misfire of bump waveform using the bump waveform monitor. By replacing the troubled timing module, the jitter becomes drastically small. Although misfire of the bump waveform was observed about ten times a day after the replacement, this suddenly disappeared. The reason may be due to the other timing module or a loose connection of cables, etc.

Now we are always watching bump waveforms during user operation using the bump waveform monitor. If there is something wrong in beam injection, quick search of trouble sources and quick recovery can be possible.

### References

- [1] T. Shinomoto *et al.*, Proc. of Particle Accelerator Society of Japan, (2009).
- [2] S. Hashimoto *et al.*, LASTI Annual report, vol.9, (2009).

# Development of automatic tune measurement and correction system at NewSUBARU storage ring

S. Hashimoto, Y. Hamada, Y. Minagawa<sup>#</sup>, T. Shinomoto<sup>#</sup>, S. Miyamoto  
 LASTI, University of Hyogo  
<sup>#</sup>JASRI / SPring-8

## Abstract

The automatic measurement and correction system for betatron tunes has been developed in NewSUBARU electron storage ring. Tunes are evaluated by analyzing beam signals from a beam position monitor. If differences between measured tunes and desired ones are large, tunes are automatically corrected using winding coils for ring quadrupole magnets Q1, Q2. We have successfully demonstrated that tune shifts can be suppressed using the system during an energy ramping.

## Introduction

One of important parameters of a storage ring is betatron tune, i.e., the number of horizontal or vertical oscillations of stored electron beams around a closed orbit during one turn of the ring circumference. If tunes are not correctly adjusted, some troubles in the operation of storage rings, including degradation of beam lifetime, beam loss by instabilities, may occur.

In NewSUBARU electron storage ring, horizontal and vertical tunes are 6.30 and 2.23, respectively. However, tunes vary according to stored beam current and filling pattern. And during energy ramping from 1.0 to 1.5 GeV,

fluctuations of electron beam orbit and tunes are relatively large. Sometimes these cause slight or critical beam losses.

To make the energy ramping stable, we have developed an automatic tune measurement and correction system. In this paper we report the system and experimental results of the automatic tune correction during energy ramping.

## Automatic tune measurement system

The automatic tune measurement system is shown in Fig. 1. Horizontal and vertical betatron tunes are measured by BPM (beam position monitor) signals. We use a difference

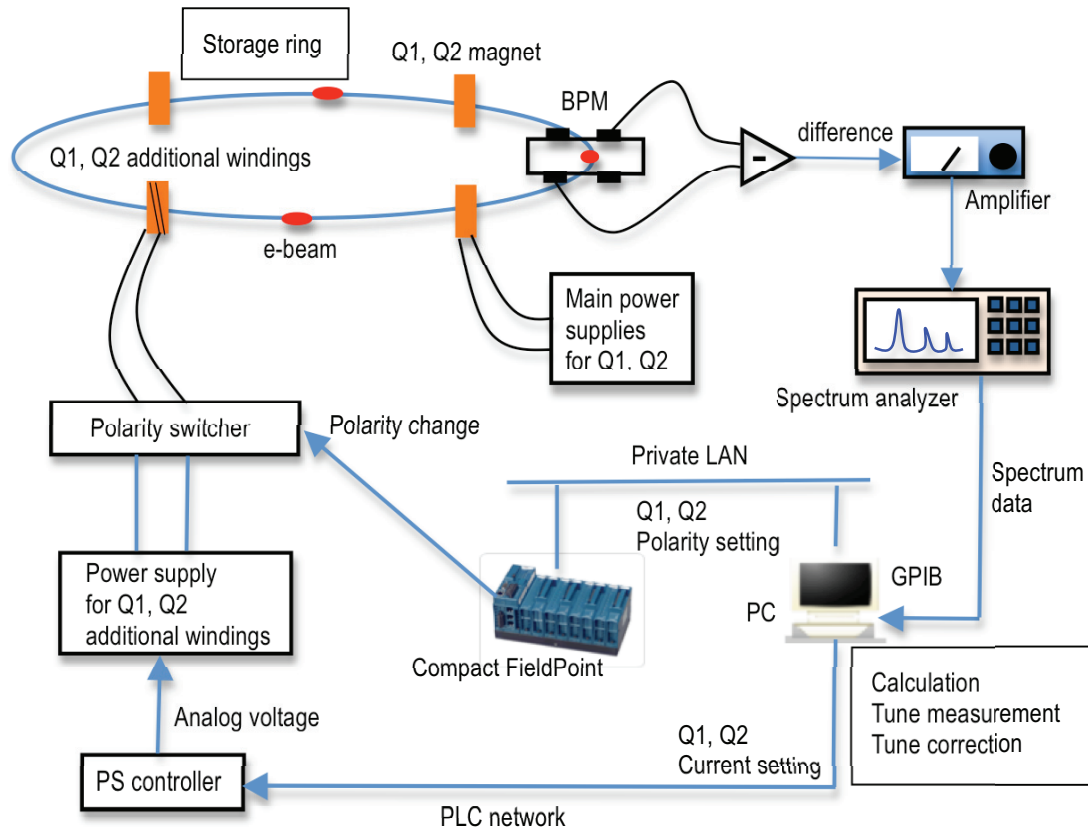


Fig. 1. Automatic tune measurement and correction system.

between signals from two diagonal electrodes of a BPM. The difference signal is analyzed in frequency domain by a spectrum analyzer. Spectrum data is transferred to a PC via GPIB. At the PC, the LabVIEW application program automatically detects two signal peaks around RF frequency and evaluates horizontal and vertical tunes in every 50 msec. Because the raw data for spectrums is relatively noisy, we use both averaging and smoothing methods in the signal processing. The measured tune values can be saved to a database every one second.

### Automatic tune correction system

The configuration of the automatic tune correction system is also shown in Fig. 1. In the NewSUBARU storage there are seven families of quadrupole magnets. For tune corrections we used two families Q1 and Q2. Additional windings are equipped to Q1, Q2 magnets and additional power supplies feed current to these winding coils. A correction program on the PC calculates tune shift  $\Delta v_x$  and  $\Delta v_y$  which are differences from nominal values. Then currents fed to Q1, Q2 winding coils are given by the following equations:

$$I_{Q1} = E*(4.58E5*\Delta v_x + 6.03E4*\Delta v_y) + I_{Q1(old)},$$

$$I_{Q2} = E*(7.00E4*\Delta v_x + 5.06E4*\Delta v_y) + I_{Q2(old)},$$

where E is beam energy,  $I_{Q1}$ ,  $I_{Q2}$  are currents fed to Q1, Q2 winding coils, respectively. The above equations were evaluated by comparing kick strength by additional winding coils and results of lattice calculations.

The PC sends calculated values of  $I_{Q1}$  and  $I_{Q2}$  to the controller every one second via a PLC network. The controller generates the equivalent analog voltage, by which power supplies for Q1

and Q2 windings are externally controlled.

To correct tunes both positively and negatively, the power supplies should be bi-polar. We used mono-polar power supplies with a polarity-switcher, which includes relay circuits and can control polarity according to external control signals, which are given by National Instruments Compact FieldPoint.

### Tune correction during energy ramping

Measured tunes during energy ramping, which takes about 15 minutes, are shown in Fig. 2. Without tune corrections, variations of horizontal and vertical tunes were about 0.02.

With tune corrections, tune shifts became small and were within 0.005. Thus betatron tunes could be kept almost constant during energy ramp by this system.

### Summary

We have developed the measurement and correction system for betatron tunes in the NewSUBARU storage ring. This system can measure horizontal and vertical tunes every 50 ms and correct tune shifts every one seconds. During energy ramping from 1.0 to 1.5GeV, tunes are successfully corrected within 0.005 with this system.

This system also can correct tune shifts in current decay operations. Furthermore, as applications of this system, an automatic tune survey is possible, which can automatically measure beam lifetime or injection efficiency at various operating points in a tune diagram.

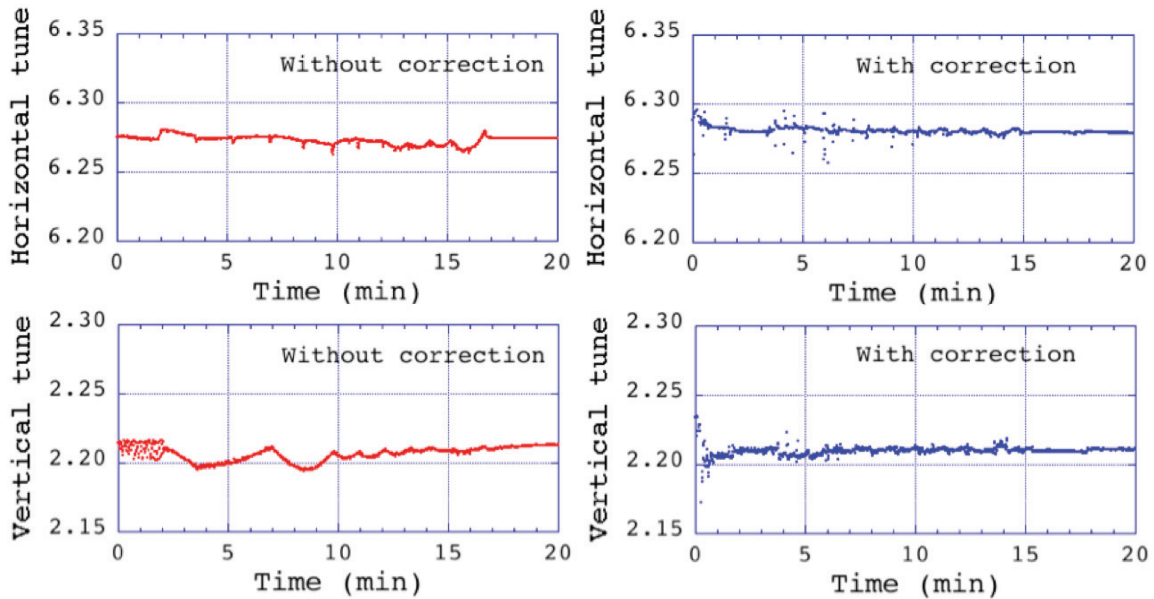


Fig. 2. Horizontal (upper) and vertical (lower) tunes during energy ramp without (left) and with (right) the automatic tune corrections.

# **Research Activities**



# Laser-Compton Gamma-Ray Source by using 2 $\mu$ m Tm-Laser

Sho Amano, Shuji Miyamoto  
LASTI/UH

## Abstract

In order to expand energy range of the Compton gamma-ray, we considered to introduce a Tm-fiber laser operating at 2  $\mu$ m to generate gamma rays in the energy range of 4–21 MeV, using a laser-focusing design to generate the maximum flux. The generated luminosity is calculated to be 6400 photons/(W·mA·s) with a laser power of 4 W and a beam current of 200 mA. This is at the same level as for the Nd:YVO<sub>4</sub>, and CO<sub>2</sub>, laser. Tm-fiber laser is also capable of operating in a high-power regime and can generate kW-level output power. At present, the maximum gamma-ray flux is limited only by the laser power. When operating the laser at 1 kW of output power with a beam current of 200 mA, we expect a flux of up to  $\sim 10^9$  photons/s. At NewSUBARU, up to several dozen MeV gamma-ray sources are capable of generating such high power.

## Introduction

Initially, we generated gamma rays in the range of 17–37 MeV by using a Nd:YVO<sub>4</sub> laser operating at 1.06  $\mu$ m. The gamma-ray source is used for various studies. Several applications, however, demand gamma-ray energies of several MeV, prompting us to install a CO<sub>2</sub> laser operating at 10.6  $\mu$ m to generate gamma rays in the range of 1–4 MeV. In addition to the Nd:YVO<sub>4</sub> and the CO<sub>2</sub> lasers, the installation of a third laser with a wavelength of approximately 2  $\mu$ m is planned to generate gamma rays in the energy range that is not currently attainable. With the addition of the 2- $\mu$ m laser, we will have the capacity to generate gamma rays with a continuously tunable energy range from 1 to 37 MeV. The Tm-doped fiber laser is a candidate for the 2- $\mu$ m laser. Recently, a high-power Tm-doped fiber laser has been developed with an output power at the kW level. In general, both Nd:YVO<sub>4</sub> and CO<sub>2</sub> lasers are capable of operating in a high-power regime, and output powers exceeding the kW level have already been achieved. Because the laser-Compton gamma-ray flux is proportional to power of the driving laser, these high power lasers make it possible to generate a high flux of gamma rays. Thus, by using the high power lasers, the gamma-ray source in NewSUBARU will be capable of producing a high flux of gamma rays in the energy spectrum from 1 to 37 MeV.

In this paper, we present a theoretical prediction of the performance expected using a 2- $\mu$ m laser.

## Compton gamma-ray beamline (BL1a)

Figure 1 shows the experimental setup of the laser-Compton gamma-ray source in NewSUBARU, which is an electron storage ring with stored energies from 0.7 to 1.5 GeV. Laser-Compton gamma-ray experiments are conducted on one of the straight sections in combination

with beamline 1 (BL1). The Nd:YVO<sub>4</sub> and CO<sub>2</sub> lasers are installed in the experimental hall, and only the beam transport path for the Nd:YVO<sub>4</sub> or CO<sub>2</sub> laser is shown in Fig.1. The beam transport paths for the Nd:YVO<sub>4</sub> and CO<sub>2</sub> laser are called the N-path and the C-path, respectively. The transmittance of each path corresponds to each laser wavelength and each path has an optimized collision point (A or B) for laser beam and electron. Figure 2 shows the RMS size of the electron beam calculated from Twiss parameters, and the laser beam radii ( $1/e^2$ ) in the straight section. To maximize the interaction length, the focusing optic in the N-path of the Nd:YVO<sub>4</sub> laser (1.064  $\mu$ m) is designed to create a laser spot with a radius of 0.5 mm at position A at the center of the straight section, which is one advantage offered by NewSUBARU. At position A, the laser beam collides with the electron beam, which is of nearly equal size. However, in the C-path the focusing optics were redesigned to focus the laser at position B near the laser window; because diffraction is an order of magnitude greater than for the Nd:YVO<sub>4</sub> laser. Considering the effective hard apertures along the C-path, we find that the radius of the laser spot is 1.2 mm at position B, which is about twice the size of the electron beam.

## Calculated results

By introducing a 2- $\mu$ m laser, we expect to be able to generate gamma rays with energies spanning the 4- to 21-MeV range, with electron energies tuned to 0.7–1.5 GeV. Thus, driving with such a laser will enable us to generate gamma rays spanning an energy range that is not attainable using the present lasers. We proceeded by considering a beam transport path for a 2- $\mu$ m laser and calculating the expected gamma-ray luminosity. The first case considered entailed passing the 2- $\mu$ m laser beam through the N-path so that it collides with the equal-sized electron

beam at point A. However, this design proved unsatisfactory because of diffraction losses for the 2- $\mu\text{m}$  laser. We next considered the following two cases (Fig. 2): (1) At point A, the 2- $\mu\text{m}$  laser beam that has passed through the N-path collides with the electron beam. The laser beam radius at point A is 1.2 mm (twice as large as the radius of the electron beam). (2) At point B, a laser beam that has passed through the C-path collides with the electron beam. The laser beam radius at point B is 0.6 mm, which is the same size as the electron beam. From the same calculation that produced results for the case of the Nd:YVO<sub>4</sub> and CO<sub>2</sub> lasers, we estimate a luminosity for cases (1) and (2) to be 6400 photons/(W·mA·s) and 3500 photons/(W·mA·s), respectively. We conclude that higher luminosity can be obtained for case (1), with the collision at point A, where the long interaction zone may be used with advantage even with a large laser beam radius. Under these conditions, the luminosity of the gamma rays generated by a 2- $\mu\text{m}$  laser should be at the same level as for the Nd:YVO<sub>4</sub> and CO<sub>2</sub> lasers.

At present, gamma-rays with energies of 17–37 MeV and 1.7–3.9 MeV are achieved using an Nd:YVO<sub>4</sub> and a CO<sub>2</sub> laser, respectively, and the luminosities obtained in both cases are 6000–7000 photons/(W·mA·s). The maximum gamma-ray flux is currently  $5 \times 10^6$  photons/s, obtained using a laser power of 4 W and an electron-beam current of 200 mA. We also estimate that the gamma-ray luminosity produced by a 2- $\mu\text{m}$  laser should be 6400 photons/(W·mA·s), with energies covering the range of 4–21 MeV.

Nd:YVO<sub>4</sub>, CO<sub>2</sub>, and Tm-doped fiber lasers (the latter as a 2- $\mu\text{m}$  laser) are all capable of generating kW-level output power. Using this level laser power with an electron-beam current of 200 mA allows a gamma-ray flux of  $10^9$  photons/s to be achieved. Thus, the laser-Compton gamma-ray source in NewSUBARU has the potential to generate such high fluxes over a continuously tunable energy range from 1 to 37 MeV.

#### References

- [1] S.Amano *et al.*, AIP Conf. Proc, **1234**, pp.489 (2010).

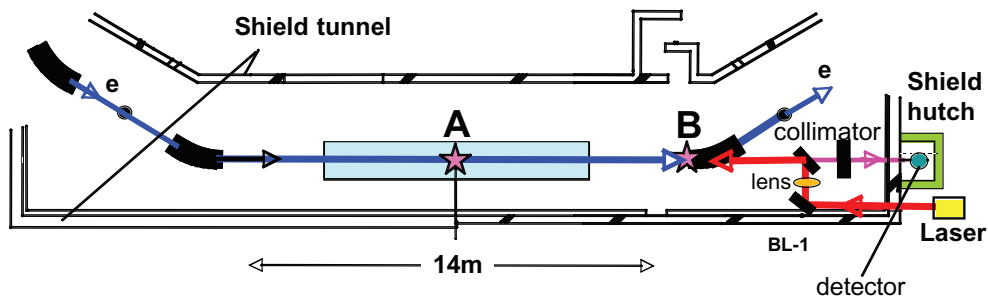


FIG1. Experimental setup of laser Compton gamma-ray

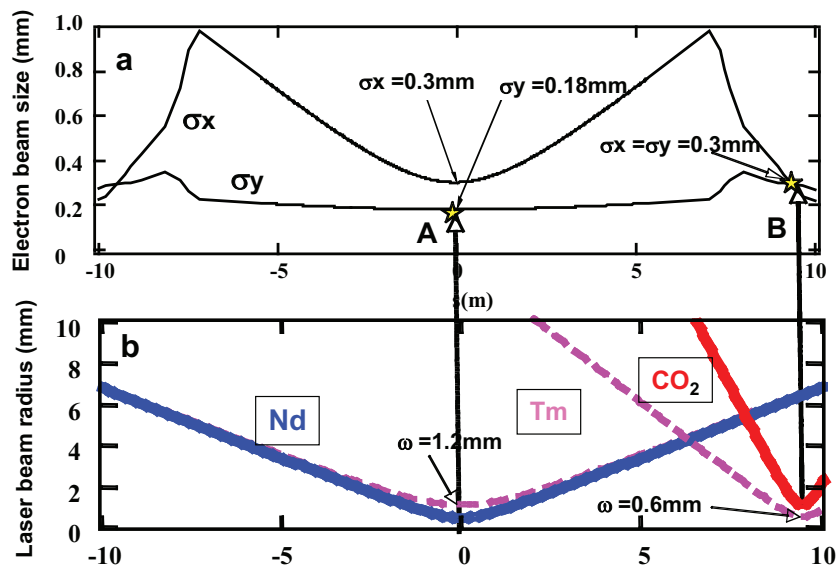


FIG2. (a) Electron beam size and (b) laser beam radius of the Nd:YVO<sub>4</sub>, CO<sub>2</sub> and Tm lasers in the interaction zone. The zero value on the horizontal axis refers to the center of the long straight section.

Sun

# Imaging for Stress Corrosion Cracking in Stainless Steel with Laser Compton Scattering Gamma Ray

T.Hasegawa<sup>1)</sup>, S.Nakahigashi<sup>1)</sup>, T.Fujishiro<sup>2)</sup>, K.Horikawa<sup>3)</sup>, M.Terasawa<sup>3)</sup> and S.Miyamoto<sup>3)</sup>

<sup>1)</sup>Japan Power Engineering and Inspection Corporation, <sup>2)</sup>University of Hyogo, <sup>3)</sup>LASTI, University of Hyogo

## Abstract

In order to detect SCC non-destructively, laser compton scattering gamma ray imaging was examined. As a result, imaging with 1.76MeV gamma ray was available to detect artificial slit for 30mm thick stainless steel and SCC for 10mm thick stainless steel.

## Introduction

The simulation technique for ultrasonic propagation is very useful as a support tool to analyze the result of practical ultrasonic testing (UT). In Japan power Engineering and Inspection Corporation (JAPEIC), large-scale ultrasonic simulation system used finite element method has been developed and put to practical use [1-3].

In ultrasonic simulation, the information, such as specimen shape, physical properties of specimen, three-dimensional defect shape and distribution, is necessary. Particularly, the information about defect is very important to evaluate the validity of simulation model and to simulate more accurately.

Stress corrosion cracking (SCC), known as a defect occurred in the structure in nuclear power plant or chemical plant, has very intricate ramification and narrow crack width. Therefore, it has been difficult to observe actual 3D SCC shape in the specimen so far.

Recently, the authors have succeeded for the first time to observe 3D SCC image occurred in stainless steel and nickel-based alloy by synchrotron radiation used Spring-8, synchrotron radiation facility [4-5]. Fig.1 shows the 3D CT image of SCC in stainless steel as an example [6]. However, it was impossible to compare the actual result of UT since the size of specimen was very small (a few mm diameters) and UT was not available.

Therefore, we tried to perform imaging experiment by gamma( $\gamma$ ) ray for larger size of specimen (a few dozens of millimeter thick).

## Experiments

SUS316L stainless steels were used as specimens in this imaging experiment. For each specimen, SCC was artificially developed in high-pressure pure hot water at 300°C. SCC specimen size was 10x10mm and the thickness was from 10 to 50mm. Fig.1 shows the SCC specimen. Some of SUS316L blocks were prepared as standard specimen machined the slit artificially. We also prepared the weld joint specimen with SCC. The base metal was SUS304 and filler metal was SUS308. The thickness of specimen was 10mm.

Imaging experiment was performed by  $\gamma$  ray in NEW SUBARU BL01A. In this experiment,  $\gamma$  ray

was generated by collision between CO<sub>2</sub> laser and electron. This  $\gamma$  ray energy was 1.76MeV. Imaging plate (IP) which had 50um resolution was utilized to detect the image. Table 1 shows the examination condition and fig.2 shows experimental equipment, respectively.

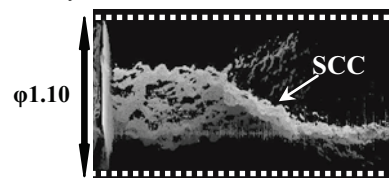


Fig.1 Three dimensional CT image of SCC in stainless steel observed by synchrotron radiation [6].

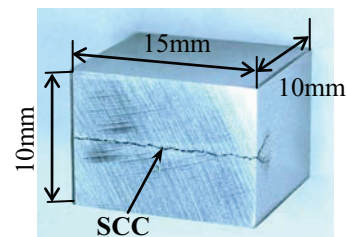


Fig.2 SCC specimen for imaging experiment.

Table 1. Experimental condition.

Electron energy	1.0 GeV
Laser	CO <sub>2</sub> laser ( $\lambda$ :10.54um)
Gamma ray energy	1.76MeV
Irradiation time	1h, 3h, 6h, 9h
Image detection	Imaging plate
Specimen thickness	10-50mm
Artificial slit	Width:0.245mm Depth:1mm~5mm

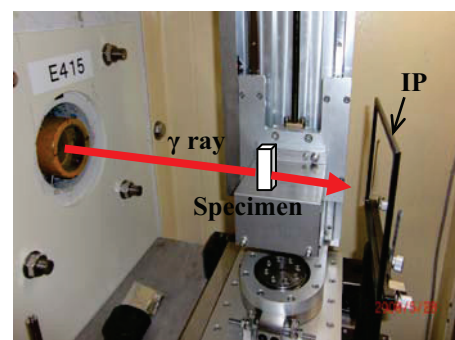


Fig.2 Experimental equipment.

## Experimental results

Imaging experiment was performed for 10mm thick standard specimen which had 21 slits (width: 0.245mm, depth: ~1.7mm) at 2mm intervals. Fig.3 shows the image for standard specimen. 7 slits were confirmed both sides of beam center on the image. The slit images between third and sixth from beam center were clear. The energy of  $\gamma$  ray at the position from third to sixth slit was estimated at 0.6 ~1.0MeV in calculation.

In order to examine effects of specimen thickness and irradiation time for the image contrast, imaging experiments for two kinds of standard specimen with 10mm and 30mm thick were carried out. Irradiation times were 3hrs, 6hrs and 9hrs. Fig.4 shows the result of 3hrs irradiation as an example. In cases of slit size in this experiment, there was no remarkable difference in the slit image contrast between 10mm and 30mm thick specimen. The image resolution was saturated above 6hrs irradiation although the image was clearer with increasing with irradiation time until 6hrs.

Imaging experiment was also performed for the 10mm thick SUS316L specimen with SCC. Irradiation time was for 3hrs and the beam center of  $\gamma$  ray was located at 5mm distance from the crack. Fig.5 shows the image of SCC in SUS316L. Y-shaped crack was confirmed on the image although the contrast was not so clear. In cases of measurement by optical microscope, the size of crack width near the specimen surface was about 250 $\mu$ m. On the other hands, the width near the crack tip was 50~100 $\mu$ m.

Moreover, the experiment was carried out for weld joint specimen with SCC. The irradiation time was for 3hrs. Fig.6 shows the image of weld joint specimen. It was confirmed by the figure that the crack was occurred at heat affected zone (HAZ) and propagated toward the specimen depth. It was noted that the crack penetrated into filler metal from HAZ, with its propagating. The crack depth was measured about 13mm.

## Conclusions

Imaging measurements by 1.76MeV  $\gamma$  ray were performed for stainless steels which had SCC or artificial slit. Clear slit image was confirmed for stainless steel specimen up to 30mm thick. On the other hands, SCC image was confirmed for 10mm thick specimen although the image was not so clear.

Laser compton scattering gamma ray imaging may be good tool as non-destructive defect detection technique to compare with the result of UT since the defect detection for 10mm thick stainless steel by UT is available.

## References

- [1] I.Komura *et al.*, ULTRASONIC TECHNO, Vol.13, No.2 (2001), P10 (in Japanese).
- [2] T.Furukawa *et al.*, Maintenology, Vol.3, No.3

(2004), P10 (in Japanese).

- [3] I.Komura *et al.*, JAPEIC NDE Center Technical Review, Vol.4 (2001), P10 (in Japanese).
- [4] S.Nakahigashi *et al.*, Proc. 2007 Spring Meeting of AESJ (2007), P36 (in Japanese).
- [5] S.Nakahigashi *et al.*, Proc. 2008 Fall Meeting of AESJ (2008), P929 (in Japanese).
- [6] S.Nakahigashi *et al.*, Maintenology, Vol.8 No.3 (2009), P69 (in Japanese).

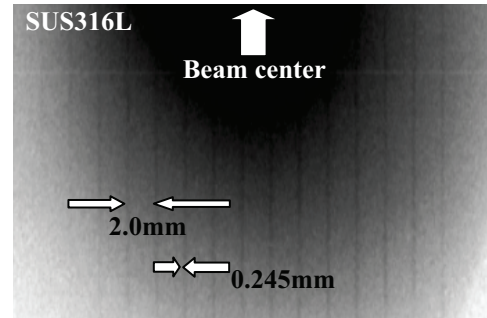


Fig.3 The  $\gamma$  ray image of standard specimen.

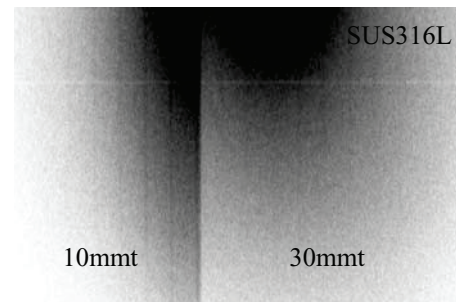


Fig.4 The effect of specimen thickness.

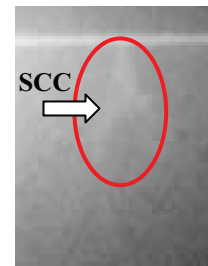


Fig.5 The image of SCC in SUS316L specimen.

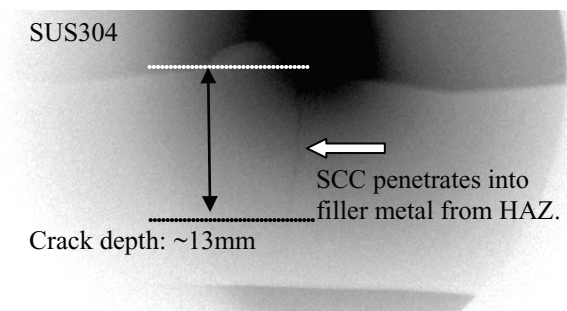


Fig.6 The image of SCC penetrated into filler metal from heat affected zone (HAZ).

# Study of $^{12}\text{C}(\gamma,2\alpha)^4\text{He}$ with NewSUBARU laser Compton scattered $\gamma$ -ray beam

Tatsushi Shima<sup>a</sup>, Yasuki Nagai<sup>b</sup>, Shuji Miyamoto<sup>c</sup>, Sou Amano<sup>c</sup>, Ken Horikawa<sup>c</sup>,  
Takayasu Mochizuki<sup>c</sup>, Hiroaki Utsunomiya<sup>d</sup> and Hidetoshi Akimune<sup>d</sup>

<sup>a</sup>Research Center for Nuclear Physics, Osaka University

<sup>b</sup>Nuclear Science and Engineering Directorate, Japan Atomic Energy Agency

<sup>c</sup>Laboratory of Advance Science and Technology for Industry, The University of Hyogo

<sup>d</sup>Department of Physics, Konan University

## Abstract

The  $^{16}\text{O}(\gamma,2\alpha)^4\text{He}$  reaction cross section was measured at the  $\gamma$ -ray energies between 16 MeV and 39 MeV using an active target method and a quasi-monochromatic  $\gamma$ -ray beam provided at the Laboratory of Advanced Science and Technology for Industry (LASTI) of the University of Hyogo. The cross section is found to be rather small in the energy region corresponding to the  $2^+$  and  $4^+$  excited states of the intermediate  $^8\text{Be}$  nucleus, while it becomes large above the energy corresponding to the  $^8\text{Be}$   $1^-$  state, being in contrast to the latest result reported by Afanas'ev and Khodyachikh. The present result suggests the cross sections are dominated by the contributions of the  $1^-$  states in  $^8\text{Be}$  and  $^{12}\text{C}$  excited with the E1 transition.

## Introduction

The triple-alpha reaction and the  $^{12}\text{C}(\alpha,\gamma)^{16}\text{O}$  reaction are considered to play essential roles in the evolution and the nucleosynthesis of the stars in the He-burning phase [1]. It has been discussed that the triple-alpha reaction plays important roles also in various processes such as the He-ignition in Type I X-ray bursts [2] and the break out from the H-burning in the rp-process in neutrino-driven wind [3]. To study those processes in detail, accurate data of the triple-alpha reaction rate are demanded. The cross section of the reaction, however, is hardly measured by a laboratory experiment, because it is a fusion reaction of three alpha-particles, and the reaction rate must be calculated with some reliable theoretical model for the three-alpha system. To develop such a reliable theory, the information about the inverse reaction, i.e., the photodisintegration of  $^{12}\text{C}$  is expected to be helpful. For that purpose we made a new measurement of the  $^{12}\text{C}(\gamma,2\alpha)^4\text{He}$  reaction cross section with use of an active target and a quasi-monochromatic  $\gamma$ -ray beam. In this contribution the preliminary result is presented.

## Experiment

The experiment was performed at the Laboratory of Advanced Science and Technology for Industry (LASTI) at the University of Hyogo. A quasi-monochromatic  $\gamma$ -ray beam in the energy range of between 16 MeV and 39 MeV was generated at the BL01 beam line of the NewSUBARU storage ring in LASTI using the laser Compton-backscattering (LCS) method [4,5]. Figure 1 shows a schematic view of the experimental setup.

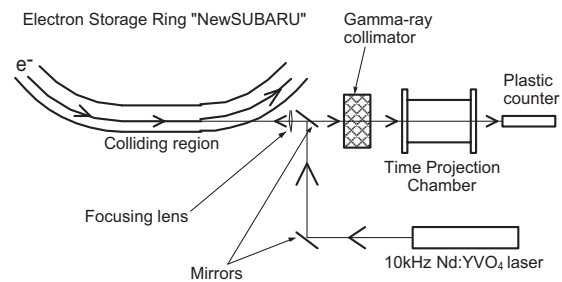


Fig. 1. A schematic drawing of the experimental setup (top view).

The LCS  $\gamma$ -ray was generated by the head-on collision of the electron beam and the laser lights with the wavelengths of 1064nm (fundamental wave) and 532nm (second harmonics) of a Nd:YVO<sub>4</sub> pulse laser. The 180° backscattered  $\gamma$ -ray was extracted by using a collimator made of 10 cm thick lead brick. Using a collimator with the collimation angle of 0.081 mrad, the  $\gamma$ -ray energy spread of 4.5% (FWHM) was achieved.

The intensity of the incident  $\gamma$ -ray was 20000~40000 photons/s, which was measured online by using a plastic scintillation counter whose detection efficiency was calibrated with a BGO counter with the absolute efficiency better than 99%. The energy distribution of the incident  $\gamma$ -rays was determined so as to reproduce the pulse height spectrum measured with a 6'' $\phi$   $\times$  5'' NaI(Tl) scintillation counter using its response functions calculated with the EGS5 Monte Carlo code. Fig. 2 shows an example of the  $\gamma$ -ray pulse height spectrum and the intrinsic  $\gamma$ -ray energy distribution.

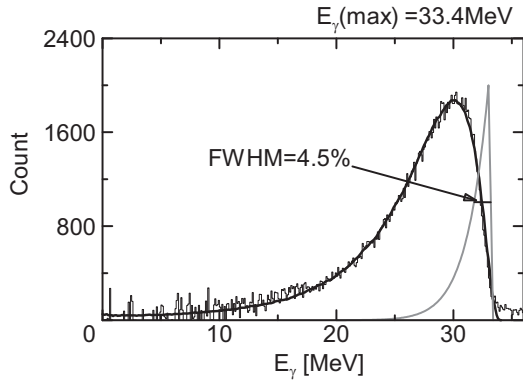


Fig. 2. A typical pulse height spectrum of the LCS g-ray measured with a NaI(Tl) scintillation counter (histogram) and the reproduced pulse height spectrum (black solid curve) assuming the intrinsic distribution (gray solid curve) of the  $\gamma$ -ray energy.

The  $\gamma$ -ray beam was introduced into a time-projection chamber (TPC) which contained a gas mixture of 80% He and 20% CD<sub>4</sub> [6]. The <sup>12</sup>C nuclei in the CD<sub>4</sub> gas worked as an active target, provided a detection efficiency better than 98.5% and an acceptance of the solid angle of  $4\pi$  for the <sup>12</sup>C( $\gamma,2\alpha$ )<sup>4</sup>He reaction events. The overall sensitivity for the photodisintegration was checked by the simultaneous measurement of the D( $\gamma,p$ )n reaction, whose cross section has been well known both experimentally and theoretically. As shown in Fig. 3, the present result on the D( $\gamma,p$ )n reaction cross section is in a good agreement with the existing data [6,7,8,9] as well as a theoretical calculation [10] and the ENDF/B-VII evaluation [11].

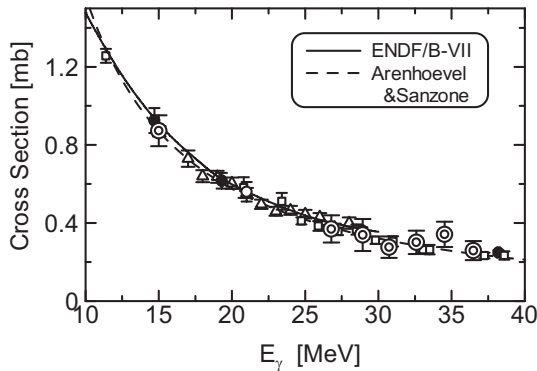


Fig. 3. D( $\gamma,p$ )n reaction cross section. The open circles and double circles indicate our previous data measured at AIST and the present ones, respectively. The triangles, filled circles, and boxes denote the data from Refs. [7], [8], and [9], respectively. The solid curve and dashed curve are the theoretical calculation with the potential model [10] and the evaluated data [11], respectively.

The <sup>12</sup>C( $\gamma,2\alpha$ )<sup>4</sup>He events were identified by requiring the existence of the three tracks of the charged fragments emitted from the  $\gamma$ -ray beam axis and their large energy losses in the TPC gas. Figures 4 and 5 show the examples of the tracks of three  $\alpha$ -particles from the <sup>12</sup>C( $\gamma,2\alpha$ )<sup>4</sup>He reaction and the major background probably due to the  $\alpha$ -decays of the radon isotopes contained in the TPC gas, respectively.

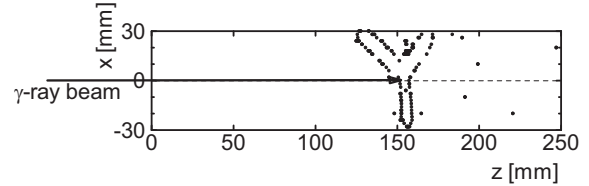


Fig. 4. An example of the tracks of the  $\alpha$ -particles from the <sup>12</sup>C photodisintegration. The box shows the edge of the effective volume of the TPC (side view). The  $\gamma$ -rays are injected from the left.

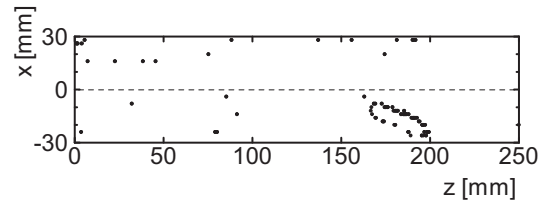


Fig. 5. An example of the track of the background due to the  $\alpha$ -decay of a radioactive isotope contained in the TPC gas. It can be easily distinguished from the <sup>12</sup>C( $\gamma,2\alpha$ )<sup>4</sup>He events because of the absence of the three tracks originating in the  $\gamma$ -ray beam axis.

### <sup>12</sup>C( $\gamma,2\alpha$ )<sup>4</sup>He cross section

The cross section was obtained from the numbers of the observed <sup>12</sup>C( $\gamma,2\alpha$ )<sup>4</sup>He events as a function of the incident  $\gamma$ -ray energy. Figure 6 shows the preliminary result from the present experiment together with the existing data including our previous data measured by using the LCS  $\gamma$ -ray source at the National Institute of Advanced Industrial Science and Technology (AIST). Compared to the latest result [15], the present cross section is significantly smaller in the energy region below  $\sim 20$  MeV where the 2<sup>+</sup> and 4<sup>+</sup> excited states of the intermediate <sup>8</sup>Be nucleus exist. As shown in Tables 1 and 2, there are few 1<sup>-</sup> states below  $E_\gamma \sim 20$  MeV in <sup>8</sup>Be and <sup>12</sup>C, while many 1<sup>-</sup> states with relatively large widths exist above  $\sim 20$  MeV. Therefore the present result suggests the reaction is dominated by the E1 transition to the 1<sup>-</sup> excited states of the target <sup>12</sup>C nucleus and the intermediate <sup>8</sup>Be nucleus.

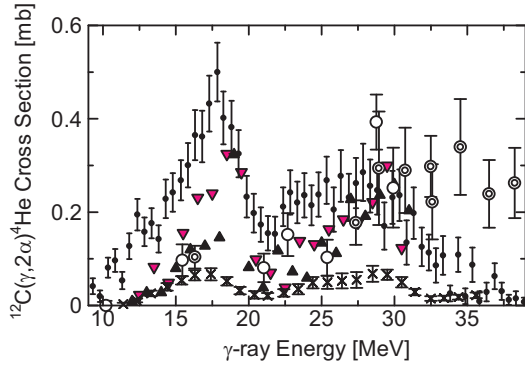


Fig. 6.  $^{12}\text{C}(\gamma,2\alpha)^4\text{He}$  reaction cross section. The open circles and double circles indicate our previous data measured at AIST and the present ones, respectively. The filled triangles, gray downward triangles, diagonal crosses, and dots denote the data from Refs. [12], [13], [14] and [15], respectively.

Table 1. Excited states of  $^8\text{Be}$  [16].  $E_x$ ,  $J^\pi$  and  $\Gamma$  stand for the excitation energy, spin-parity, and the total width of a state.

$E_x$ [MeV]	$J^\pi$	$\Gamma$ [MeV]
0	$0^+$	$5.57 \times 10^{-6}$
3.040	$2^+$	1.5
11.400	$4^+$	3.5
19.400	$1^-$	0.65
19.860	$4^+$	0.7
20.100	$2^+$	1.1
20.900	$4^-$	1.6
21.500	$3^+$	1.0
22.000	$1^-$	4
24.000	$(1,2)^-$	7

Table 2. Excited states of  $^{12}\text{C}$  [17].

$E_x$ [MeV]	$J^\pi$	$\Gamma$ [MeV]
0	$0^+$	0
4.439	$2^+$	$1.08 \times 10^{-8}$
7.654	$0^+$	$8.50 \times 10^{-6}$
9.641	$3^-$	0.034
10.300	$(0^+)$	3
10.844	$1^-$	0.315
17.230	$1^-$	1.15
19.200	$(1)$	$\sim 1.1$
22.650	$1^-$	3.2
25.400	$1^-$	2
27.000	$(1)$	1.4
28.200	$1^-$	1.6

On the other hand, a large strength was observed in the energy region above 29 MeV where a lot of excited states with unknown  $J^\pi$  exist. It will be important for better understanding of the mechanism of the  $^{12}\text{C}(\gamma,2\alpha)^4\text{He}$  reaction to determine  $J^\pi$  of those excited states

experimentally. The spin and parity of each excited state are to be determined from the angular distribution and analyzing power at the relevant excitation energy, and the LCS  $\gamma$ -ray will be a promising tool for such measurements because of its nice features such as a very high polarization, a small energy spread and a small angular spread.

### Summary and Discussion

The  $^{12}\text{C}(\gamma,2\alpha)^4\text{He}$  reaction cross section was measured by means of a quasi-monochromatic  $\gamma$ -ray beam for the first time. Using an active target technique, the absolute cross section was determined with high accuracy, and it will be useful to develop a reliable theoretical method to calculate the triple-alpha fusion reaction.

### Acknowledgment

This work was supported in part by Grant-in-Aid for Specially Promoted Research of the Japan Ministry of Education, Science, Sports and Culture and in part by Grant-in-Aid for Scientific Research of the Japan.

### References

- [1] A.Bcdefg *et al.*, J. Lasti Rev., **34**,2, pp.1234-1244 (2000).
- [1] E.E. Salpeter, ApJ **115**, 326 (1952); F. Hoyle, ApJ Supp. **1**, 121 (1954).
- [2] K. Nomoto, F.-K. Thielemann, and S. Miyaji, A&A **149**, 239 (1985); F.-K. Thielemann *et al.*, Prog. Par. Nucl. Phys. **46**, 5 (2001).
- [3] S. Wanajo, ApJ **647**, 1323 (2006).
- [4] K. Aoki *et al.*, Nucl. Instr. Meth. in Phys. Res. A **516**, 228 (2004).
- [5] S. Miyamoto *et al.*, Radiation Meas. **41**, S179-S185 (2006).
- [6] T. Kii, T. Shima, T. Baba, and Y. Nagai, Nucl. Instr. Meth. in Phys. Res. A **552**, 329 (2005).
- [7] D.M. Skopik *et al.*, Phys. Rev. C **9**, 531 (1974).
- [8] R. Bernabei *et al.*, PRL **57**, 1542 (1986).
- [9] C. Dupon *et al.*, Nucl. Phys. A **445**, 13 (1985).
- [10] H. Arenhövel and M. Sanzone, Few-Body Systems Suppl. **3**: *Photodisintegration of the Deuteron* (Springer-Verlag, Wien,1991).
- [11] ENDF/B-VII data file for  $^1\text{H}$  (MAT=125). 2006, evaluated by G.M. Hale.
- [12] V.N. Maikov, Zh. ekper. teor. Fiz. **34**, 1406 (1958) (Soviet Physics-JETP **7**, 973 (1958)).
- [13] A. Murakami, J. Phys. Soc. Japan **28**, 1 (2008).
- [14] E.A. Kotikov *et al.*, Izv. Ross. Akad. Nauk, Ser. Fiz. **66**, 445 (2002).
- [15] S.N. Afanas'ev and A.F. Khodyachikh, Phys. Atomic Nuclei **71**, 1827 (2008).
- [16] ENDSF file for  $^8\text{Be}$ , edited by J.H. Kelley, J.L. Godwin, C.G. Sheu, *et al.*, 2004.
- [17] ENDSF file for  $^{12}\text{C}$ , edited by F. Ajzenberg-Selove and J.H. Kelley, Nucl. Phys. A **506**, 1 (1990).

# Laser-plasma debris from a rotating cryogenic–solid-Xe target

S.Amano, Y.Inaoka, H.Hiraish, S.Miyamoto, T.Mochizuki  
LASTI/UH

## Abstract

We investigate the characteristics of laser plasma debris that is responsible for damaging optics. The debris is composed of fast ions, neutral particles, and fragments, and originates from a solid Xe target on a rotating drum that we developed as an extreme ultraviolet (EUV) source. The ice fragments appear to be a problem most notably with solid Xe targets; however, we find that the damage induced by Xe ice fragments can be avoided by simply reducing the laser pulse energy. We find the number of fast neutral particles to be an order of magnitude less than the number of ions, and we clarify that the plasma debris is primarily composed of fast ions. In addition, we find that the number of fast ions having a few dozen keV's of energy decreases when using the rotating target compared with the rest target. We attribute this to a gas curtain effect from the Xe gas localized at the rotating target surface. We estimate the sputtering rate of the Mo/Si mirror, which is caused primarily by the fast ions, to be 104 nm/1 M shots at 190 mm from the source plasma and at an 11.25° angle from the incident laser beam. Up to the 1M shots exposure, remarkable degradation of the mirror reflectivity is not observed though the sputtering damages the mirror. Mitigation of the ions by using gas and/or magnetic fields will further improve the mirror lifetime. By comparing with a liquid jet Xe target, we conclude that the sputtering rate per conversion efficiency when using the solid Xe targets on the rotating drum is the same as that when using the liquid Xe targets. The high conversion efficiency of 0.9% in the rotating drum solid Xe target makes this technique useful for developing laser plasma EUV sources.

## Introduction

Laser plasma radiation from high density, high temperature plasma constitutes an attractive, high brightness point source for producing EUV to x-ray radiation. It is achieved by illuminating a target with high-peak-power laser irradiation.

We originally developed a fast rotating cryogenic drum system, which can continuously supply a solid Xe target. Using the drum system, a maximum CE of 0.9% was demonstrated at 13.5 nm and with the 2% bandwidth required for an EUVL source. The source operated continuously with an output power of 1W.

We investigated the plasma debris from the drum target system, that is responsible for damaging optics. The debris consists of fast ions, fast neutrals, and ice fragments. In this article, we report in detail the characteristics of the debris and discuss the damage it causes on a Mo/Si mirror.

## Experiments

Figure 1 shows the experimental setup used to obtain data on the characteristics of the plasma debris from a cryogenic solid Xe target on a rotating drum. Initially, data characteristic of fast ions, neutrals, and fragments, which were thought to be main elements of plasma debris, were obtained in single-shot laser experiments using a conventional Nd:YAG rod laser with a wavelength of 1064 nm and a 10 ns pulse width. By adjusting the focal lens position, laser

intensity on the target was optimized to be  $\sim 1 \times 10^{10}$  W/cm<sup>2</sup> to maximize the EUV radiation around 13.5nm.

Ions from the plasma were detected using a charge collector (CC) with an applied bias voltage of -100 V, and their kinetic energies were estimated from time of flight (TOF) signals. The CC was fixed 190 mm from the plasma and at a 22.5° angle with respect to the incident laser beam.

We used a double micro-channel plate (MCP) (Hamamatsu, F4655-10) to detect neutral particles, after an electrical field repelled the ions. We positioned the MCP at 45° with respect to the laser beam, and mounted it inside a small vacuum chamber that was connected via a vacuum tube to the main vacuum chamber. The tube included a pair of electrodes and a 0.75 mm diameter pinhole. The pinhole allowed us to differentially pump the MCP chamber and keep the vacuum pressure below 10<sup>-4</sup> Pa. The distance from the plasma target point to the MCP was 1050 mm.

To observe damages by fragment impact, we placed a Si substrate 100 mm from the plasma target point and at a 22.5° angle with respect to the incident laser beam.

Next, we conducted multi-shot laser experiments to study mirror damage caused by the total plasma debris (ions, neutrals, and fragments) using a high-repetition-rate Nd:YAG pulsed slab laser developed in-house. The slab laser was configured to generate 1064 nm pulses with pulse widths of 20 ns at a repetition rate of 320 Hz. In

the experiments, a Mo/Si mirror sample and a gold-coated quartz crystal microbalance (QCM) sensor (Sigma, SQM-160) were placed 100 mm from the plasma at 22.5° and 45° angles, respectively, to measure total erosion rates upon extended multi-shot plasma operation.

EUV energy from the plasma was also monitored by an EUV energy monitor placed 190 mm from the plasma at an 11.25° angle with respect to the incident laser beam. The energy monitor consisted of an X-ray diode with a Mo/Si filter (IRD, AXUV-20) and a Mo/Si mirror to select the wavelength band around 13.5 nm. Mirror damage leading to reduced reflectivity is detected by monitoring the decrease in EUV energy during multi-shot laser operation.

### Results

Being an inert gas at room temperature, Xe is deposition-free compared with other metal targets. However, damage to mirror surfaces occurs due to sputtering. In particular, damage by Xe ice fragments was considered problematic for solid Xe targets. We find, however, that this damage can be avoided simply by reducing the laser pulse energy. We find that the number of fast neutral particles is approximately an order of magnitude less than the number of ions, and we demonstrate that the major plasma debris component is fast ions. We also find that the number of the fast ions having a few dozen keV's of energy decreases when using the rotating target compared to that observed when using the stationary target. We attribute this to the gas curtain effect of Xe gas localized on the rotating target surface.

The sputtering of the Mo/Si mirror is mainly caused by fast ions, and the sputtering rate is estimated to be 104 nm/1 M shots with the mirror 190 mm from the plasma at 11.25° from the incident laser beam. If a Mo/Si multilayer mirror having more than 40 layers pairs is used, the degradation of its reflectivity under such conditions will be kept under 10% for an exposure of up to 1M shots.

The major plasma debris component is ions, and we believe its mitigation to be comparatively simple. To reduce the debris and improve the mirror lifetime, we are now developing ion-mitigation techniques that involve using gas.

The measured sputtering rate per CE at 51° from the incident laser beam is essentially equal to that obtained when using the liquid Xe jet. Assuming that the debris distribution for both solid and liquid targets is identical, we conclude that the sputtering rate per CE for solid Xe rotating targets is the same as for liquid Xe targets. Considering the higher efficiency (0.9%) obtained using a solid Xe rotating target compared with a liquid Xe jet target (0.3%), we conclude that a solid Xe rotating target is advantageous for laser plasma EUV sources.

### References

- [1] S.Amano *et al.*, Rev. Sci. Instrum., **81**,023104 (2010).

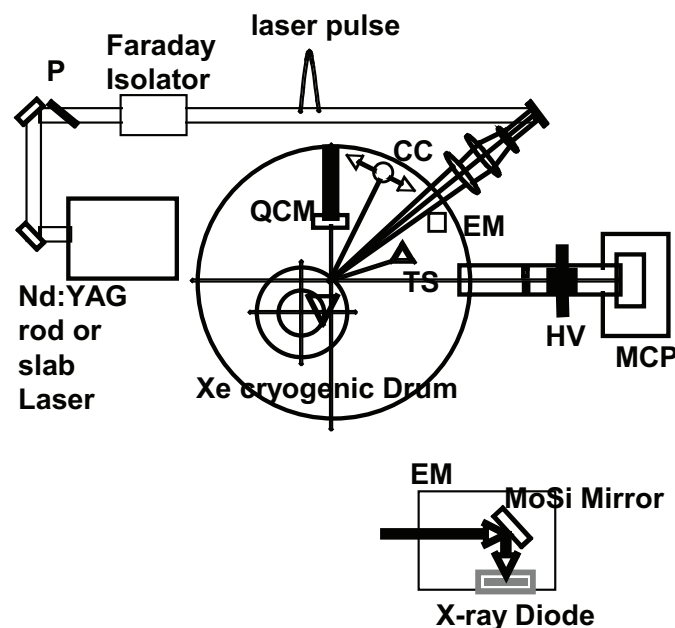


Fig.1 Experimental setup.

# Mitigation by argon buffer gas of fast debris from cryogenic xenon laser plasma EUV light source

T. Sekioka<sup>1</sup>, S. Amano<sup>2</sup>, T. Inoue<sup>2</sup>, and T. Mochizuki<sup>2</sup>  
<sup>1</sup>Graduate School of Engineering, University of Hyogo,  
<sup>2</sup>LASTI, University of Hyogo

## Abstract

One of the serious problems in the laser-produced plasma for an extreme ultraviolet (EUV) light source used for the next generation lithography is the generation of fast ions that damage the EUV collector optics. Gas curtain method is regarded as one of the most efficient methods for mitigation of fast debris without serious loss of EUV light. We have investigated the mitigation of fast ions from laser-produced xenon plasma on the rotating drum xenon cryogenic target by argon gas curtain. Energy spectra of fast  $\text{Xe}^+$ ,  $\text{Xe}^{2+}$ ,  $\text{Xe}^{3+}$  ions from the xenon plasma were obtained at back ground pressure of  $4 \times 10^{-4}$  Pa, before argon gas was introduced into the chamber. Argon gas flow rate was increased by 100 ml/min step to the extent of 800 ml/min. We have obtained the pressure dependence of the energy spectra of xenon ions for each charge state. These data on the attenuation of xenon ions by argon buffer gas are indispensable for designing a gas curtain debris mitigation system.

## Introduction

An extreme ultraviolet (EUV) light source is under development for use in EUV lithography. However, in general, these targets emit particle debris that produce mechanical damage and/or deposition on the mirrors degrading their reflectivity in a short period. Mirror cleaning will become a serious problem. In this study, we investigated the mitigation by argon gas curtain of the fast xenon ions from the cryogenic xenon target.

## Experiments and results

A schematic diagram of the experimental setup is shown in Fig. 1. A xenon cryogenic target on the rotating drum<sup>[1]</sup> was irradiated in a target chamber by a pulsed 1.06  $\mu\text{m}$  Nd:YAG slab laser<sup>[2]</sup> with a energy of 0.3 J at incident normal. The back ground pressure inside the target chamber was  $4 \times 10^{-4}$  Pa. Fast ions were measured with a Thomson parabola (TP) ion analyzer which was set at an angle of  $45^\circ$  with respect to the laser axis. The fast ions were collimated with double pinholes of 0.3mm in diameter, and travel on species-dependent trajectories determined by electric and magnetic deflections and then impinge upon the micro channel plate (MCP). Both the magnetic field and electric field were applied between 1-cm-thick and 5-cm-length space. Figure 2 shows the luminescent image of the fluorescent screen which was set at the output of the MCP, from a single laser shot. Thomson parabolas of  $\text{Xe}^+$ ,  $\text{Xe}^{2+}$  and  $\text{Xe}^{3+}$  were confirmed.

Argon gas was introduced into the target chamber, and the argon gas flow rate was increased by 100 ml/min step. For each argon gas flow rate, we obtained the energy spectra of xenon ions resolving their charge state.

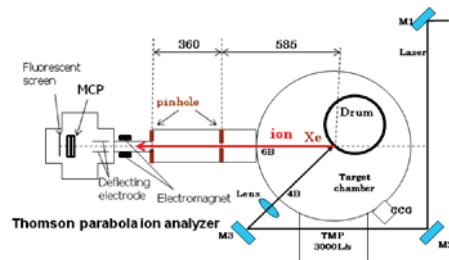


Fig.1. Experimental setup.

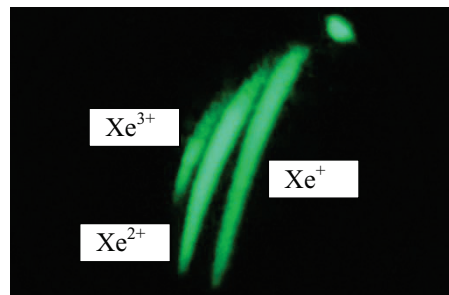


Fig.2. A typical image of Thomson parabola ion analyzer.

Figs.3, 4 and 5 show the energy spectra of  $\text{Xe}^+$ ,  $\text{Xe}^{2+}$  and  $\text{Xe}^{3+}$  at several argon gas flow rates. The response of MCP for ions was not considered in the analysis. Above argon gas flow rate of 500 ml/min, only  $\text{Xe}^+$  ions could be observed. Above 800 ml/min, where the argon partial pressure was 0.56 Pa, the  $\text{Xe}^+$  ions intensity was so weak that they were buried in the back ground.

Data analysis is on the progress for determining the argon column density that is required to stop the fast xenon ions to the level where no sputtering occurs without serious loss of X-ray<sup>[3]</sup>.

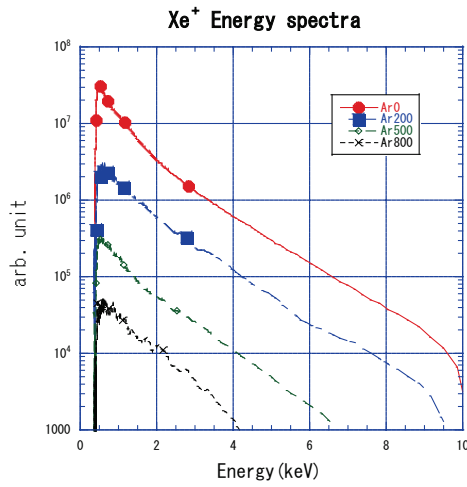


Fig.3. Energy spectra of fast  $Xe^+$  debris ions at several argon gas flow rates. The flow rates are 0, 200, 500 and 800 ml/min.

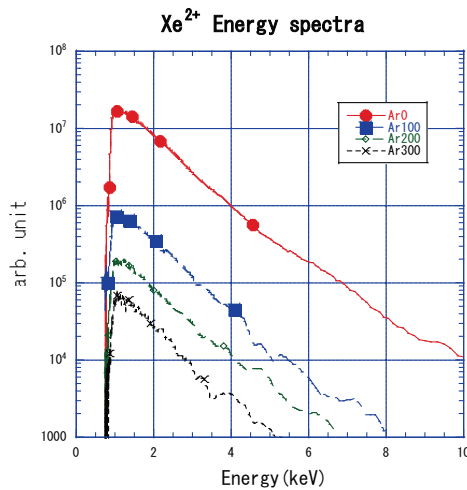


Fig.4. Energy spectra of fast  $Xe^{2+}$  debris ions at several argon gas flow rates. The flow rates are 0, 100, 200 and 300 ml/min.

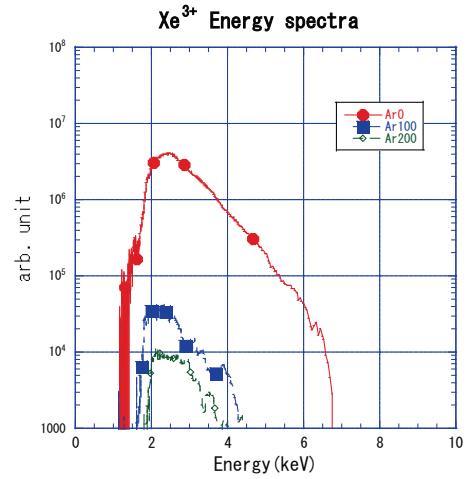


Fig.5. Energy spectra of fast  $Xe^{3+}$  debris ions at several argon gas flow rates. The flow rates are 0, 100 and 200 ml/min.

### References

- [1] K.Fukugaki *et al.*, Rev. Sci. Instrum. **77**, 063114 (2006)
- [2] S.Amano *et al.*, Rev. of Laser Engineering, Vol. 29, pp.679-682 (2001)
- [3] T.Inoue *et al.*, Lasti Annual Report, Vol.10, pp27-28 (2008)

# Mitigation effect of plasma debris from cryogenic xenon target by argon jet

T. Inoue, S. Amano, T. Mochizuki  
University of Hyogo LASTI

## Abstract

In order to mitigate the sputtering effect on collection mirror which was caused by xenon fast debris, the mitigation effect of plasma debris from the rotating drum xenon cryogenic target by an argon gas jet and its absorption for soft X-ray from the plasma were investigated. The sputtering by xenon debris was mitigated to be 1/50 when the argon gas flow was 0.75L/min. The measurement of ion debris showed that a decrease in the energy of the colliding particle contributed to the mitigation than a decrease of the number of collision particles. In addition, the attenuation of soft X-rays was found to be 10% or less as well as a buffer method.

## Introduction

X-ray source generated from laser produced xenon plasma has a broad-band spectrum, and it would become a compact and high efficiency soft X-ray source. We achieved a generation of the soft X-ray (5-17nm) of  $20\text{W}/2\pi\text{Sr}$  by using a rotating drum xenon cryogenic target<sup>[1]</sup> and a 100W/320pps Nd:YAG slab laser system<sup>[2]</sup>. Furthermore a focusing of soft X-ray, which improved its intensity by 27-times ( $1.26\text{mJ}/\text{cm}^2 @ 1\text{mm}\Phi$ ) compared with that without focusing<sup>[3]</sup> was accomplished by using a cylindrical ruthenium mirror system under the single laser pulse operation. However to use this mirror system at the operation condition of 100W/320pps, the mirror sputtering effect by xenon plasma debris must be mitigated because it causes a deterioration of the mirror reflectivity. We used an argon buffer gas which had a low absorption ratio of soft X-ray from xenon plasma and was able to mitigate the sputtering. The sputtering caused by the xenon debris was able to be mitigated to 1/18 on the condition of the argon gas of 8Pa filled thoroughly in the chamber.

In this paper, we report on a mitigation effect of plasma debris from xenon cryogenic target by an argon jet which can be increased the gas density locally.

## Experiments and Results

The experiment arrangement is shown in Fig.1. Nd:YAG Slab laser was used, and the laser pulse was focused on a rotating drum xenon cryogenic target at incident normal. The laser energy was 0.3 J with a pulse duration of 20 ns at 160pps or single pulse operation. The position of focus lens was  $LP=5\text{mm}$  where the conversion efficiency maximized. The rotating drum was operated at 130rpm and its vertical movement velocity was 3mm/s at 30mm width. A thickness of xenon layer was adjusted about  $500\mu\text{m}$  by two wipers inside the drum cover and fresh surfaces were supplied in each shot. An argon buffer gas was supplied by using a nozzle with a inside diameter of  $0.75\text{mm}\Phi$  near the source. A SUS wall with a thickness of  $400\mu\text{m}$  and

10mm width was placed in front of the nozzle to increase the argon density of that position. In order to evaluate a debris mitigation effect by the argon jet, we measured a sputtering rate in a gold film coated on a Quartz Crystal Micro-balance (QCM) which was mounted at 45 degree and a distance of 73 mm from a light source point. The soft X-ray energy was measured by an X-ray calorimeter at 45 degree and a distance of 190mm from the source. The ion debris was measured by a charge collector at 45 degree and a distance of 73mm.

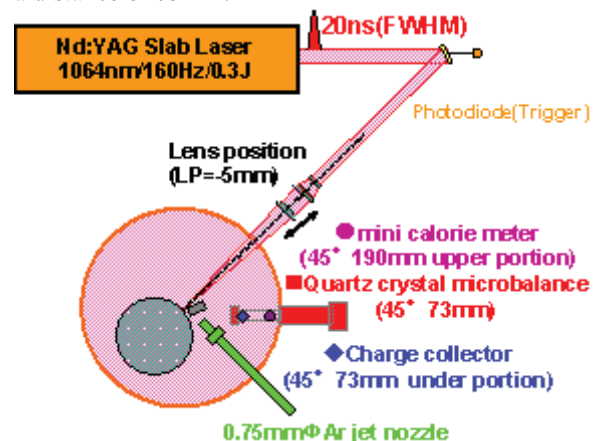


Fig.1 Experimental Setup

Fig.2 shows the result of measurements by QCM. The sputtering by xenon debris was mitigated to be 1/50 when the argon gas flow was 0.75L/min. At this time, the wave of charge collector signal shown Fig.3 was delayed and increased the width of the time. However the integer of the charge collector signal that means the number of ions was not so decrease. These results suggest that a decrease in the energy of the colliding particle mainly contributed to the mitigation rather than a decrease of the number of ions. In addition, the attenuation of soft X-rays was 10% or less as well as a buffer method. It is proven that the jet method effectively mitigates the plasma debris. If the attenuation up to 10% can be allowed, the debris mitigation of about 1/500 will be achieved.

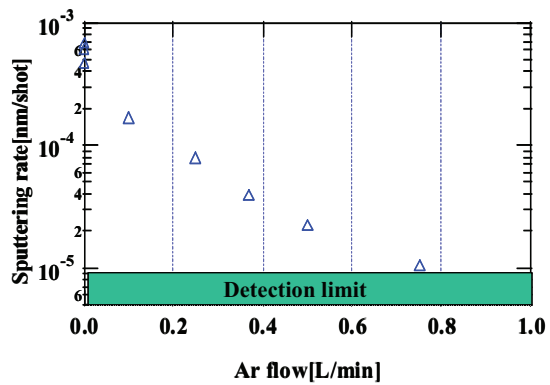


Fig.2 the mitigation effect of gold film sputtering rate as a function of argon flow.

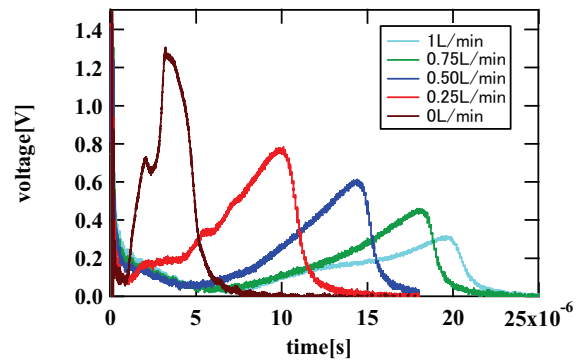


Fig.3 ion signal measured by charge collector

### References

- [1] K.Fukugaki *et al* , Rev. Sci. Instrum. **77**, 063114 (2006)
- [2] S.Amano *et al* , Rev. of Laser Engineering, Vol.**29**, pp.679-682 (2001)
- [3] T.Inoue *et al* , Lasti annual report vol.**10** p27-28(2008)

# Propose of Three-dimensional Micro Fluidics Device Using Centrifugal Force

Yuichi Utsumi\*, Tsukasa Azeta\*, Yoshiaki Ukita\*\*and Saki Kondo\*

\*Laboratory of Advanced Science and Technology for Industry, University of Hyogo, Japan

\*\*School of Materials Science, Japan Advanced Institute of Science and Technology, Japan

## Abstract

Lab-on-a-CD enables automation of chemical operations for overall assay protocol [1, 2], however there is strong restriction to the lab-on-a-CD, due to limited area for integration of multiple and multiple reactor units and different modules. This paper reports a new concept of lob-on-a-CD with three-dimensional (3D) microchannel interconnection, which enables fast, high-sensitive and high-throughput analysis.

## Introduction

There have been paid much attention to the lab-on-a-CD for the use of enzyme-linked immunosorbent assay (ELISA), due to its convenience for the automation of multiple microreactors. However it is difficult to simultaneously realize the performance and integration of multiple reactor units due to the limited chip area. One of the biggest problem arise from the limitation is inadequate sensitivity due to shortage of surface area for the immobilization of antibody. To resolve these problems, we propose a new type lab-on-a-CD concept based on three-dimensional (3D) microchannel network.

The important contributions of the 3D structure are summarized in two types of benefits as listed in below.

1. As shown in fig.1, stack concept of lab-on-a-CD contributes to the large-scale integration of various modules and reactor systems by stacking various layers of disks with different functions. Seven multiple reservoirs with different functions are integrated and connected each other with 3D microchannel network. It is notable that we succeeded in to increase the density of integrated microreactor unites by utilizing three-dimensionally stacked layers.
2. Flexibility of structural design, arises from 3D microstructure, enhances of performance of various modules. For example our device has 3D scaffolds for the immobilization of antibody onto the surface [3], and stacked structure of 3D detection reservoir resulting in the increase of signal-to-noise ratio as shown in fig. 2.

To realize the concept, the most important key-technology is a controlling of “vertical” liquid transportation which enables transfer of reagents between different layers of the stacked CD.

To investigate the feasibility of the valving and liquid transportation by centrifugal force, computational fluid dynamics (CFD) using “FLUENT” software is carried out. We assumed the

driving force arisen from spinning speed from 0 rpm to 2000 rpm. As shown in fig. 3(a), the liquid is held by surface tension with spinning speed less than 1000rpm and it becomes transported through capillary bundle structure with spinning speed greater than 1000rpm. The results suggest possibility of vertical liquid transportation through vertical capillary bundle structure by converting the planar centrifugal driving force into isotropic pressure to drive the liquid in vertical direction.

## Experiments and Results

The poly-dimethylsiloxane (PDMS) disks with planer microchannels are fabricated by conventional rapid prototyping and poly-methylmethachrylate (PMMA) disks are fabricated by deep X-ray lithography as shown in fig. 4[3]. To construct 3D microchannel network, these disks are aligned and reversibly bonded.

To demonstrate the automatic sequencing in 3D CD platform, we loaded pure water and stained into the reservoirs and CD platform is spun for the sequencing. The burst frequency and flow behaviors are measured and observed by using strobe scope system. The four step flow sequencing involving vertical liquid flow around reaction reservoir are successfully demonstrated. As shown fig. 5, the reproducibility is indeed good between 8 individual measurements.

Achieved flow sequencing driven by controlled centrifugal force in 3D fluidic interconnection is expected to realize high-efficiency and high-throughput total assay on one platform.

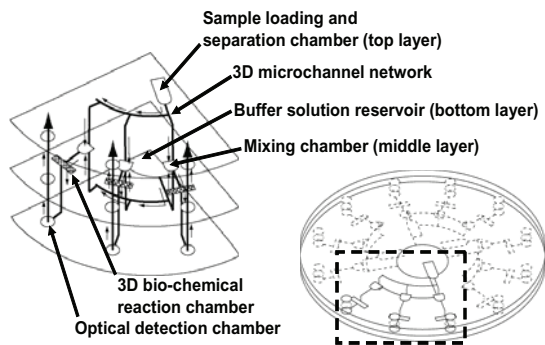


Figure 1. Schematic diagram of new CD-like microfluidic platform with three-dimensional fluid network

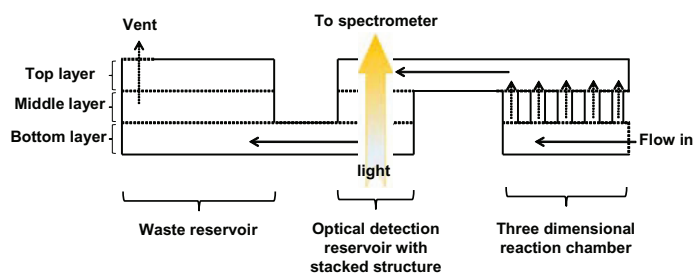


Figure 2. Cross sectional view of three-dimensional microchannel interconnection

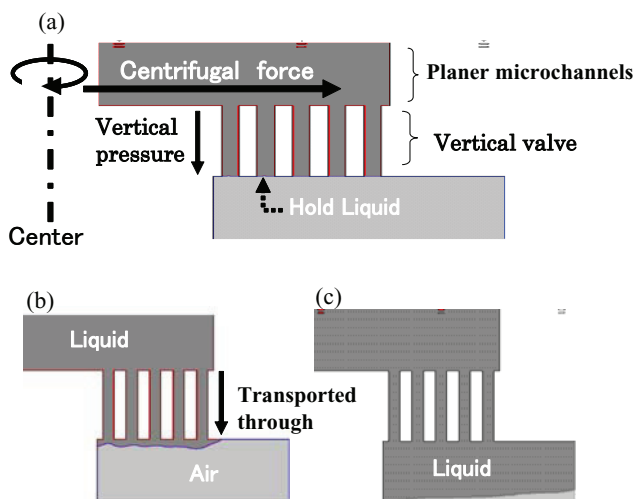


Figure 3. Analysis model of three-dimensional structure by centrifugal force.  
 (a) Liquid is held by surface tension. [500rpm]  
 (b), (c) Centrifugal force was over surface tension [over 1000rpm].



Figure 4. Photographs of designed and fabricated CD platform consist of three layers

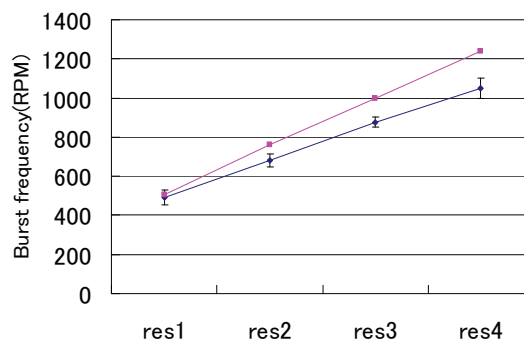


Figure 5. (a) Images of flow sequencing of water  
 (b) Measured burst frequency

**REFERENCES:**

- "Design of a Compact Disk-like Platform for Enzyme-Linked Immunosorbent Assay," S. Lai, S. Wang, J. Luo, L. J. Lee, S. T. Yang, and M. J. Madou, *Analytical Chemistry*, **76**, 1832 (2004)
- "A fully automated immunoassay from whole blood on a disk" B. S. Lee *et al.*, *Lab Chip*, **9**, 1548, (2009)
- " Proposal of a new microreactor for vertical chemical operation," Y. Utsumi, T. Asana, and Y. Ukita, *Japanese Journal of Applied Physics*, **45**, 2606 (2006).

# Fabrication of electrodes for multiplex neural interface

Mitsuhiro Yoshida\*, Yoshiaki Ukita\*, Kunihiro Mabuchi\*\*, Yuichi Utsumi

\*Laboratory of Advanced Science and Technology for Industry, University of Hyogo

\*\*Dept. of Information physics & Computing, Grad. School of Info. Sci. & Tech. The University of Tokyo

## Abstract

“Microneurography” developed by Karl-Erik Hagbarth and Ake B.Vallbo, is a technique for reading and manipulating nerve signals by tools, acting as “nerve signal interfaces”<sup>[1]</sup>. The “flexible regeneration type nerve electrode” is an interface device for nerves, connecting nerve fibers to signal conducting lines on a macro structure, making it usable for “Microneurography”<sup>[2]</sup>. Our chips buildup is based on multiple stacked SU-8-layers.

## Introduction

Information on the neural system is expressed by the action potential transmitted in the neuronal cell. This neural coding can be measured by mounting the electrode in the neighborhood of the neuronal cell or the neuronal cell. More, it is also possible to stimulate the neuronal cell oppositely, and to generate the neural coding. Such an electrode is called a nerve electrode. It becomes possible to analyze the function of the neural system by measuring the neural coding. And, a multi activity of a cell simultaneous metrology that records the activity of two or more neuronal cells at the same time is paid to attention. There is a nerve regeneration type electrode using the ability of regeneration for the peripheral nerve to make the action potential transmitted in the neuronal cell a multi channel. The model of the nerve regeneration electrode is shown Fig.1 Flexible regeneration type nerve electrode relies on the regeneration ability of nerves. By putting a pair of cut nerves at both ends of a capillary, they grow through the capillary to reconnect. When an electrode is embedded inside of the capillary, it become possible to detect the potential of nerves by the electrode. This method is suitable to detect signals inside and outside of the nerve fiber. The development of implantable neural interface will realize brain-driven prosthetic limb and the artificial organ, or its also possible to apply to scientific application such as understanding of biological functions of nerves.

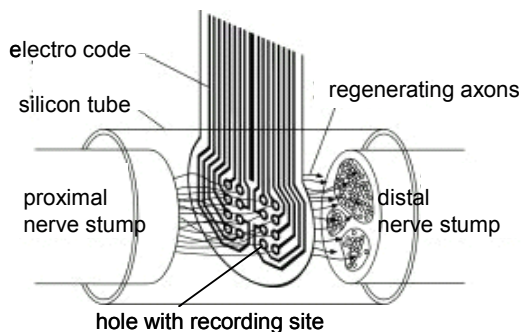


Fig.1 Model of nerve reproduction electrode

## Design

Fig.2 (a) shows the outline of the nerve regeneration electrode. To increase the number of electrodes we propose stacked type electrode structure. It is difficult to integrate many electrodes by using single layer due to small area. Thus the electrode shape is designed to be stacked allowing three-dimensional (3D) crossing of multiple electrode lines. For the first attempt, designed electrode structures have 12 channels electrode on a single layer and total 24 channels are realized by stacking two layers. Fig.2 (b) shows the designed nerve reproduction electrodes.

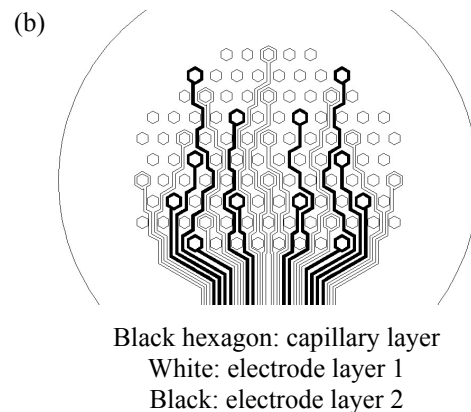
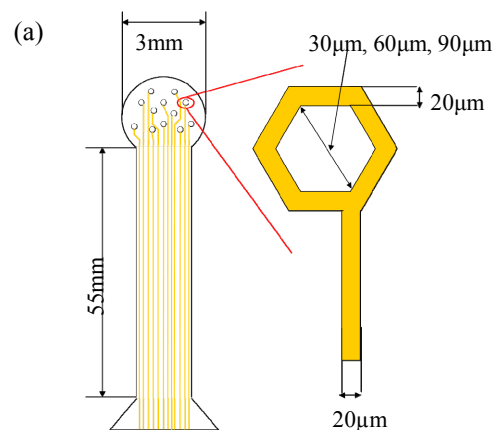


Fig.2 (a) Outline of electrode

(b) Designed nerve reproduction electrodes

## Experiments

Our chips buildup is based on multiple stacked SU-8-layers. The prepared single layer electrode chips are piled up together with the precise alignment and bonding process. Fig.3 shows the fabrication process image of bonding. For the bonding process the unique characteristic of SU-8 is utilized for the patterning of capillaries and bonding<sup>[3]</sup>.

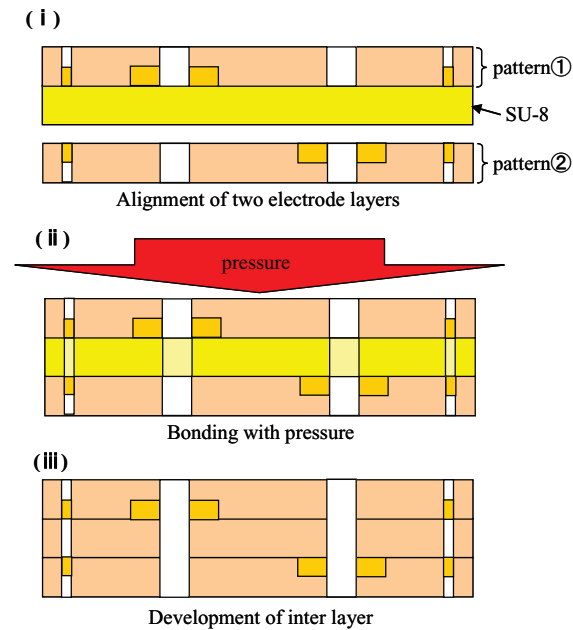


Fig.3 Fabrication process image of bonding

## Results

Fig.4(a) shows photographs of outer view fabricated electrodes. Fig.4(b) shows photographs of zoom up of structure of electrodes. As shown in Fig.4(b) the three-dimensionally stacked electrodes and through capillary for nerve growth are successfully aligned and patterned in monolithic SU-8 chip. We inspected the method to manufacture it for three-dimensions to realize the multi channel of the flexible regeneration type nerve electrode in this study and demonstrated that it was possible for the first time. We will aim at the optimization of the structure parameter and the multistage of the stacking step and the advancement of the fabrication process in future. Moreover, it is necessary to verify it by measuring an actual neural coding by mounting.

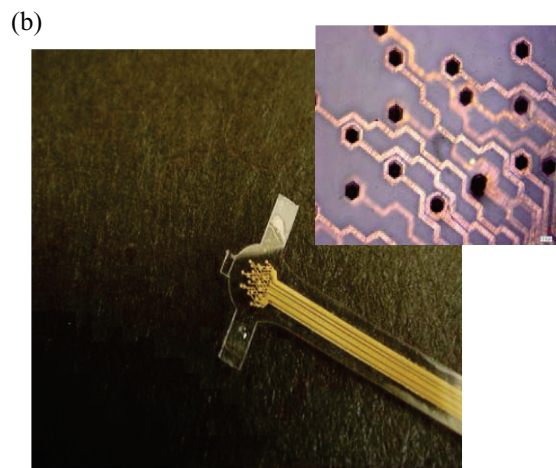
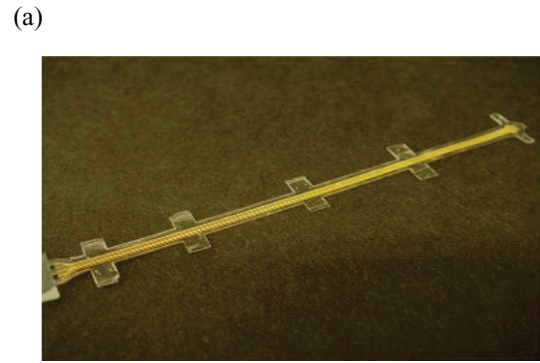


Fig.4 (a) Outer view fabrication electrodes  
(b) Zoom up of structure of electrodes

## References

- [1] Åke B. Vallbo, Karl-Erik Hagbarth, and B. Gunnar Wallin : “Microneurography: how the technique developed and its role in the investigation of the sympathetic nervous system”, *J Apply Physiol* 96, p.1262-1269 (2004)
- [2] Takafumi Suzuki, Takashi Saito, Kunihiko Mabuchi : “Development of a multi-channel nerve electrode for peripheral nervous system”, *Technical report of IEICE*, Vol. 100, No. 479 pp.63 -66 (2000)
- [3] F J Blanco, M Agirregabiria, J Garcia, J Berganzo, M Tijero, M T Arroyo, I Aramburu and Kepa Mayora : “Novel three-dimensional embedded SU-8 microchannels fabricated using a low temperature full wafer adhesive bonding”, *J.Micromech..Microeng*, Vol. 14, pp.1047 -1056 (2004)

# HIGH EFFICIENCY MICROFLUIDIC REACTOR CHIP OPERATED ONLY USING SURFACE-ACOUSTIC-WAVE

Takeshi Komoto\*, Tsunemasa Saiki\*\*\*, and Yuichi Utsumi\*

\*Laboratory of Advanced Science and Technology for Industry, University of Hyogo, Japan

\*\* Hyogo Prefectural Institute of Technology, JAPAN

## Abstract

Surface acoustic wave (SAW) devices are expected for micro total analysis systems, because their structures are simple. We studied flow actuators driven by SAWs. We then fabricated a micro-mixer driven by the SAWs. In this study, on the basis of the mixer and the flow actuator, we proposed and fabricated a novel micro-reactor driven by the SAWs, and investigated its reaction property. As a result, we found that the local rapid mixing of micro solutions was possible by using the SAWs, and high availability of our micro reactor was demonstrated.

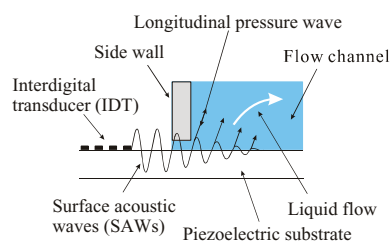
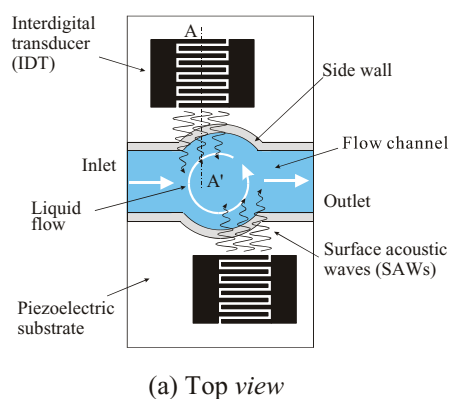
## Introduction

The manufacturing process for each component device in a lab on a chip must be simplified to integrate multiple functional devices. Surface acoustic wave (SAW) devices with very simple structures have attracted attention. Therefore, we studied SAW actuators that could enable a continuous liquid to flow with high efficiency [1] and enable a small amount of liquid to be rotated at high revolution [2]. The knowledge obtained from our previous research enabled us to fabricate a high efficiency microfluidic mixing chip [3]. In this study, we evaluated the chemical reactivity of the chip.

## Structure of our reactor

The top view and magnified sectional view of our micro reactor operated using SAWs are shown in Figure 1 (a) and (b). SAWs are generated from the IDTs when high frequency voltage is applied to interdigital transducers (IDTs). The SAWs propagate in the surface layer of the substrate and pass through a sidewall to the bottom plate of the flow channel. The liquid in the flow channel then becomes energized due to longitudinal pressure wave radiation from the SAWs and flows in the propagated direction of the SAWs. Overall, the liquid in the reactor flows with some rotation in a stream from the inlet to the outlet through external pumps.

A photograph of a microfluidic reactor (mixing) chip operated using SAWs is shown in Figure 2. The chip consists of one y-type flow channel, three reservoirs, one reactor, and two pumps. Not only the micro reactor but also the pumps were driven in the microfluidic chip using SAWs. The flow channel widths upstream and downstream of the merging point were 0.5 mm and 1 mm. The depth of the flow channel was approximately 250  $\mu\text{m}$ . The IDTs of the reactor and the pumps had pitches of 200  $\mu\text{m}$ , 20 pairs, and apertures of 0.5 mm.



(b) Magnified sectional view (A-A')

Figure 1. Overview of micro reactor operated using SAWs.

## Experiments

Our experimental setup for investigating the reaction characteristic of the microfluidic chip is shown in Figure 3. Before starting the experiment, we filled reservoir 1 with solution A, which was a mixture of 10% NaOH water solution of 15  $\mu\text{L}$  and 0.075 mg of luminol reagent, and filled reservoir 2 with solution B, which was a mixture of 7.5 vol%  $\text{H}_2\text{O}_2$  water solution of 15  $\mu\text{L}$  and 0.45 mg of potassium ferricyanide. In the experiment, these solutions flowed through the two pumps, which operated simultaneously. We then took photographs of the liquid behavior in the reaction area using a highly sensitive camera.

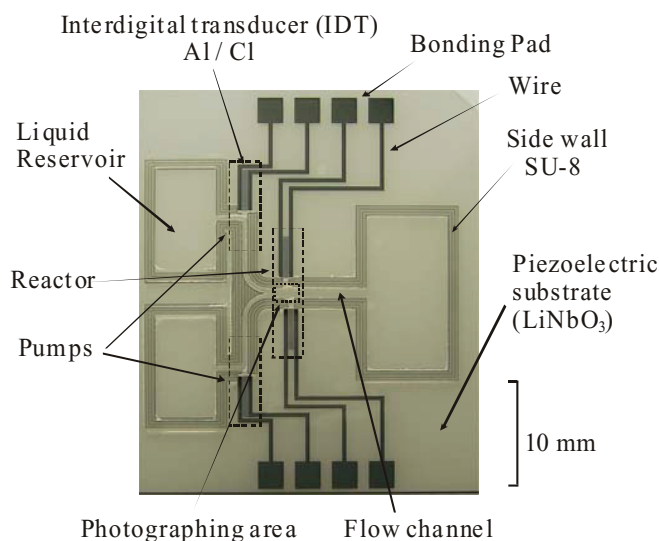


Figure 2. Photograph of microfluidic reactor chip operated using SAWs.

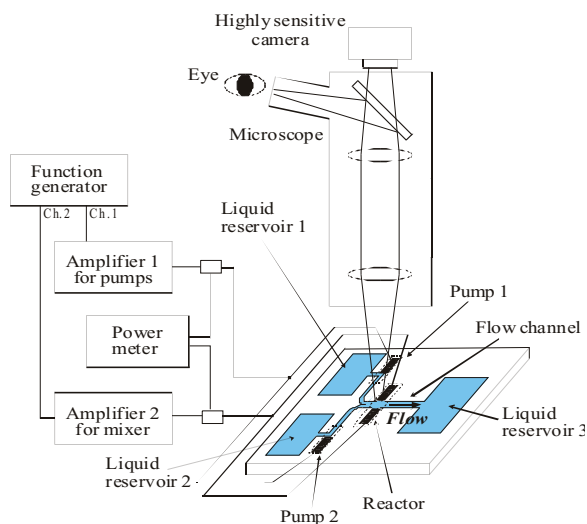
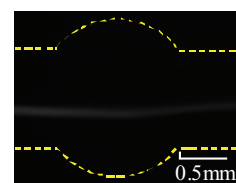


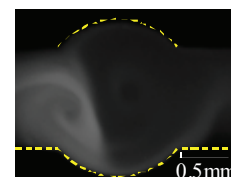
Figure 3. Experimental setup.

### Results

The photographs of luminol luminescence in the reaction area are shown in Figure 4. Here, the flow velocities in the channels were about 5 mm/sec, and driving power  $P_R$  of the micro reactor was 250 mW. When the micro reactor did not operate, only one line of luminescence was observable near the center of the flow channel. However, when the micro reactor did operate, luminescence occurred in the whole flow channel. These observations demonstrated that local and rapid mixing of these solutions was possible by using the SAWs. Moreover, our micro reactor demonstrated high applicability.



(a) Non-operation of reactor (PR=0mW)



(b) Operation of reactor (PR=250mW)

Figure 4. Photographs of luminescences with luminol reactions.

### REFERENCES:

1. "Proposal of a Novel Continuous Flow Pumping Operated by Surface Acoustic Wave," Y. Utsumi, T. Saiki, K. Okada, 12th International Conference on Miniaturized Systems for Chemistry and Life Sciences ( $\mu$ TAS2008), 715 (2008).
2. "Fabrication and Estimation of Novel Micro Liquid Rotor that Operates with Surface-acoustic-wave," T. Saiki, K. Okada, Y. Utsumi, 12th International Conference on Miniaturized Systems for Chemistry and Life Sciences ( $\mu$ TAS2008), 387 (2008).
3. "High Efficiency Mixing and Pumping of Continuous Liquid Flow using Surface-Acoustic-Wave," Y. Utsumi, T. Saiki, K. Okada, 13th International Conference on Miniaturized Systems for Chemistry and Life Sciences ( $\mu$ TAS2009), 58 (2009).

# High-sensitive enzyme-linked immunosorbent assay in three-dimensional lab-on-a-CD

Yoshiaki Ukita, Laboratory of advanced science and technology for industry  
Tsukasa Azeta, Laboratory of advanced science and technology for industry  
Saki Kondo, Laboratory of advanced science and technology for industry  
Yuichi Utsumi, Laboratory of advanced science and technology for industry

## Abstract

This paper reports a new lab-on-a-CD with three-dimensional(3D) microchannel network for the highly versatile and automatic immunoassay system. The lab-on-a-CD is consist of disks with planer microchannels and vertical channels, which fabricated by using conventional rapid prototyping method and x-ray lithography. The three dimensional lab-on-a-CD is applied to ELISA with standard sandwich protocol. The results suggest quite low detection limit (the several ng/ml order detection limit of immune globlin G of mouse).

## Introduction

The lab-on-a-CD is promising for the automation of multiple microreactor systems. Recently, high-performance systems based on lab-on-a-CD has been proposed [1, 2]. However it is difficult to simultaneously realize the integration of many reactor units and various modules due to the restriction of chip size. In fact, the lab-on-a-CDs proposed by the references are integrating a few systems [1, 2].

To resolve this problem, we propose a new type lab-on-a-CD concept based on three-dimensional (3D) microchannel network. Figure 1 shows schematic illustration of 3D lab-on-a-CD consists of multiple layers of CD-like disks with different functions. By stacking multiple layers of lab-on-a-CD, it can compactly be integrated microreactor systems. It is also notable that the use of three-dimensional structure enhances the performance of modules. For example, it can be realized to improve the sensitivity of ELISA by increasing surface area for the immobilization of antibody, and optical path length is also increased by utilizing stacked structure as shown in fig. 1(b).

## Experiments and Results

To demonstrate the ELISA, we carried out the sandwich ELISA by means of standard sandwich ELISA in fabricated 3D lab-on-a-CD. Planer PDMS lab-on-a-CD and through-hole PMMA lab-on-a-CD are fabricated by rapid prototyping and deep X-ray lithography respectively, and figs. 2(a, b) show the photograph of the disks and SEM images of bundle-like capillary structures.

To estimate the immobilization and specificity of antibody, we compared three different reaction conditions in the lab-on-a-CD. As shown in fig. 4, the absence of 1st antibody or absence of analyte result in low level signal, and presence of immobilized 1st antibody and analyte result in the higher signal. This result suggests successful immobilization of antibody with sufficient activity on the capillary bundle structure. It is also

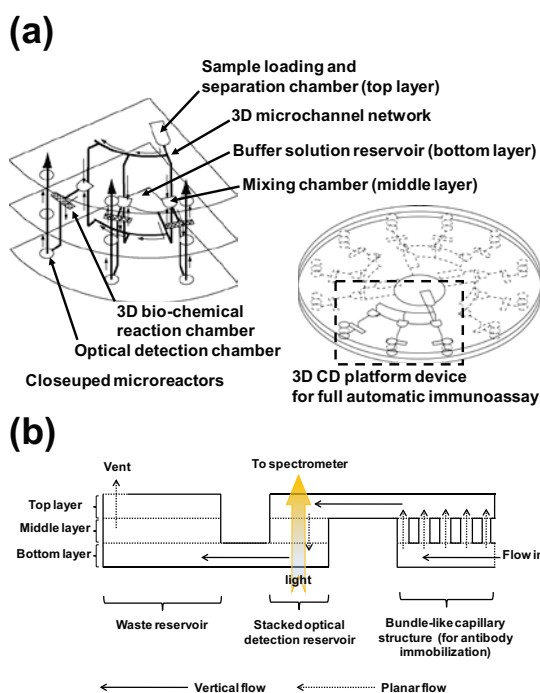


Figure 1: The schematic illustration of three-dimensional lab-on-a-CD. (a) Multiple layers with different functions are stacked and integrated together, to construct high-performance assay system. (b) Cross section of the 3D reaction chamber and optical detection reservoir.

notable that we succeeded in on-chip detection by means of absorption spectroscopy in three-dimensionally stacked detection reservoir with optical path of 700 $\mu$ m.

It is also very important to realize the on-chip washing for the automation. Prof. Madou's group reports the consumed volume of wash is three-times of the reaction reservoir, however it is concerned that the complex flow behavior in bundle-like capillary structure result in the difficulty of the washing. Thus we demonstrated and compared the results of ELISA by on-chip

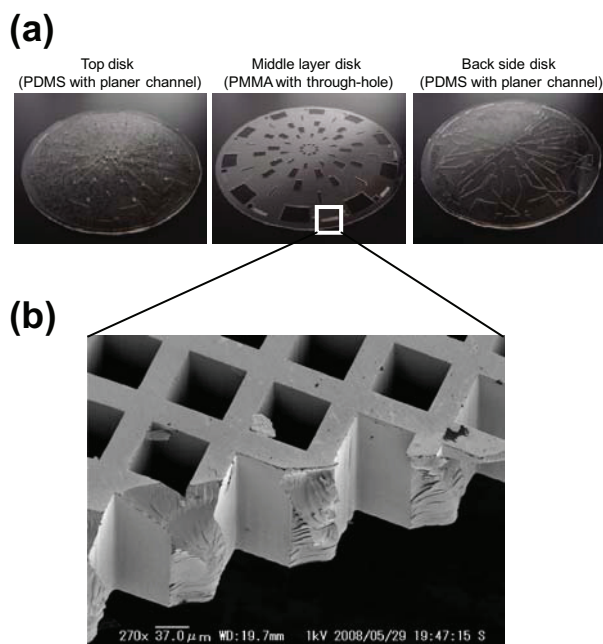


Figure 2. (a) Photographs of fabricated disks of 3D lab-on-a-CD. (b) SEM image of bundle-like capillary structure for antibody immobilization.

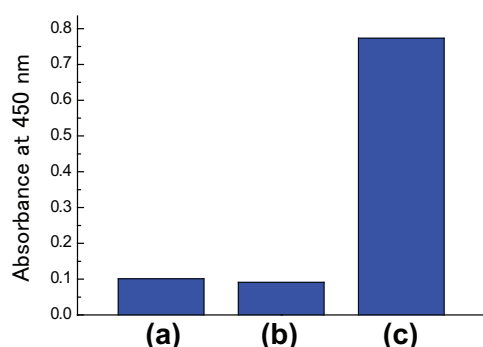


Figure 3. Comparison of three different reaction conditions. (a) with 1<sup>st</sup> antibody, and without analyte (Mouse IgG) (b) without 1<sup>st</sup> antibody, and with analyte (10 μg/ml of Mouse IgG) (c) with 1<sup>st</sup> antibody, and with analyte (10 μg/ml of Mouse IgG)

and off-chip washing step.

As shown in fig. 5, we successfully detected reasonable dose response of the signal reflecting the concentration of analyte. The corresponding assays to the each plot in the fig. 5 were simultaneously carried out and detected by on-chip absorption spectroscopy and the result also suggests stable filling of capillary bundle by centrifugal pumping. The estimated detection limit is quite sensitive less than several ng/ml and oval reaction time is less than 25 min. By comparing the results of on-chip washing and off-chip washing, it is very encouraging that the result of on-chip washing also exhibit clear dose response and plot of 1 ng/ml analyte is quite close to the back ground level of off-chip washing. We

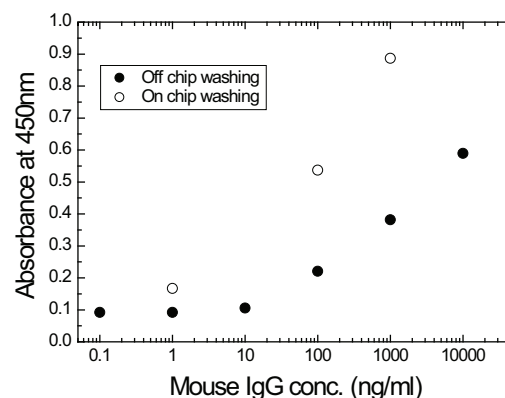


Figure 5. Obtained calibration curve by using three-dimensional lab-on-a-CD. The mouse IgG (analyte) is sandwiched by anti mouse IgG goat IgG and enzyme conjugated (HRP) anti-mouse IgG goat IgG. The signal of the enzyme reaction is amplified by high-sensitive peroxidase substrate (TMBZ). Closed plots are taken by off-chip washing protocol, and opened plots are taken by on-chip washing protocol.

believe that the on-chip washing is effectively controlling the back ground due to nonspecific binding of proteins.

#### References

- [1] B. S. Lee *et al.*, 1. "A fully automated immunoassay from whole blood on a disk", *Lab Chip*, **9**, 1548, (2009)
- [2] S. Lay *et al.*, 2. "Design of a compact disk-like microfluidic platform for enzyme-linked immunosorbent assay", *Anal. Chem.*, **76**, 1832, (2004)

# Mask Observation Results using a Coherent EUV Scattering Microscope at NewSUBARU

Tetsuo Harada<sup>a)</sup>, Junki Kishimoto, Takeo Watanabe, Hiroo Kinoshita

LASTI, University of Hyogo, 3-1-2, Koto, Kamigori, Ako, Hyogo, Japan 678-1205

JST, CREST, Japan

Dong Gun Lee

Samsung Electronics Co., LTD., San #16 Banwol-Dong, Hwasung-City, Gyeonggi-Do, Korea, 445-701

<sup>a)</sup> Electronic mail: harada@lasti.u-hyogo.ac.jp

A coherent scattering microscope for extreme ultraviolet (EUV) light has been developed for the actinic inspection of EUV lithography masks. It was installed at the NewSUBARU synchrotron facility. It provides aberration-free, diffraction-limited imaging and a high numerical aperture. Coherent EUV light scattered (diffracted) from a mask is recorded using a CCD camera with a numerical aperture of 0.15. An image of the sample is reconstructed using a hybrid input-output algorithm, which retrieves the phase from the intensity data. Masks containing periodic line-and-space and hole patterns with a half pitch ranging from 100 nm to 400 nm were fabricated in our laboratory and imaged. The reconstructed images correlate well with images obtained with a scanning electron microscope (SEM). The actinic critical dimension of the line width of TaN absorber patterns on a mask was measured and was consistently found to be 25 nm larger than that obtained from the SEM data.

## I. INTRODUCTION

Extreme ultraviolet (EUV) lithography is a promising technology for the production of semiconductor devices at the 32-nm node. The fabrication of a defect-free mask is a critical issue. An EUV mask consists of a glass substrate with a reflective multilayer coating and a patterned absorber coating. A Mo/Si multilayer exhibits a high reflectivity of 70% at  $\lambda = 13.5$  nm, which is the working wavelength of EUV lithography. The required accuracy of the critical dimension (CD) for the 32-nm node is less than 2.6 nm.<sup>1</sup> To achieve that level of accuracy, it is necessary to be able to precisely determine the line width of a mask pattern. Thus, at-wavelength observations with an EUV microscope is essential for estimating the actinic CD of the reflection profile. There are two types of defects in EUV lithography masks: amplitude defects, which are caused by particles on the surface of a mask, and phase defects, which are caused by defects in the substrate and particles in the multilayer. To detect phase defects on mask blanks, SELETE has developed a dark-field inspection tool employing Schwarzschild optics and a laser plasma source<sup>2</sup>. To inspect finished (patterned) masks, the LBNL group has developed an actinic inspection tool that employs a Fresnel zone plate as an optical component.<sup>3,4</sup> It is installed at the ALS synchrotron facility. This microscope has a numerical aperture (NA) of 0.0875

and a field diameter of 5  $\mu\text{m}$ , and can estimate CDs ranging from 100 nm to 500 nm. However, aberration makes it difficult to obtain a high NA at the Fresnel zone plate. We have developed an EUV microscope that employs Schwarzschild optics and an X-ray zooming tube,<sup>5,6</sup> and installed it at the NewSUBARU synchrotron facility. It has a high NA of 0.3 and a large field with a diameter of 50  $\mu\text{m}$ . Because of the low magnification (30 $\times$ ) of the Schwarzschild optics, the zooming tube uses electromagnetic lenses to magnify a projected mask image by 10-200 $\times$ . The optics for these actinic inspection tools are difficult to produce and align, and they become more complex as the NA and magnification become higher.

This paper describes a coherent EUV scattering microscope (CSM) based on X-ray diffraction microscopy.<sup>7,8</sup> It requires no objective and uses only coherent EUV light. The scheme is simple: Coherent EUV light illuminates a region of a patterned EUV mask, and an EUV CCD camera records the intensity distribution of the scattered (diffracted) light. In a conventional diffraction imaging setup, an objective collects both phase and amplitude information from the sample. In contrast, the CSM records only the diffraction intensity of the sample, which contains only amplitude information. The missing phase information is retrieved by using a hybrid input-output (HIO) algorithm,<sup>9</sup> which iteratively

calculates the Fourier transform and the inverse Fourier transform, subject to constraints.

The CD for a periodic mask can be determined from the intensity ratios of the zero, 1st, 2nd, and

## II. DESIGN OF COHERENT EUV SCATTERING MICROSCOPE

The CSM is installed on the BL-3C beamline<sup>10</sup> of the NewSUBARU synchrotron facility, which has a bending-magnet source. Two toroidal mirrors collimate the white light, and a Mo/Si multilayer deflects the beam at the C station by a designed angle of 0.75 mrad. This multilayer has a peak reflection wavelength around 13.5 nm at an angle of incidence of 10°. Figures 1 and 2 show a schematic and a photograph, respectively, of the CSM at the end station of the BL-3C; and Table 1 lists the specifications. The optical path in the CSM chamber begins with a 5- $\mu\text{m}$ -diameter pinhole and a 200-nm-thick Zr filter, which reduces the beam diameter and partially monochromatizes the beam. Next, a concave spherical mirror reflects the beam

higher diffraction orders, which makes the CSM a useful tool for quickly estimating the CD. The zero diffraction order means direct reflection from the mask.

(incident angle: 3°) and a planar mirror reflects it (incident angle: 39°) onto an EUV mask. The two mirrors are coated with 40 pairs of Mo/Si layers, which have a peak reflectivity of 43% at  $\lambda = 13.4$  nm, and 52% at  $\lambda = 13.5$  nm. The Zr filter, the three Mo/Si multilayers of the branching mirror, and the two mirrors of the CSM monochromatize the beam striking the EUV mask at a wavelength of 0.3 nm. When the CSM is used for estimating the CD, the results accurately take the shadowing effects of the absorber pattern into account because the angle of incidence on an EUV mask is 6°, which is the same as that for the alpha EUV exposure tools ADT (ASML) and EUV1 (Nikon).

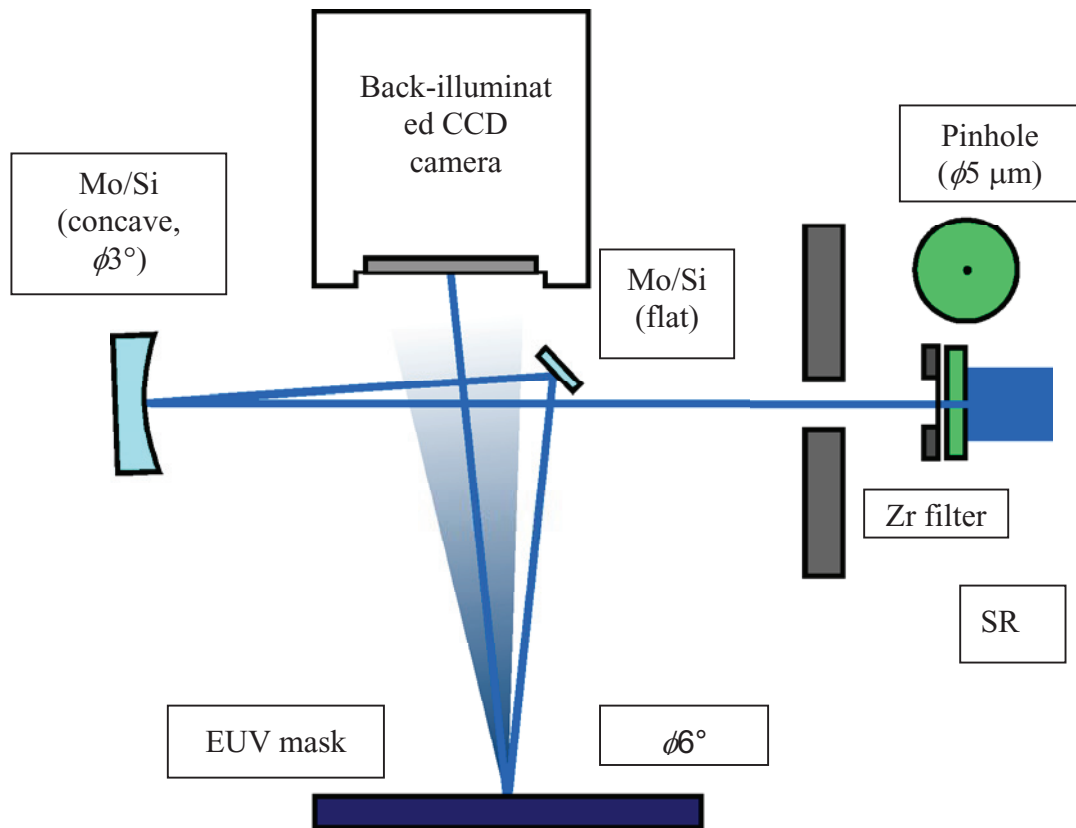


Figure 1. Schematic diagram of coherent EUV scattering microscope (CSM). All the optics, including the CCD camera, are inside the vacuum chamber.

Due to the off-axis illumination of the alpha tools, the CD includes the effects of shadowing by the absorber pattern. The concave mirror (radius of curvature: 163 mm) projects the pinhole image onto the mask. It is 163 mm from the pinhole and the same distance from the mask. Due to aberrations inherent in the use of a pinhole for imaging, the size of the pinhole was made significantly larger than the wavelength. The beam divergence is equal to the calculated diffraction angle. The area of the concave mirror that is exposed is less than a millimeter in diameter. The spot size calculated by means of a ray-tracing program that traced rays from the pinhole to the mask is 1  $\mu\text{m}$ . The pinhole image is almost the same size as the object, which limits the field size of the CSM. To obtain good contrast for the reconstruction of mask images, the diffraction field should be at least 5  $\mu\text{m}$  across to produce interference at the position of the CCD camera. The spatial coherence length of the incident beam is 18  $\mu\text{m}$ , as estimated from the divergence. This is substantially larger than the required field size.

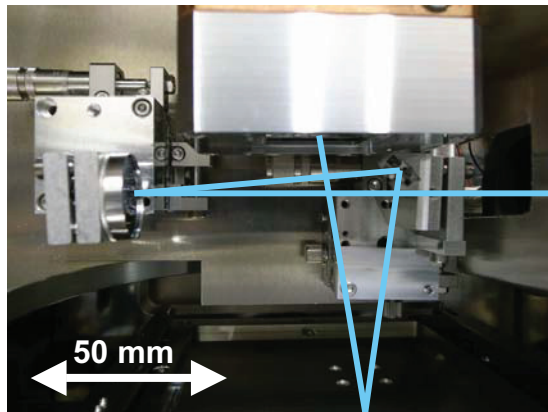


Figure 2. Photograph of coherent EUV scattering microscope (CSM). The solid line is the optical path of the SR light.

The CCD camera (MTE-2048B, Roper Scientific) can operate in a high vacuum and has a back-illuminated CCD without an anti-reflection coating. The surface of the CCD is parallel to the

surface of the mask. The imaging area is 27.6 mm square; it contains a 2048  $\times$  2048 array of imaging pixels, each of which is 13.5  $\mu\text{m}$  square. The CCD camera has a quantum efficiency of 42% for EUV photons and a 16-bit analog-to-digital converter. The camera is cooled to  $-50^\circ\text{C}$ . The RMS noise of the CCD was estimated to be 7 counts from counting dark frames for 5 minutes. The dynamic range was estimated to be 4 orders of magnitude. The distance from the mask to the CCD camera is about 92 mm, which is equivalent to an NA of 0.15. The estimated spatial resolution for this NA and coherent illumination is 90 nm. It can be improved by shifting the CCD camera so that it records higher diffraction orders. A 200-nm-thick Zr filter was placed just after the pinhole to remove the UV-visible components of the specular reflection from the Mo/Si multilayers. The CSM has a shadowgraph mode that uses visible light to align the mask. In this mode, a linear-stage is used to replace the Zr filter and the 5- $\mu\text{m}$ -diameter pinhole with a visible ND filter and a 4-mm-diameter pinhole. The mask X-Y stage can move  $\pm 60$  mm to enable observation of the whole area of an EUV mask of 6025 size with encoders. The step resolution for movement is 4  $\mu\text{m}$ . The CSM chamber has a load lock apparatus for sample exchange, which takes about one hour.

Table 1. Specifications of coherent EUV scattering microscope.

Light source	White SR light (Bending)
Center wavelength	13.5 nm
Bandwidth	0.3 nm
Field size	$\phi 5 \mu\text{m}$
Incident angle	$6^\circ$
Numerical aperture	0.15
Spatial resolution	45 nm hp
Mask size	6025 glass substrate
Imaging device	Back-illuminated CCD

### III. FABRICATION OF EUVL MASK PATTERNS

Test EUV masks were fabricated to evaluate the CSM specifications. Since coherent EUV scattering microscopy is a new technique for observing EUV masks, various types of masks with a variety of patterns and phase defects are needed for the evaluation. In this study, we fabricated standard line-and-space (L/S) and hole patterns to develop our fabrication technique. The masks consist of a Si substrate, a Mo/Si multilayer coating, and a TaN absorber layer. The Mo/Si multilayer has 40 6.9-nm-thick periods; and the ratio of the Mo layer thickness to the period thickness is 0.4. The TaN layer is 80 nm thick and has a calculated reflectivity of less than 0.1%. In the mask fabrication process (Fig. 3), first a Si substrate is coated with a Mo/Si multilayer by magnetron sputtering (MPS-4500, ULVAC). Next, the TaN layer is deposited; and a spin coater covers it with a 200-nm-thick layer of

ZEP520A resist. Electron beam lithography (ELS-7500, ELIONIX) is used to write the pattern in the resist; and the mask is etched by ICP dry etching (TCP 9400SE Alliance, Lam Research). Three types of patterns were fabricated: horizontal and vertical L/S patterns, and holes. The half pitch (hp) ranged from 50 to 500 nm. Each pattern was formed on a 20- $\mu\text{m}$ -square area, which is larger than the field size ( $\phi$  5  $\mu\text{m}$ ). Forty-eight patterns were fabricated in each 300- $\mu\text{m}$ -square block (Fig. 4). Nine blocks were fabricated on a 4-inch Si wafer, along with alignment marks to make alignment of the mask easy. The alignment marks are useful for locating the position of a pattern in the shadowgraph mode of the CSM. Regarding the fabrication results, the 50-nm-hp patterns collapsed due to the high aspect ratio of the resist. The 60-nm-hp and 200-nm-hp patterns were fabricated successfully (Fig. 5). A half pitch of 60 nm on a mask is equivalent to a half pitch of 15 nm for semiconductor devices.

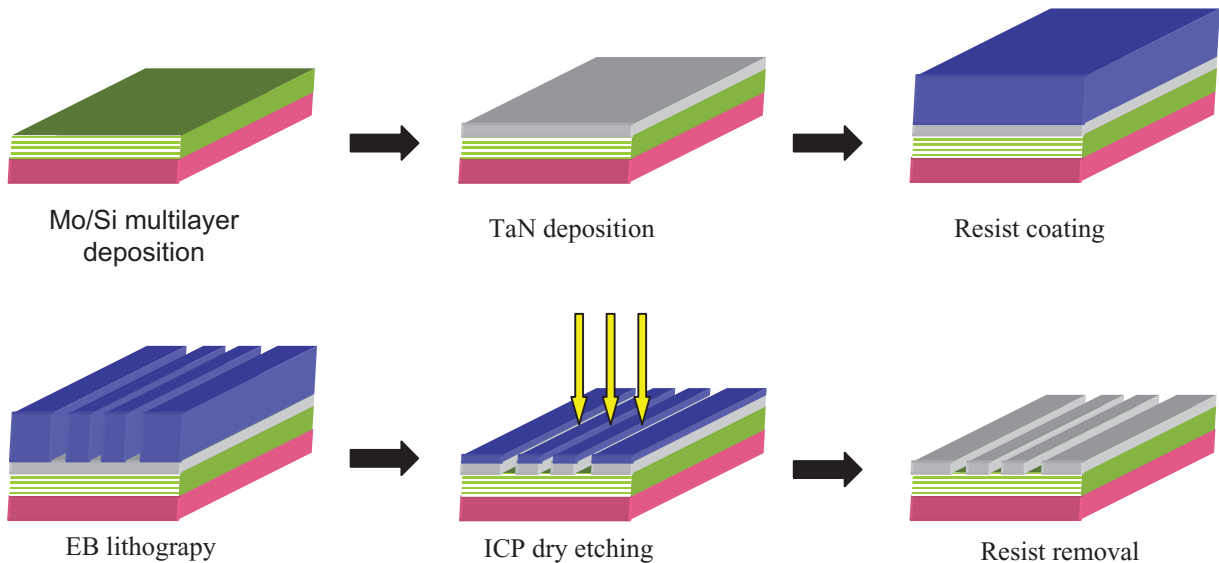


Figure 3. Fabrication process for EUV mask.

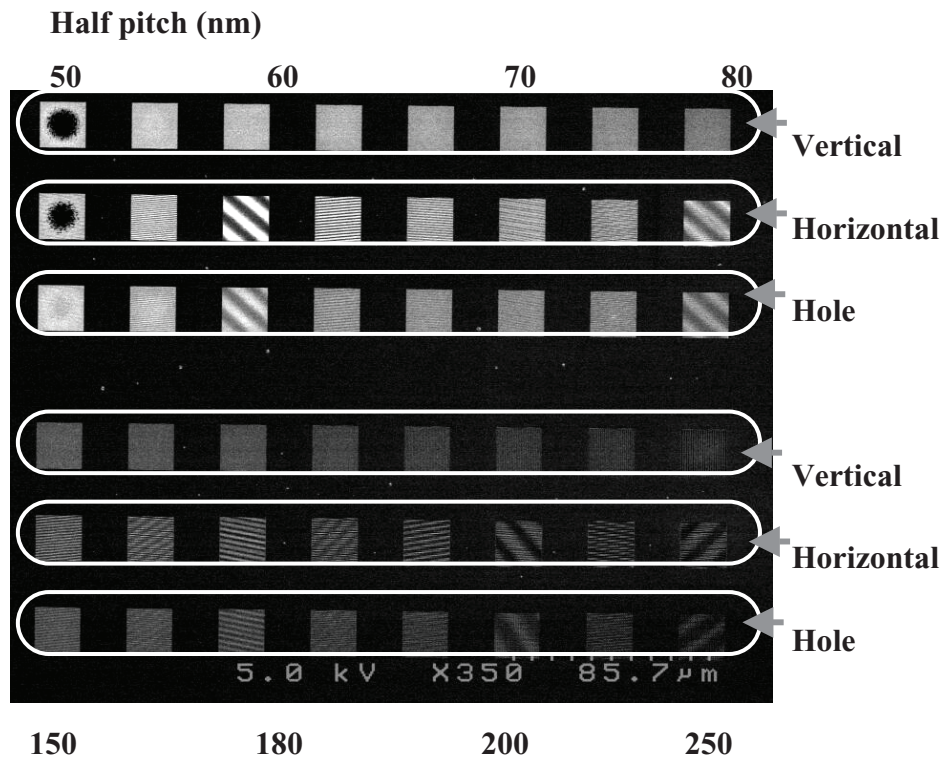


Figure 4. SEM image (top view) of fabricated EUV mask. Each square is about 20  $\mu\text{m}$  on a side. There are 48 squares containing vertical L/S, horizontal L/S, and hole patterns with half pitches ranging from 50 nm to 500 nm.

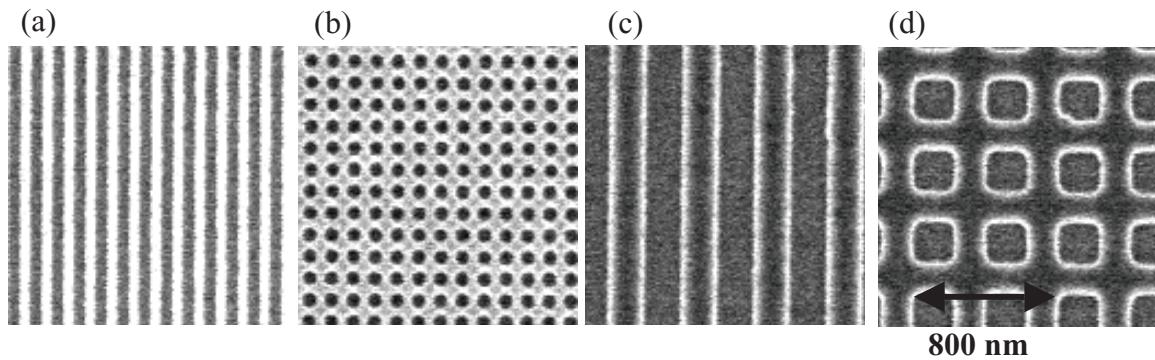


Figure 5. SEM images of fabricated EUV mask: (a) 60-nm-hp L/S, (b) 60-nm-hp holes, (c) 200-nm-hp L/S, (d) 200-nm-hp holes.

#### IV. RESULTS

To obtain a contrast image of the mask, the CCD camera signal was measured at two positions, namely, on the surface of the Mo/Si multilayer and on the surface of the absorber layer, with a ratio of 39. The reflectivity contrast was found to be as high as 0.95. The reflectivity of the absorber layer was estimated to

be 1.5%, assuming the reflectivity of the Mo/Si multilayer to be about 60%. Since the reflectivity of the absorber layer was higher than the calculated value ( $< 0.1\%$ ), the thickness and/or the absorption coefficient of that layer must be different from the values used in the calculation.

Figure 6 shows images obtained with the CSM of the 200-nm-hp L/S pattern in Fig. 5(c): (a) CCD image, (b) reconstructed image, (c) magnified image of (b), and (d) profile at the center of the reconstructed pattern. The shadowing effects of the absorber pattern are negligible because the incident light was parallel to the L/S pattern. The exposure time was limited to 12 minutes so that the CCD

signal would not be saturated with zero-order light. Figure 6(a) is the diffraction intensity recorded by the CCD camera. The center signal is zero-order light, and up to 4 diffraction orders were recorded. The aura around the zero order is due to the Fraunhofer diffraction of the pinhole. The signal counts for the zero, 1st, 2nd, 3rd, and 4th diffraction orders were 44300, 17955, 915, 1803, and 527, respectively.

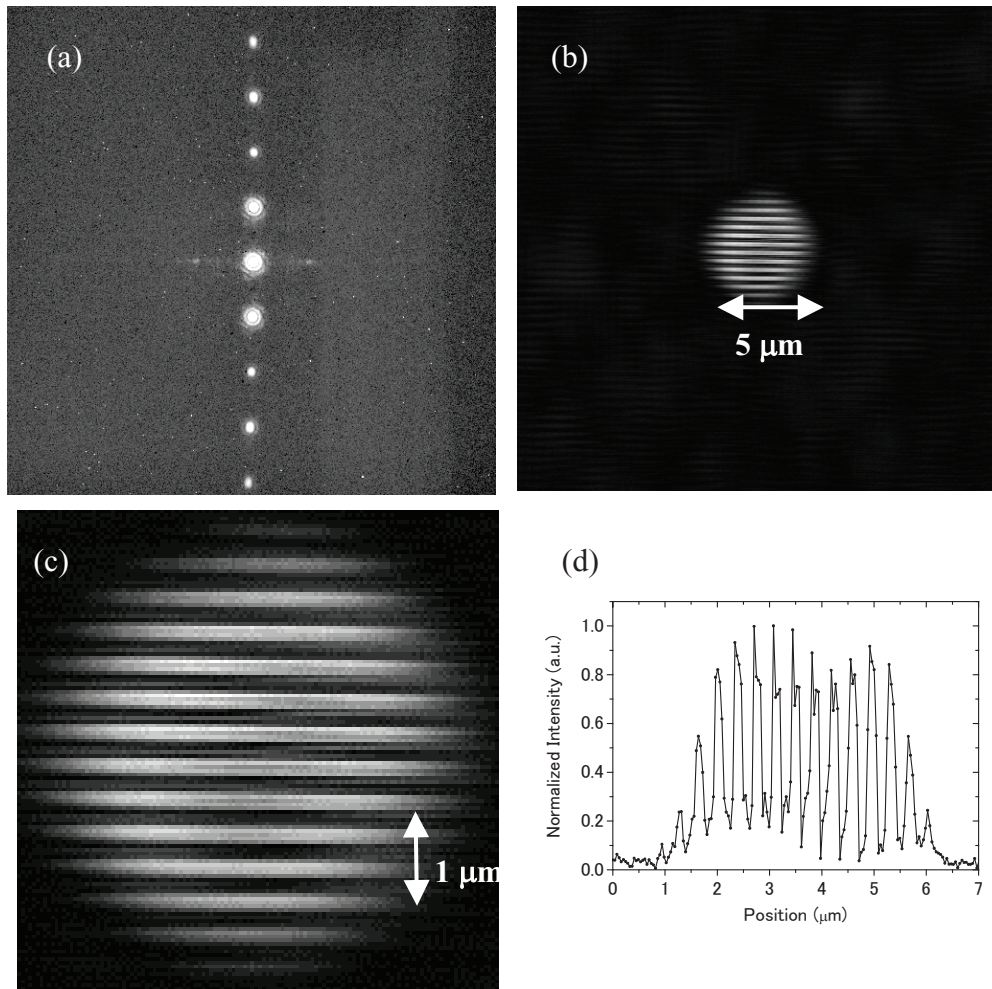


Figure 6. CSM results for 200-nm-hp L/S pattern: (a) CCD image, (b) reconstructed image obtained with HIO algorithm, (c) magnified image of (b), and (d) profile of center of (c).

The CD of the absorber thickness was found to be  $224.2 \pm 2.6$  nm by fitting the peak diffraction intensities to the Fraunhofer diffraction distribution. On the other hand, a one-minute exposure yielded a CD of  $224.8 \pm 3.7$  nm. Since these values are virtually the same, we can conclude that a one-minute exposure is sufficient for estimating the CD. The exposure time could be further reduced by increasing the field of view and by developing a peak detection algorithm. The CD obtained with the SEM was 199

nm, which is smaller than that obtained with the CSM. The SEM detects secondary electrons at the surface of the absorber, and the CSM detects the distribution of the reflectance. Thus, the CD for absorber patterns obtained with the SEM is smaller because the patterns have sloping edges. The dependence of CD on absorber shape will be investigated in the future.

In reconstructing a diffraction image, the signal-to-noise (S/N) ratio is improved by resampling the CCD data to reduce the size of the pixel array

from the original 2048×2048 pixels to 512×512 pixels, where the estimated oversampling ratio<sup>7</sup> is 16. A threshold is also put on the CCD signal to further reduce the noise. The images in Fig. 6(b-c) are reconstructions obtained with 200 iterations of the HIO algorithm. They correlate well to the SEM image in Fig. 5(c). For the reconstruction, the phase in real space was not constrained to be real and positive because the target of the CSM contained a phase defect. In addition, the absorber pattern produces a phase shift corresponding to its thickness. The constraint used in reconstruction was the size of the support area (that is, the illuminated area). The support area was optimized so as to reduce the error signal in real space (mask image) in the unilluminated area. A loose support constraint was initially applied, but the bright image of the 5- $\mu\text{m}$  field moved around in the support area as the iteration proceeded. For optimization, a tight support size was chosen, with a step-by-step increase in the support size to reduce the error. The CD of the reconstructed image profile is about 219 nm, which is

about the same as the fitting results for the diffraction peaks.

Figures 7 and 8 show a 100-nm-hp L/S pattern and a 400-nm-hp hole pattern, respectively, taken with the CSM using exposure times of 8 and 10 minutes. Estimation of the CD requires not only zero- and 1st-order diffraction images but also 2nd-order ones. At present, the CSM cannot record 2nd-order diffraction for patterns with a half pitch of less than 100 nm because of the limited NA. However, 1st-order diffraction was clearly recorded for half pitches from 60 nm to 90 nm. Thus, the pattern with the smallest hp (60 nm) fabricated in our laboratory exhibited a periodic structure when observed with EUV light. In Fig. 7, the reconstruction for the 100-nm-hp L/S pattern is very good. The CD obtained from the SEM image is 95 nm; that from the CSM image is  $120.7 \pm 2.1$  nm; and that from the reconstructed image profile is 119 nm. The CD from the CSM is larger than that from the SEM.

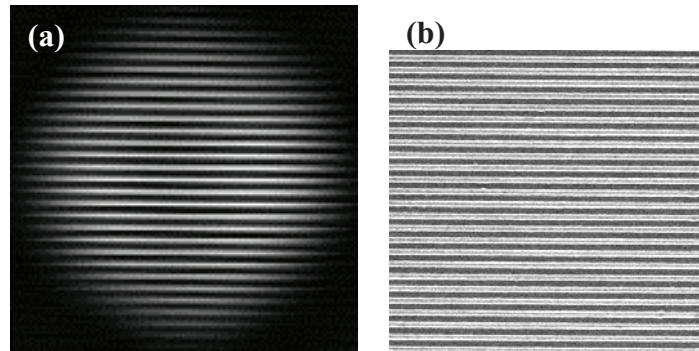


Figure 7. 100-nm-hp L/S pattern: (a) reconstructed image obtained with CSM and (b) SEM image.

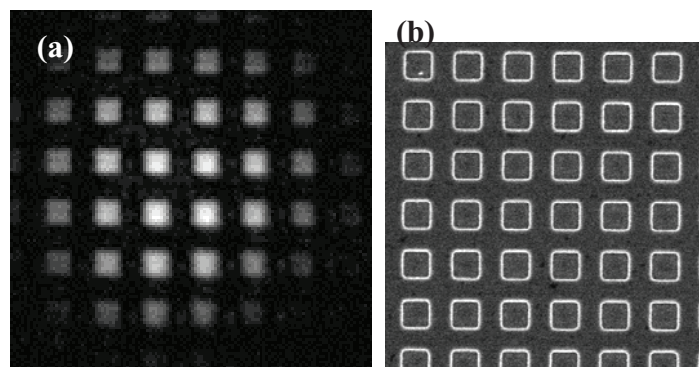


Figure 8. 400-nm-hp hole pattern: (a) reconstructed image obtained with CSM and (b) SEM image.

For the hole pattern in Fig. 8, the reconstructed image corresponds to the SEM image. However, there is a reconstruction error in the absorber region, possibly due to the low reflectivity of the EUV mask.

The count for the zero-order signal was about 3,000, which is only 1/10 of that for the L/S pattern. The L/S and hole patterns were fabricated on the same substrate, but the absorber layer was not completely etched off the holes, even though the dry etching

process was identical. The etching conditions for the

absorber layer need to be optimized.

## V. CONCLUSION

A CSM has been developed for the actinic inspection of EUV lithography masks, and it has been installed at the NewSUBARU synchrotron facility. To evaluate its performance, EUV masks containing L/S and hole patterns with half pitches ranging from 50 nm to 500 nm were fabricated, and the CSM was used to image them. EUV mask patterns with half pitches down to 100 nm were successfully reconstructed. For L/S patterns, the image shapes were well reconstructed and matched those in the SEM images. The actinic CD of an L/S pattern was estimated from a one-minute exposure with the CSM, and was found to be only 25 nm wider than the CD obtained with a SEM. Our results demonstrate that the CSM can be used to image EUV masks and obtain the actinic CD. Thus, the CSM is a practical tool for inspecting EUV masks.

In the near future, we will develop a tabletop high-order harmonic generation (HHG) laser EUV source<sup>11</sup> for the practical inspection of EUV masks. The power will be 1000 times greater than that of our present source, which wastes most of the light in achieving high spatial coherence. The target defect detection sensitivity of this actinic inspection tool is less than 20 nm for the 22-nm node, which translates into a feature size of 5 nm on a wafer. The target sensitivity for the CD is about 0.1 nm, and the target scanning time for a whole mask is less than 90 minutes.

## Acknowledgement

This work was partially supported under the JST-CREST project “Development of Ultra-Fine Structure Metrology System using Coherent EUV Source.”

## References

1. Semiconductor Industry Association, “International Technology Roadmap for Semiconductors: 2007 Lithography”, Austin, TX, International SEMATECH.
2. T. Terasawa, Y. Tezuka, M. Ito and T. Tomie, SPIE Proc. **5446**, 804 (2004).
3. A. Barty, Y. Liu, E. Gullikson, J. S. Taylor, and O. Wood, SPIE Proc. **5751**, 651 (2005).
4. K. A. Goldberg, P. P. Naulleau, A. Barty, S. B. Rekawa, C. D. Kemp, R. F. Gunion, F. Salmassi, E. M. Gullikson, E. H. Anderson and H. Han, SPIE Proc. **6730**, 67305E (2007).
5. T. Haga, H. Takenaka and M. Fukuda, J. Vac. Sci. Technol. B **18**, 2916 (2000).
6. K. Hamamoto, Y. Tanaka, H. Kawashima, S. Y. Lee, N. Hosokawa, N. Sakaya, M. Hosoya, T. Shoki, T. Watanabe and H. Kinoshita, Jpn. J. Appl. Phys. **44**, 5474 (2005).
7. J. Miao, P. Charalambous, J. Kirz and D. Sayre, Nature **400**, 342 (1999).
8. J. Miao, Y. Nishino, Y. Kohmura, B. Johnson, C. Song, S. H. Risbud and T. Ishikawa, Phys. Rev. Lett. **95**, 085503 (2005).
9. J. R. Fienup, Appl. Opt. **21**, 2758 (1982).
10. T. Watanabe, T. Haga, M. Niibe and Hiroo Kinoshita, J. Synchrotron Rad. **5**, 1149 (1998).
11. E. J. Takahashi, Y. Nabekawa and K. Midorikawa, Appl. Phys. Lett. **84**, 4 (2004).

# Imaging Performance Improvement of an Extreme Ultraviolet Microscope

Kei Takase, Yoshito Kamaji, Naoki Sakagami, Takafumi Iguchi, Masaki Tada, Yuya Yamaguchi, Yasuyuki Fukushima, Tetsuo Harada, Takeo Watanabe, and Hiroo Kinoshita  
Laboratory of Science and Technology for Industry, University of Hyogo  
1-1-2 Kouto, Kamigori, Ako-gun, Hyogo 678-1205, Japan

The extreme ultraviolet microscope (EUVM) has been developed for an actinic mask inspection of a EUV finished mask and a EUV blank mask. Using this microscope, amplitude defects on a finished mask and phase defects on a glass substrate are observed. However, it has a problem of low contrast, which originates from 1) thermal noise of a charge coupled device (CCD) camera, 2) wave aberrations of an optical component, and 3) a nonuniform illumination intensity. To resolve these issues, EUVM was improved. 1) To reduce a thermal noise, a cooled CCD camera is installed. 2) To remove wave aberrations of a back-end turning mirror, a Mo/Si multilayer-coated thick glass substrate with a high surface accuracy is employed instead of a Si wafer substrate. Furthermore, in situ alignment was carried out to remove wavefront aberrations for a Schwarzschild imaging optics. In addition, 3) by installing a scanning system on the front-end turning mirror, a highly uniform illumination intensity was achieved. As a result, images of less than 100 nm without astigmatism were obtained.

## 1. Introduction

In Accordance with the ITRS roadmap, extreme ultraviolet lithography (EUVL) is expected to be introduced into the high-volume manufacturing process from the 22-nm half-pitch node from 2013.<sup>1)</sup> The fabrication of a defect-free mask is the first issue of EUVL technology.<sup>2)</sup> There are two types of defects on EUVL masks. One is an amplitude defect and the other is a phase defect.<sup>3-7)</sup> An amplitude defect originates from either a particle on the surface of the multilayer or a flaw in the multilayer.<sup>8,9)</sup> On the other hand, a phase defect is produced when the multilayer is deposited over either a bump or a pit on the substrate. Since the intensity of reflected light decreases owing to a phase shift, the projection image of the mask area with the phase defect is affected.

There are two techniques of detecting a small defect on an EUVL mask: using deep ultraviolet (DUV) light<sup>10)</sup> and using EUV light at the exposure wavelength.<sup>11-19)</sup> Mask defect inspection using DUV light is a conventional method that is used in optical lithography. However, this inspection has a difficulty in detecting a phase defect inside the Mo/Si multilayer of an EUVL mask because the DUV light is reflected on the surface of a mask. Thus, the at wavelength mask inspection method is necessary for phase defect inspection of an EUV mask. Therefore, we constructed an extreme ultraviolet microscope (EUVM) system.<sup>3-5,20)</sup> Figure 1 shows the configuration of

the actinic EUVM installed at the BL-3 beamline of the NewSUBARU synchrotron radiation (SR) facility. It consists of Schwarzschild optics (NA, 0.3; magnification, 30x) as the illumination and imaging optics, an X-Y-Z sample stage, an X-ray zooming tube connected to a CCD camera, and an image processing computer. It is installed in a vacuum chamber (pressure,  $1 \times 10^{-5}$  Pa) on a vibration isolation table. Figure 2 shows the mechanism of phase defect inspection with EUVM. When the multilayer fulfills the Bragg condition, the EUV light that penetrates into the multilayer is normally reflected. However, if there is a defect pattern on a substrate under the multilayer, the Bragg condition is not satisfied in the multilayer, the light on the defect could not reflect in the right direction to Schwarzschild optics and makes no imaged on the X-ray zooming tube. Thus, an image of a phase defect is observed by a EUVM. EUVM can image phase defects directly, even on a multilayer with a flat surface.

We have observed the finished mask with the absorber pattern and the mask blanks with programmed phase defects to identify the critical dimensions of phase defects on mask blanks.<sup>7)</sup> However, there were nonuniform intensity distribution and wave aberrations. In this paper, image quality improvement technologies are discussed.

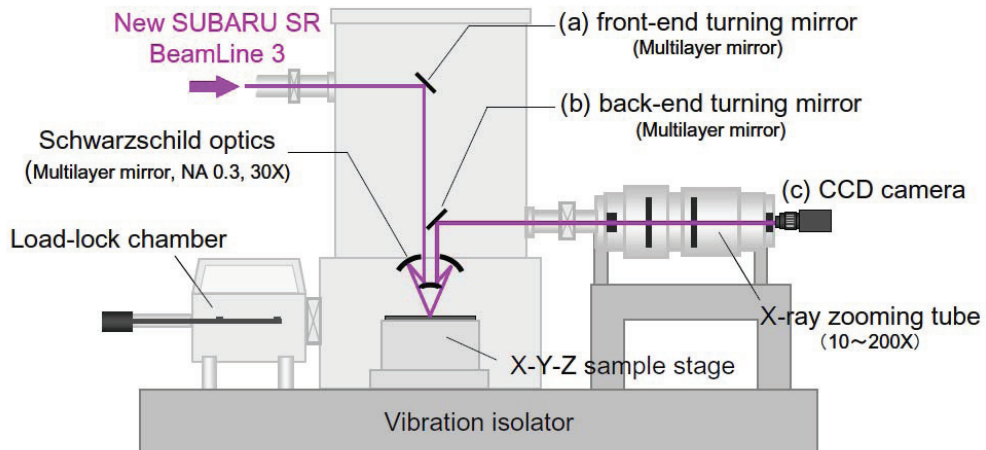


Fig. 1 Setup configuration of the EUVM system. (a) front-end turning mirror (b) back-end turning mirror (c) CCD camera.

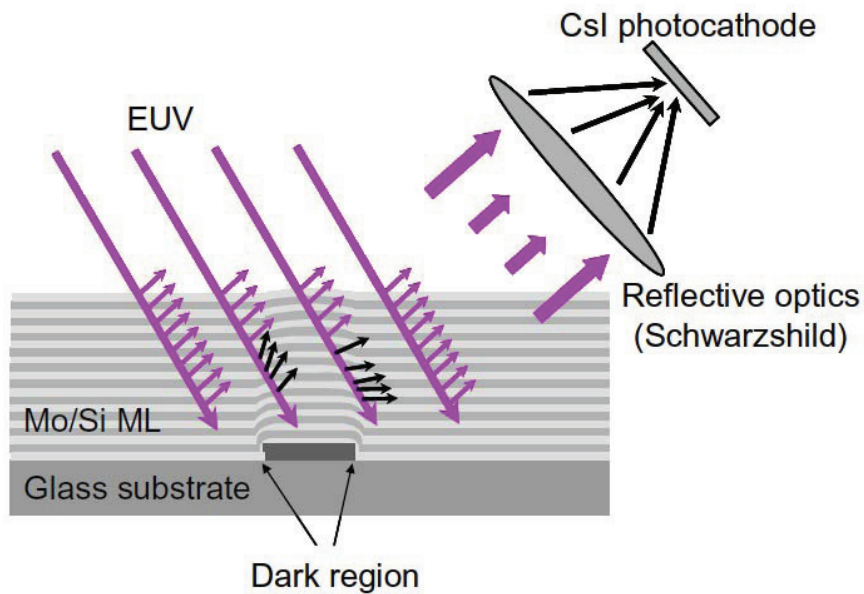


Fig. 2 Mechanism of phase defect inspection.

## 2. Issue of Imaging Quality

Figure 3 shows an image of a 300-nm-half-pitch (hp) elbow pattern observed using EUVM in our previous work<sup>21)</sup>. Since the image includes remarkable wavefront aberrations, the resolution in the horizontal direction and that in the vertical direction are different. These aberrations resulted from the surface

flatness of the substrate of the back-end turning mirror and the wavefront error of the Schwarzschild optics. Furthermore, this image includes nonuniform intensity, which reduces the resolution of the imaging. This nonuniformity also resulted from the surface figure error of the front-end mirror.

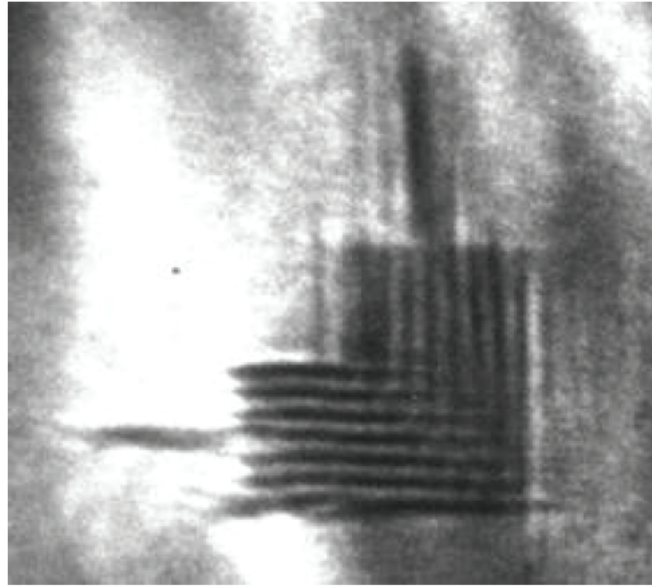


Fig. 3 EUVM image of 300-nm-hp elbow pattern in our previous work (magnification: 1800x).

Figure 4 shows the surface flatness of the Si wafer substrate of the back-end turning mirror. As shown in Fig. 4, the surface figure of the back-end turning mirror was about 166 nm (rms). To reduce

wave aberrations, a lower-figure-error substrate should be employed. In addition, in situ alignment of Schwarzschild optics is required to reduce wavefront aberrations.

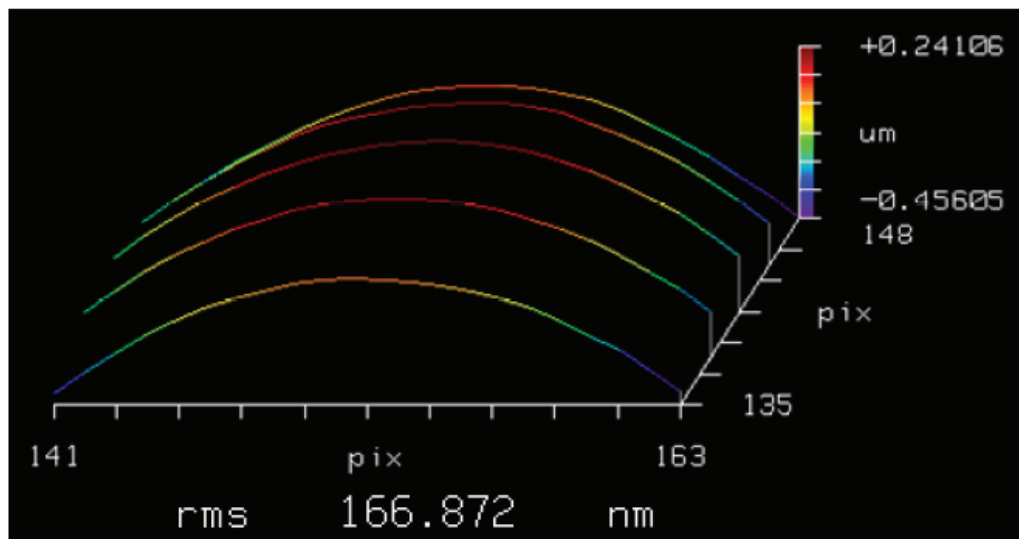


Fig. 4 The surface flatness of Si wafer substrate of back-end turning mirror was about 166 nm (rms).

Figures 5(a) and 5(b) show images of the 300-nm-half pitch (hp) pattern taken using EUVM at total magnifications of (a) 1800x and (b) 6000x, respectively. The noise considered to be thermal

noise of CCD camera is observed at the magnification of 6000x. To reduce the thermal noise of CCD camera, a cooling CCD camera is effective.

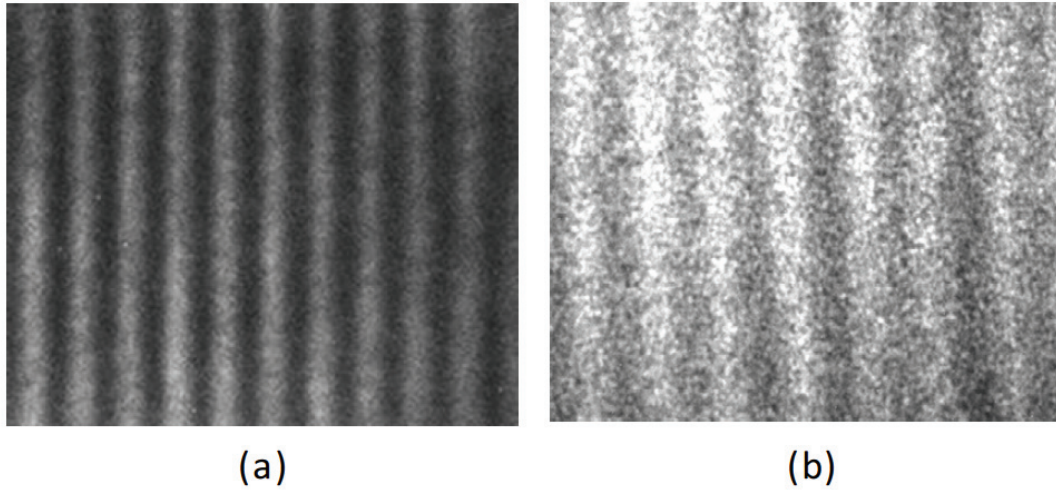


Fig. 5 EUVM images of 300-nm-hp pattern taken at total magnifications of (a) 1800x and (b) 6000x.

### 3. Imaging Quality Improvement

#### 3.1 Thermal noise reduction utilizing cooling CCD camera

The conventional CCD camera was replaced with a cooling CCD to increase a high S/N ratio of the EUVM images by reducing thermal noise. Table I shows the performance of the CCD camera and cooling CCD camera. Figure 6 shows the background images taken by the conventional (a) and cooling (b) CCD cameras without the optical input observed by EUVM and the intensity distribution of the image. The cooling CCD temperature was set at a minimum cooling temperature of -27 °C. The thermal noise of the cooling CCD camera disappeared, as shown Fig. 6(b), and the camera enabled the acquisition of uniform-background images. Therefore, the cooling CCD camera also enabled the acquisition of EUVM

images of high contrast at a maximum magnification of 200x. Figures 7(a) and 7(b) show the EUVM images of a 150-nm-hp pattern at a magnification of 6000x before and after the updating the CCD camera. The contrast of the 150-nm-hp pattern was increased from 0.22 to 0.38 when using a cooling CCD camera. The contrast can be calculated using the following equation:

$$Contrast = \frac{I_{max} - I_{min}}{I_{max} + I_{min}},$$

where  $I_{max}$  and  $I_{min}$  are the average maximum value and the average minimum value of the EUV intensity distributions of the line and space pattern, respectively.

Table I . The performance of a CCD camera and a cooling CCD camera.

	CCD camera	Cooling CCD camera
Imaging area ( $\mu\text{m}^2$ )	$9.0 \times 6.7$	$14.8 \times 10.0$
Pixels	$1392 \times 1040$	$2184 \times 1472$
Pixel size ( $\mu\text{m}$ )	$6.45 \times 6.45$	$6.8 \times 6.8$
Minimum cooling temp. (°C)	—	-27

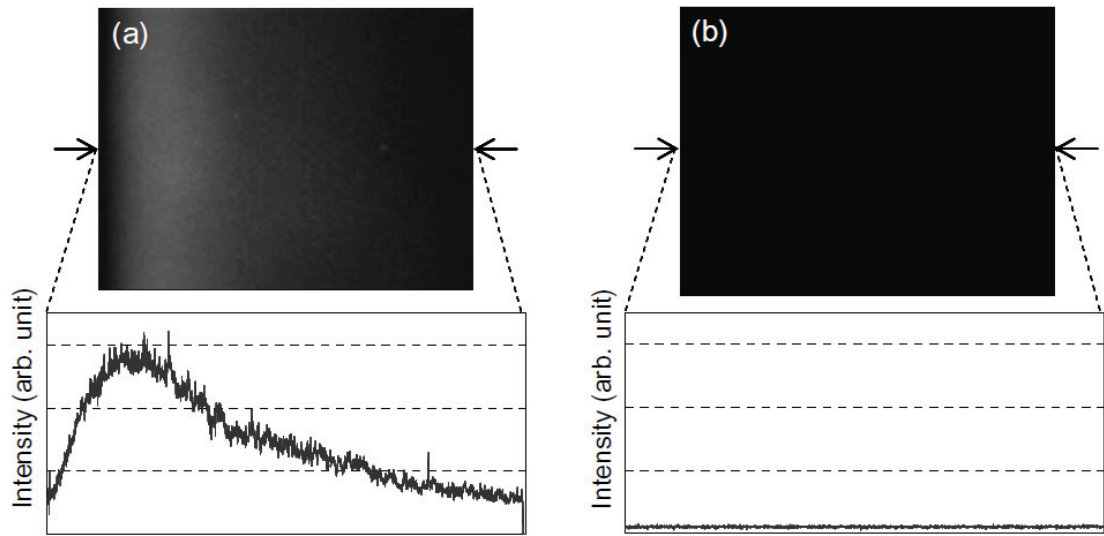


Fig. 6 EUVM background images without optical input and the intensity profiles of each image. (a) taken with a CCD camera, (b) taken with a cooling CCD camera.

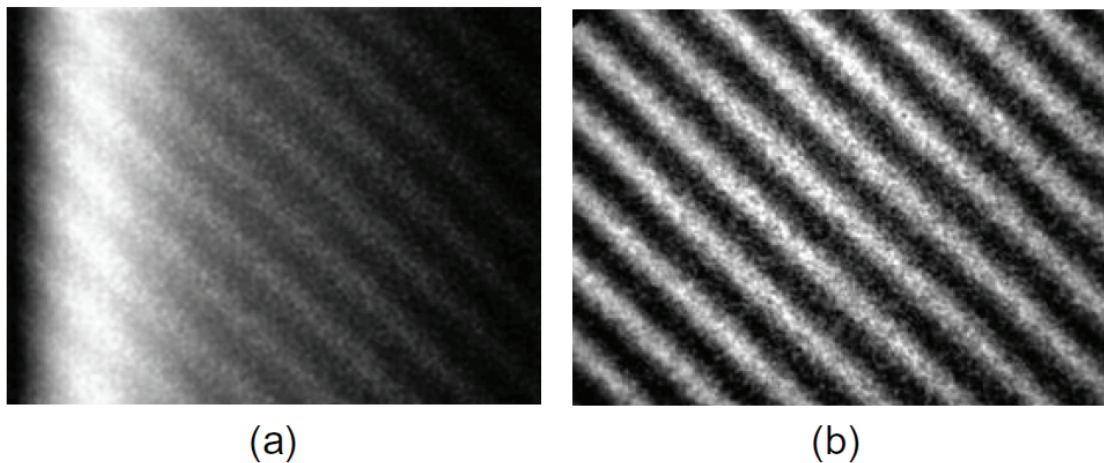


Fig. 7 EUVM images of 150 nm Line and Space (L/S) pattern (a) taken with a CCD camera, (b) taken with a cooling CCD camera (magnification: 6000x).

### 3.2 Reduction of wave aberration to improve optical components

To reduce the wavefront aberration, in general, a smooth and flat mirror surface and highly accurate alignment of the optical system are necessary for the imaging. In the EUVM system, a Mo/Si multilayer coated on the Si wafer was employed as the back-end turning mirror. As shown in Fig. 4, this mirror has a surface figure error of 166 nm (rms), it causes a large wavefront aberration and defocusing. Furthermore, in the alignment of an optical system (carried out by wavefront measurement using a laser interferometer) in the atmosphere, alignment accuracy changes after a period time. It causes imaging aberrations.

The Mo/Si multilayer coated on a thick glass substrate with a smooth surface was employed as a back-end turning mirror in the EUVM system, as indicated by (b) in Fig. 1 instead of the Mo/Si multilayer coated on a Si wafer substrate to improve wave aberrations. The wavefront error of the updated mirror was measured using a Fizeau interferometer (ZYGO GPI) and has a flatness of 3.7 nm (rms), as shown Fig. 8. In addition, we also carried out in situ alignment of the Schwarzschild imaging optics to reduce wave aberrations. Namely, an X-Y-Z-axis alignment mechanical system for each mirror of the imaging optics, which enables movement in vacuum is installed in the optical housing.

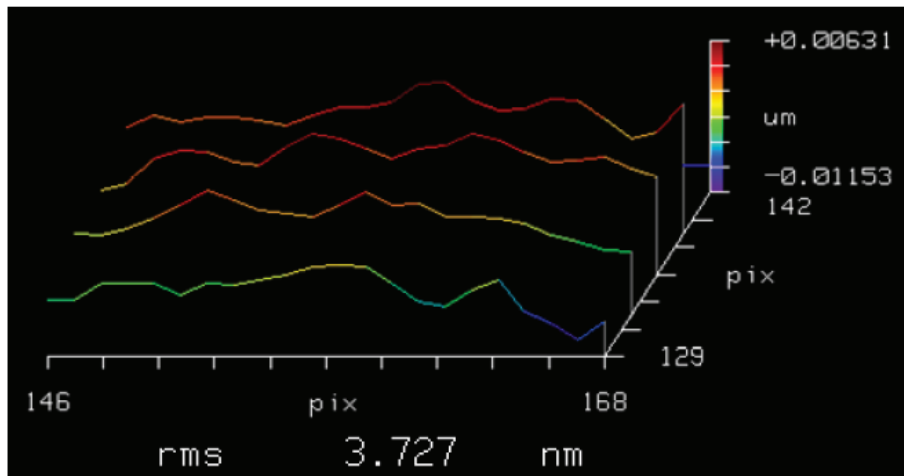


Fig. 8 The surface flatness of thick glass substrate of back-end turning mirror was about 3.7 nm (rms).

Figures 9(a) and 9(b) show the observed images of a 480-nm-hp elbow pattern before and after reducing wavefront aberrations, respectively. As a

result of changing a thick mirror and introducing in situ alignment, the wavefront aberrations and resolution were improved.

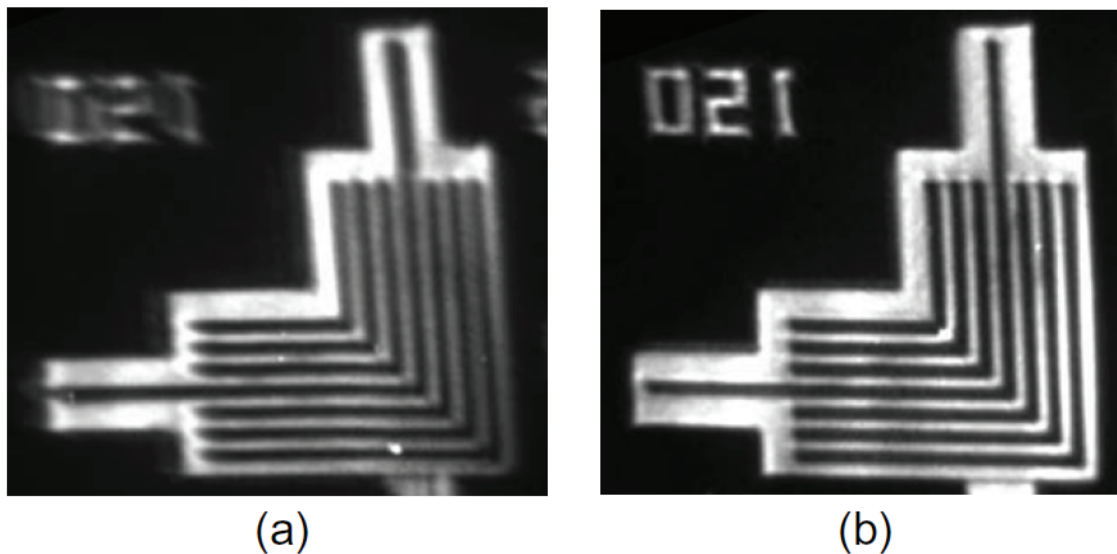


Fig. 9 EUVM images of 480-nm-hp elbow pattern. (a) before upgrading of imaging optics. (b) after upgrading of imaging optics (magnification: 600x).

**3.3 Achievement of uniform illumination intensity**  
It was difficult to recognize the existence of phase defects from the intensity distribution on an EUVM image recorded using the static illumination as shown Fig. 10(a), because the signal of the defects is hidden by the noise that causes the nonuniform illumination intensity. This nonuniform illumination intensity distribution seems to be caused by the figure error of front-end mirrors. Then, in order to average a nonuniform illumination intensity distribution, the

front-end turning mirror [as indicated by (a) in Fig. 1] was scanned. A piezo actuator was employed for scanning a mirror.

A uniform illumination was successfully obtained after the front-end-turning-mirror scanning. Figures 10(a) and 10(b) show the EUVM images of a programmed bump defect of 160 nm width recorded by static illumination and scanning illumination. Figures 10(c) and 10(d) show the illumination intensity distributions along the imaginary lines

between two arrows in Fig. 10(a) and Fig. 10(b), respectively. By reducing noise intensity by a front-end-turning-mirror scanning method, the phase

defect signal was recognized clearly, as shown in Fig. 10(d).

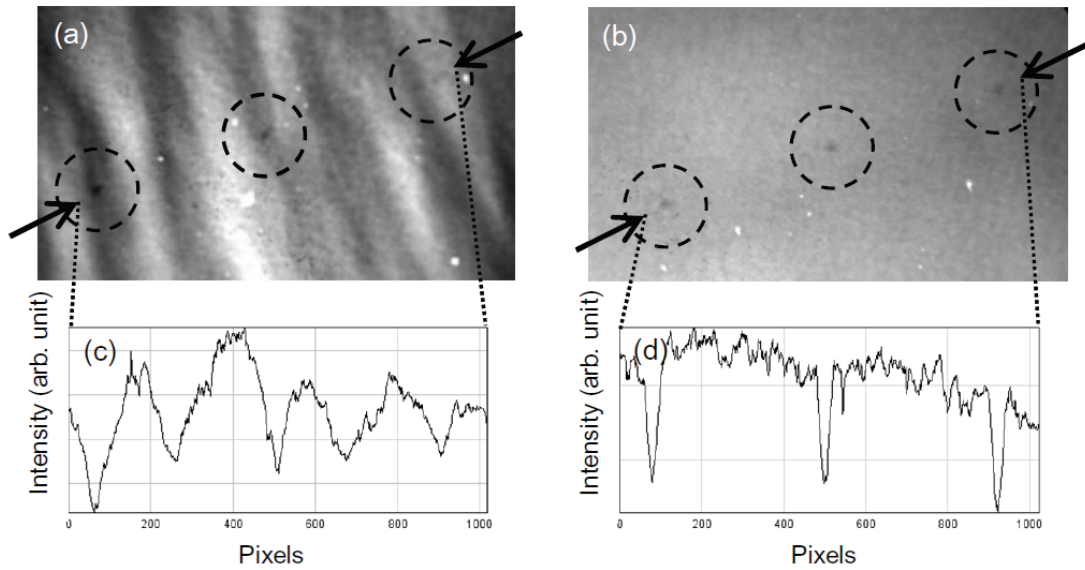


Fig. 10 EUVM images of programmed bump defect width of 160 nm size recorded with (a) static illumination and (b) scanning illumination. (magnification: 600x) (c) and (d) show the illumination intensity distributions along the imaginary lines between two arrows in (a) and (b) images.

#### 4. Imaging performance of EUVM

After the improvement as described in § 3, the resolution and image contrast of line and space absorber patterns were evaluated. Figure 11 shows the images of 150-, 130-, 120-, 110-, and 100-nm-hp patterns obtained by EUVM. Then, the contrast as shown Fig. 11, was calculated from the illumination

intensity distribution of the EUVM images. Although the resolution and contrast of the EUVM images were improved, the resolution and contrast were still not sufficient for the 22-nm-node requirement. Further studies are required for the improvements of resolution and contrast.

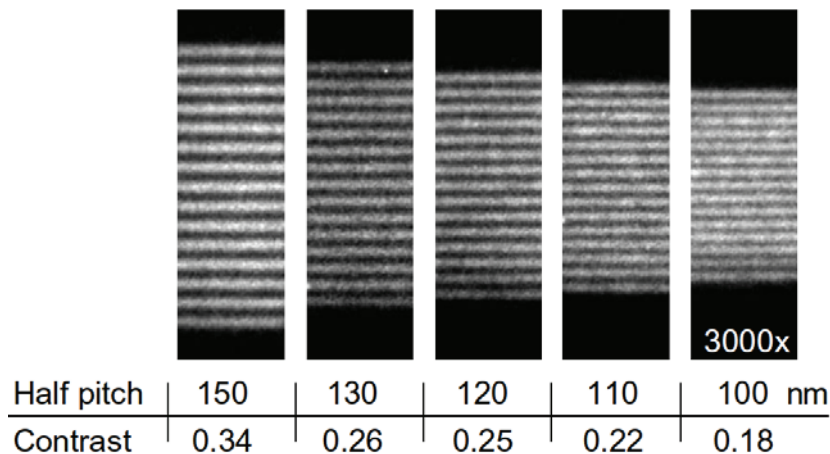


Fig. 11 EUVM images of 150, 130, 120, 110 and, 100-nm-hp patterns and there contrast values (magnification: 3000x).

## 5. Conclusions

EUVM images of high contrast at a high magnification were obtained using the cooling CCD camera. Wavefront aberrations were reduced and resolution was improved by employing a Mo/Si multiplayer-coated thick glass substrate of high surface accuracy on a back-end turning mirror and

good-alignment of Schwarzschild imaging optics. Utilizing a scanning system on a front-end turning mirror, the phase defect was recognized clearly in EUVM owing to reduction of background intensity noise. By these improvements EUVM image quality was improved.

## References

- 1) International Technology Roadmap for Semiconductors (2004) : Lithography.
- 2) H. Kinoshita, K. Kurihara, Y. Ishii, and Y. Torii: *J. Vac. Sci. Technol*, **B7**(1989) 1648.
- 3) K. Hamamoto, Y. Tanaka, S. Y. Lee, N. Hosokawa, N. Sakaya, M. Hosoya, T. Shoki, T. Watanabe, and H. Kinoshita: *J. Vac. Sci. Technol*, **B23** (2005) 2852.
- 4) K. Hamamoto, Y. Tanaka, H. Kawashima, S. Y. Lee, N. Hosokawa, N. Sakaya, M. Hosoya, T. Shoki, T. Watanabe, and H. Kinoshita: *Jpn. J. Appl. Phys.* **44** (2005) 5474.
- 5) K. Hamamoto, Y. Tanaka, T. Yoshizumi, N. Hosokawa, N. Sakaya, M. Hosoya, T. Shoki, T. Watanabe, and H. Kinoshita: *Jpn. J. Appl. Phys.* **45** (2006) 5378.
- 6) K. A. Goldberg , A. Barty, Y. Liu, Y. Tezuka, T. Terasawa, J. S. Taylor, H. Han, and O. R. Wood: *J. Vac. Sci. Technol*, **B24** (2006) 2824.
- 7) Y. Kamaji, K. Takase, T. Yoshizumi, T. Sugiyama, T. Uno, T. Watanabe, and H. Kinoshita: *Jpn. J. Appl. Phys.* **48** (2009) 06FA07.
- 8) T. Liang, A. Stivers, R. Livengood, P.-Y. Yan, G. Zhang, and F.-C: Lo: *J.Vac. Sci. Technol*, **B18** (2000) 3216.
- 9) E. M. Gullikson, C. Cerjan, D. G. Stearns, P. B. Mirkarimi, and D. W. Sweeney: *J. Vac. Sci. Technol*, **B20** (2002) 81.
- 10) Lasertec DUV Mask Review Station MRS248 [<http://www.lasertec.co.jp/products/mrs248.html>].
- 11) T. Haga, H. Takenaka, and M. Fukuda: *J. Vac. Sci. Technol*, **B18** (2000) 2916.
- 12) T. Haga, H. Kinoshita, K. Hamamoto, S. Takada, N. Kazui, S. Kakunai, H. Tsubakino, and T. Watanabe, *Jpn: J. Appl. Phys.* **42** (2003) 3771.
- 13) H. Kinoshita, T. Haga, K. Hamamoto, S. Takada, N. Kazui, S. Kakunai, H. Tsubakino, T. Shoki, M. Endo, and T. Watanabe: *J. Vac. Sci. Technol*, **B22** (2004) 264.
- 14) T. Terasawa, Y. Tezuka, M. Ito, and T. Tomie: *Proc. SPIE* **5446** (2004) 804.
- 15) Y. Tezuka, M. Ito, T. Terasawa, and T. Tomie: *Proc. SPIE* **5446** (2004) 870.
- 16) A. Barty, Y. Liu, E. Gullikson, J. S. Taylor, and O. Wood: *Proc. SPIE* **5751** (2005) 651.
- 17) Y. Liu, A. Barty, E. Gullikson, J. S. Taylor, J. A. Liddle, and O. Wood: *Proc. SPIE* **5751** (2005) 660.
- 18) K. A. Goldberg, P. P. Naulleau, A. Barty, S. B. Rekawa, C. D. Kemp, R. F. Gunion, F. Salmassi, E. M. Gullikson, E. H. Anderson, and H.-S. Han: *SPIE* **6730** (2007) 67305E.
- 19) T. Terasawa, T. Yamane, T. Tanaka, T. Iwasaki, O. Suga, and T. Tomie: *Jpn. J. Appl. Phys.* **48** (2009) 06FA04.
- 20) Y. Tanaka, T. Watanabe, K. Hamamoto, and H. Kinoshita: *Jpn. J. Appl. Phys.* **45** (2006) 7163.
- 21) M. Osugi, K. Tanaka, N. Sakaya, K. Hamamoto, T. Watanabe, and H. Kinoshita: *Jpn. J. Appl. Phys.* **47** (2008) 4872.

# Development of the Extreme Ultraviolet Interference Lithography System

\*Yasuyuki Fukushima, Naoki Sakagami, Teruhiko Kimura,  
Yoshito Kamaji, Takafumi Iguchi, Yuuya Yamaguchi, Masaki Tada,  
Tetsuo Harada, Takeo Watanabe, and Hiroo Kinoshita

*Laboratory of Advanced Science and Technology for Industry, University of Hyogo,  
3-1-2 Koto, Kamigori, Hyogo 678-1205, Japan*

e-mail: yasuyuki@lasti.u-hyogo.ac.jp

Extreme ultraviolet interference lithography was carried out at the long undulator beamline in NewSUBARU. It was confirmed that the spatial coherence length is 1.1 mm using a 10- $\mu\text{m}$ -wide slit in the Young's double slit experiment. A 25-nm half pitch (hp) resist pattern was successfully replicated by extreme ultraviolet interference lithography (EUV-IL) utilizing a two-window transmission grating pattern of a 50-nm line and space (L/S). For the replication of a 20-nm L/S resist pattern by EUV-IL, we contrived a fabrication process that is suitable for a transmission grating pattern of 40-nm L/S and smaller. Employing a hard-mask process with a silicon dioxide ( $\text{SiO}_2$ ) layer on a tantalum-nitride (TaN) layer in the fabrication of a two-window transmission grating, we successfully achieved five times larger dry-etch selectivity in comparison with a non-hard-mask process. As a result, we confirmed the ability this process to apply to a 40-nm hp grating.

## 1. Introduction

Extreme ultraviolet lithography (EUVL)<sup>1)</sup> is the most promising technology for a 22-nm half-pitch (hp) and it will be required for high-volume-manufacturing lithographic technology by the year 2013.<sup>2)</sup> Resist materials and process technologies are two of the three top issues. In addition, according to the ITRS roadmap, EUVL is strongly predicted to be expanded to the 20-nm node by the year 2017 and to the 11-nm node by the year 2022. For the 20-nm node and the 11 nm-node, the requirements of line width roughness (LWR) are 0.8 nm ( $3\sigma$ ) and 0.6 nm ( $3\sigma$ ), respectively. Because the required size of LWR is smaller than the molecular size of a resist, a satisfying the LWR criterion is not easy. Thus,

because the development of resist material should be started earlier than the development of the EUV exposure alpha tool, extreme ultraviolet interference lithography (EUV-IL)<sup>3-12)</sup> should be recognized as an important part in the evaluation of resist materials at 20-nm and smaller.

The EUVL interference exposure tool was installed at the BL-9 long undulator beamline in the NewSUBARU synchrotron radiation facility. The EUV-IL exposure tool including a two-window transmission grating was installed at the end station of the BL9C beamline. In this report, we focus on the coherence length measurement, exposure result, and fabrication process using a hard-mask process for a silicon dioxide ( $\text{SiO}_2$ ) layer on a transmission grating.

## 2. Beamline Setup for EUV-IL in NewSUBARU

EUV-IL was constructed at the BL9 long undulator (LU) beamline in NewSUBARU. Figure 1 shows the beamline setup of the EUV-IL. An LU source spectrum with the peak at a specific wavelength can be obtained by tuning the gap between the magnets of the undulator.<sup>13)</sup> Because the long undulator in NewSUBARU has a total length of 10.8 m and has 200 periods for high-brilliance radiation, the brilliance of EUV light with the undulator as a source is approximately 50,000 times higher than that with a bending magnet as a source.<sup>14)</sup> To achieve a 20-nm L/S pattern and smaller on a wafer by EUV-IL, a

large spatial coherence length can be increased by enlarging the distance between the pinhole and the transmission grating. Thus, a large spatial coherence length and a low exposure time can be realized simultaneously by increasing the light intensity employing the long undulator. As described in §4, a spatial coherence length of more than 1 mm can be achieved. Figure 2 shows the light spectrum used in this experiment. The EUV light was focused on a pinhole using an optical component. At the pinhole position, the beam is focused to a size of 10  $\mu\text{m}$  in the  $y$ -direction. Because the distance from the pinhole to the resist is maintained at approximately 3.3 m and

the high wavelength range beyond 20 nm is removed by a 0.2- $\mu\text{m}$ -thick zirconium (Zr) filter, the light is

monochromated with a wavelength of 13.4 nm on the resist sample.

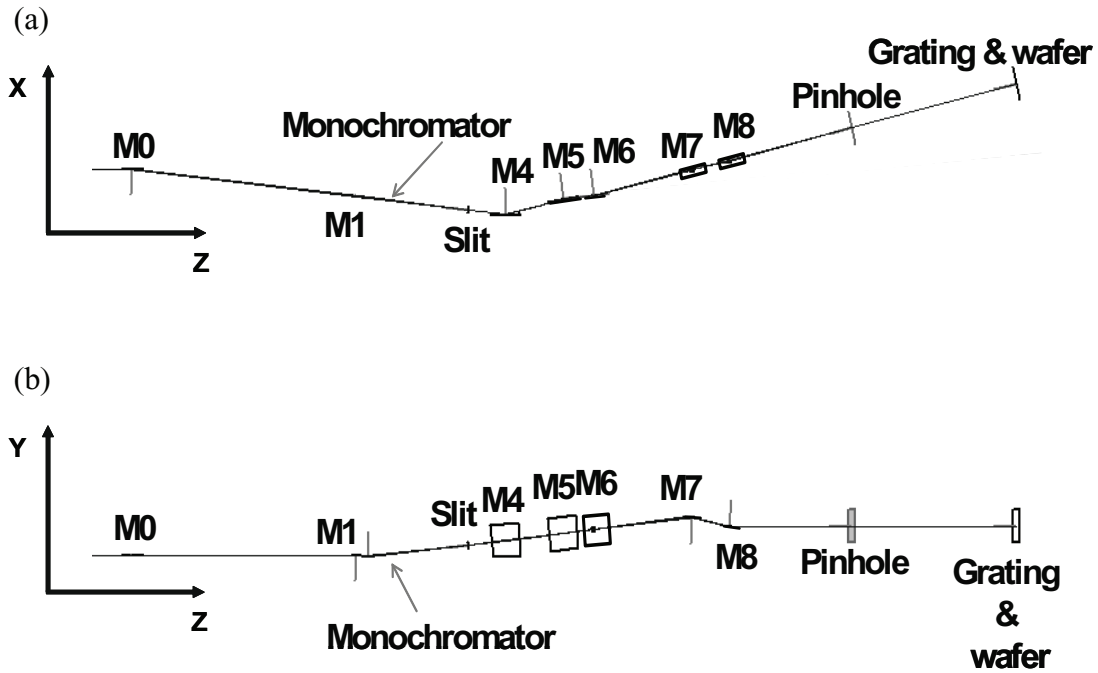


Fig. 1. BL9 beamline setup of EUV-IL: (a) top view and (b) side view.

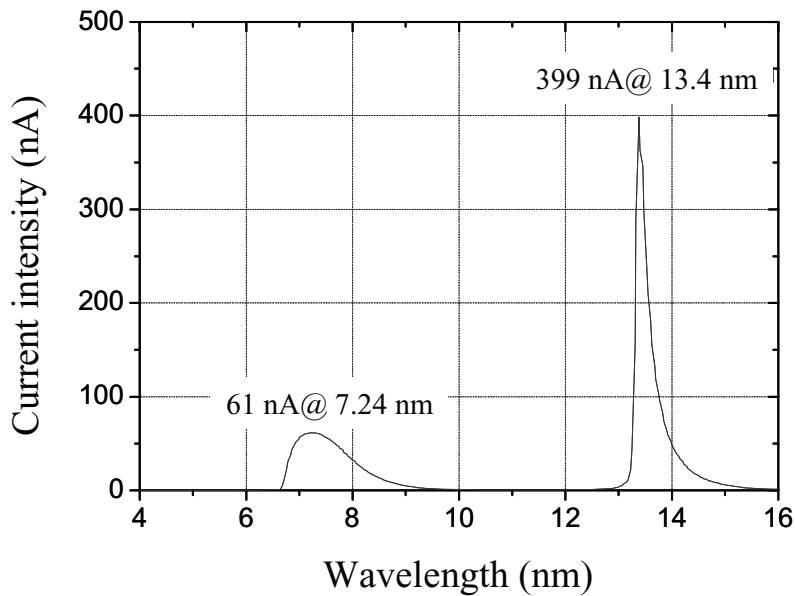


Fig. 2. Spectrum of long undulator at the BL9 beamline used for EUV-IL.

### 3. Principle of EUV

Figure 3 shows the principle of EUV-IL. In the dual beam interference system, double periodic interference fringes are created at a position fitting two phases when the +1st order ray diffracted from one window of the grating interferes with the -1st

order ray diffracted from another window of the grating. The diffraction condition of the grating can be expressed as  $m\lambda = d(\sin \theta_f - \sin \theta_i)$ , where  $m$ ,  $d$ ,  $\theta_f$ , and  $\theta_i$  are the number of the diffraction order, the pitch size of the grating pattern, the angle of transmitted light, and the angle of

incident light, respectively. In addition, the pitch size of interference fringes  $p$  is expressed as  $p = \lambda / (2 \sin \theta)$ , where  $\theta$  is half of the angle between the propagating directions of the two beams of the +1st and -1st diffraction orders. Considering normal incident light, an incident light angle may be expressed as  $\theta_i = 0$ . Then, the pitch size of interference fringes  $p$  is expressed as  $p = d / 2$ . Thus, the half-size of the grating pattern size can be replicated on a wafer. In EUV-IL the distance

between the two windows has to be smaller than the coherence length. In addition, if the grating pitch pattern  $d$  becomes smaller, the diffraction angle  $\theta_f$  of the -1st and +1st diffraction orders becomes larger. If the distance between two windows of a transmission grating is constant, the distance between the grating and the wafer becomes smaller. Thus, a larger coherence length may relax the distance between the grating and the wafer.

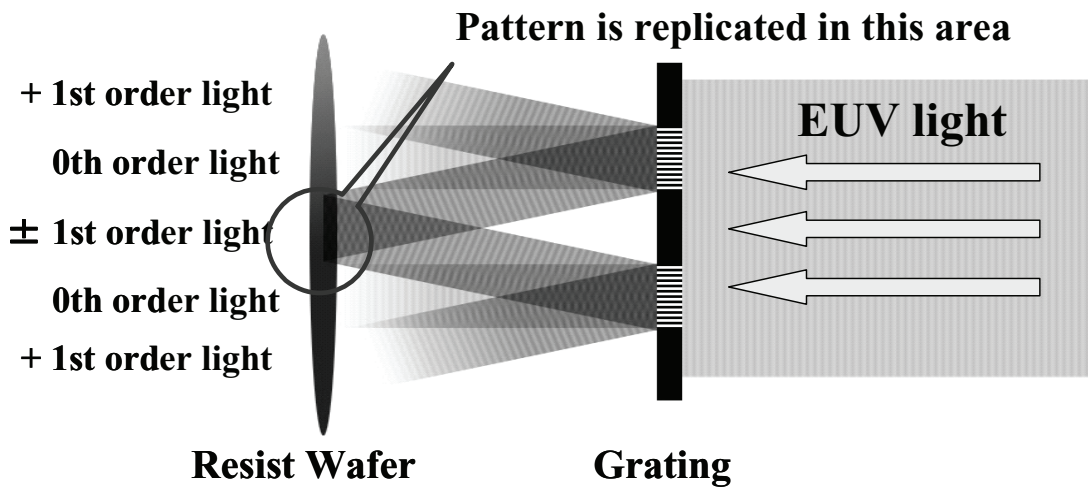


Fig. 3. Principle of EUV interference lithography.

#### 4. Spatial Coherence Measurement

The spatial coherence of the light source can be determined by Young's double slit experiment. Figure 4 shows the experimental setup for the spatial coherence measurement.<sup>15, 16</sup> The distance between the single slit and the double slit was 0.9 m, and the distance between the double slit and the photodiode installed in the exposure chamber was 2.4 m. The light intensity was measured by changing the

photodiode position in the vertical direction, as shown in Fig. 4(b). Two single slits of 3 mm (horizontal)  $\times$  25  $\mu$ m (vertical) in size and 3 mm (h)  $\times$  10  $\mu$ m (v) in size were prepared. The size of each slit in the double slit was 3 mm (h)  $\times$  25  $\mu$ m (v). Four double slits with separations of 40, 160, 320, and 640  $\mu$ m were prepared for Young's double slit experiment.

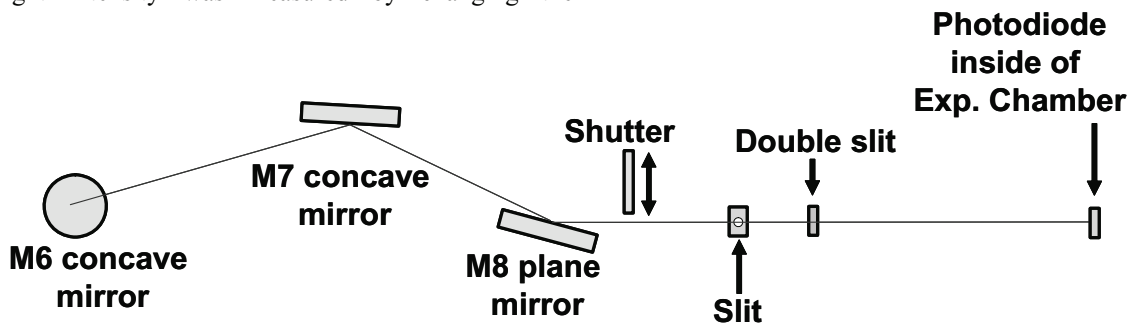


Fig. 4. Experimental setup for spatial coherence measurement.

The spatial coherence was calculated by the following method. The contrast of the spatial coherence is expressed as  $Contrast = \exp(-d_s^2 / 2R_c^2)$ , where  $R_c (= 2 \times l_c)$ ,  $l_c$ , and  $d_s$  are the coherence radius, the spatial coherence length at the double slit position, and the double slit separation, respectively. The spatial coherence length is defined for the condition where  $Contrast = 0.88$ . Furthermore, the measured value of  $Contrast$  is expressed as  $Contrast = (I_{max} - I_{min}) / (I_{max} + I_{min})$ , where  $I_{min}$  and  $I_{max}$  are the minimum photodiode current and the maximum photodiode current, respectively. When the distance between the single slit and the double slit and the distance between the double slit and the photodiode are taken into account, the spatial coherence length ( $L_c$ ) at the grating position is expressed as  $L_c = 2.4 \times l_c / 0.9$ .

Figures 5(a), 5(b), and 5(c) show the results of light intensity measurements using a 25- $\mu\text{m}$  slit with double slit separations of 40, 160, and 320  $\mu\text{m}$ , respectively. In addition, Fig. 5(d) shows the result of light intensity measurements using a 10- $\mu\text{m}$  slit with a double slit separation of 640  $\mu\text{m}$ . In this figure, the vertical axis is the measured current from a photodiode, and the horizontal axis is the distance to the double slit in the  $y$ -direction.  $Contrast$  can be obtained using eq. (5) by substituting the maximum and minimum values obtained from these graphs. Figure 6 shows results. The vertical axis is normalized  $Contrast$ , and the horizontal axis is the double slit separation. Using 25- $\mu\text{m}$  and 10- $\mu\text{m}$  single slits, the spatial coherence lengths ( $l_c$ ) at the double slit position were 204 and 440  $\mu\text{m}$ , respectively. Thus, it was confirmed that spatial coherence ( $L_c$ ) using a 25- $\mu\text{m}$  slit and a 10- $\mu\text{m}$  slit was 544 and 1173  $\mu\text{m}$  at the transmission grating position, respectively. As a result, a large spatial coherence length was achieved for replicating a 20-nm L/S pattern and smaller.

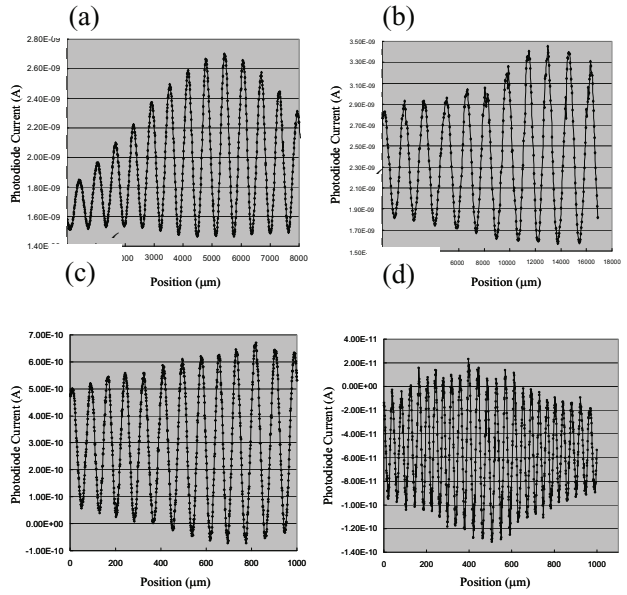


Fig. 5. Examples of light intensity measurement at the grating position: (a) slit width 25  $\mu\text{m}$  and double slit separation 40  $\mu\text{m}$ , (b) slit width 25  $\mu\text{m}$  and double slit separation 160  $\mu\text{m}$ , (c) slit width 25  $\mu\text{m}$  and double slit separation 320  $\mu\text{m}$ , and (d) slit width 10  $\mu\text{m}$  and double slit separation 640  $\mu\text{m}$ .

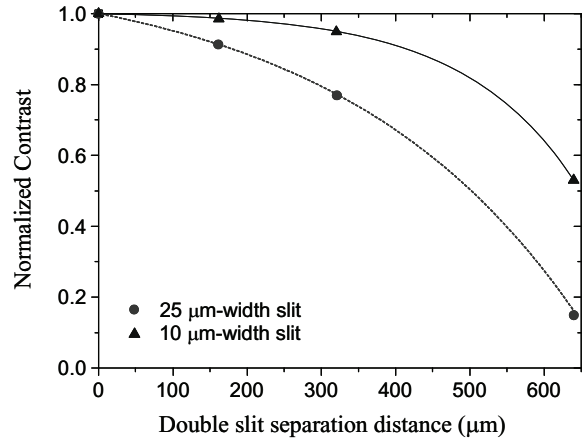


Fig. 6. Results of spatial coherence length measurement.

### 5. Resist Patterning by EUV-IL

25 nm hp resist pattern was replicated by EUV-IL using the 100-nm-pitch transmission grating. A wafer stage and a grating stage were installed in the EUV-IL exposure chamber. The wafer stage consists of  $x$ -,  $y$ -, and  $z$ -stages and a tilt stage. The grating stage consists of  $x$ - and  $y$ - stages and a tilt stage. Using these stages, the light axis was adjusted. A nonchemically amplified resist ZEP520A was spin-coated on a 4-in. wafer. The resist thickness was

50 nm, and the prebake was carried out at 180  $^{\circ}\text{C}$  for 180 s. The exposure conditions were as follows: using a 25- $\mu\text{m}$  (vertical) slit, the distance between the wafer and the transmission grating was 250  $\mu\text{m}$ , the current was 560 nA after transmission grating, and the exposure time was 12 s. Development was carried out at 23  $^{\circ}\text{C}$  for 90 s with o-xylene, and the wafer was rinsed at 23  $^{\circ}\text{C}$  for 30 s with isopropyl alcohol.

Figure 7 shows a photograph of a replicated ZEP520A resist pattern of a 34-nm line and a 16-nm

space (25-nm hp) pattern observed using a critical dimension scanning microscope (CD-SEM; Hitachi S8840). In the near future, various types of

chemically amplified resist will be evaluated. In addition, in future studies, we will approach replicating 20-nm hp resist patterns and smaller.

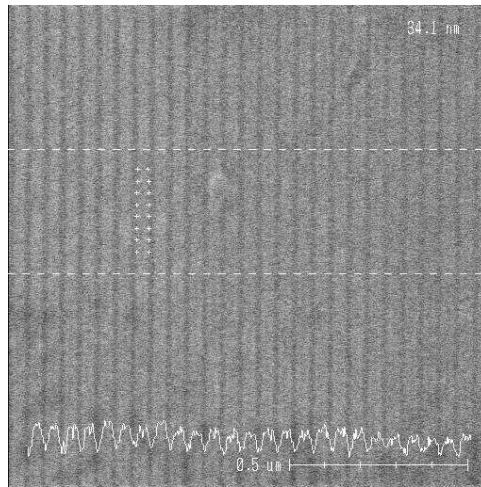


Fig. 7. SEM image of replicated ZEP520A resist pattern of a 25-nm hp.

Using a two-dimensional transmission grating, as shown in Fig. 8(a), with a four-beam diffraction, a dot or hole pattern can be replicated. In this case, for a 50-nm L/S grating pattern, a 35-nm hp dot resist pattern was replicated, as shown in Fig. 8(b). The

resist was ZEP520A. The resist thickness was 50 nm. The resist development and rinse conditions were the same as those used in replicating the L/S resist pattern.

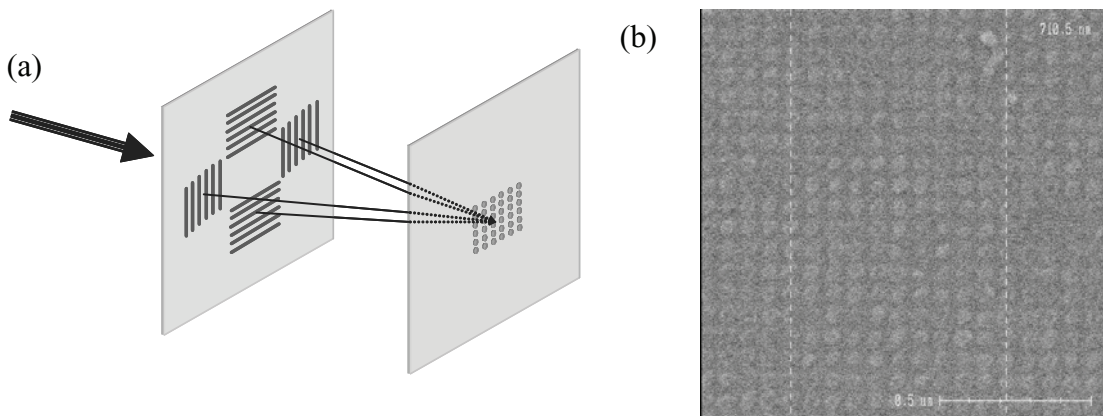


Fig. 8. (a) Configuration of two-dimensional transmission grating and (b) SEM image of replicated ZEP520A resist pattern of 35-nm hp dot resist pattern.

### 6. Transmission Grating Fabrication by Applying a Hard-Mask Process

The fabrication of a transmission grating<sup>17)</sup> is a key technology for EUV-IL. For replicating resist patterns of 20-nm hp and smaller, it is necessary to make a transmission grating of a 40-nm L/S pattern. Figure 9 shows the fabrication of a transmission grating. A 4-in. silicon wafer coated on both sides with a silicon nitride ( $\text{Si}_3\text{N}_4$ ) layer in 300 nm thick was prepared. The transmittance of a 300-nm-thick

$\text{Si}_3\text{N}_4$  layer is 7.4%. For the grating absorber, a TaN layer with 70 nm thick was coated on a  $\text{Si}_3\text{N}_4$  layer, which has a good absorbance of 99.6% for EUV light.<sup>18)</sup> Considering the dry-etch selectivity between a resist and TaN, to fabricate 30-nm and 40-nm L/S TaN patterns with 70 nm thick, the resist should be 200 nm thick. Therefore, it is impossible to make 30- and 40-nm L/S resist patterns with 200 nm thick, because the resist pattern collapses. On the other hand, if a 20-nm-thick silicon dioxide ( $\text{SiO}_2$ ) layer is



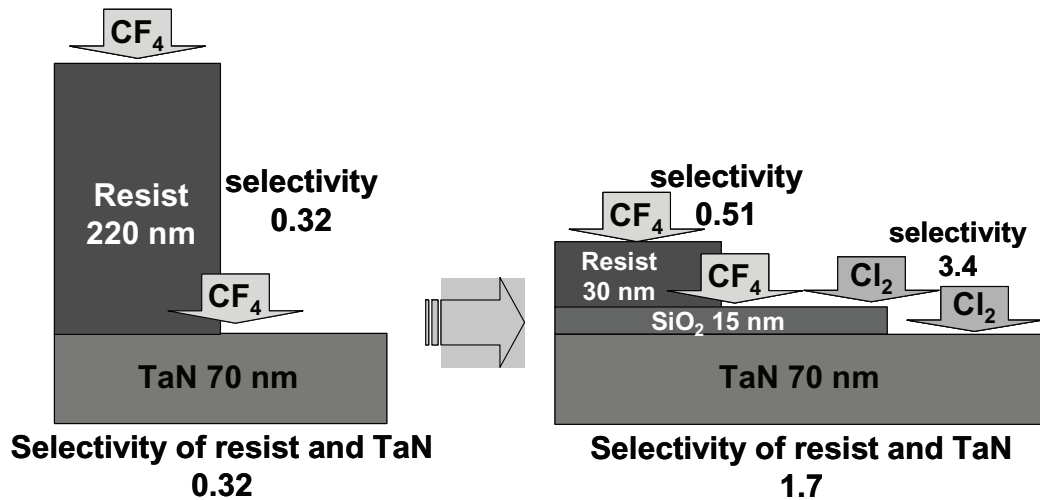


Fig. 10. Dry-etching selectivities of SiO<sub>2</sub> and TaN.

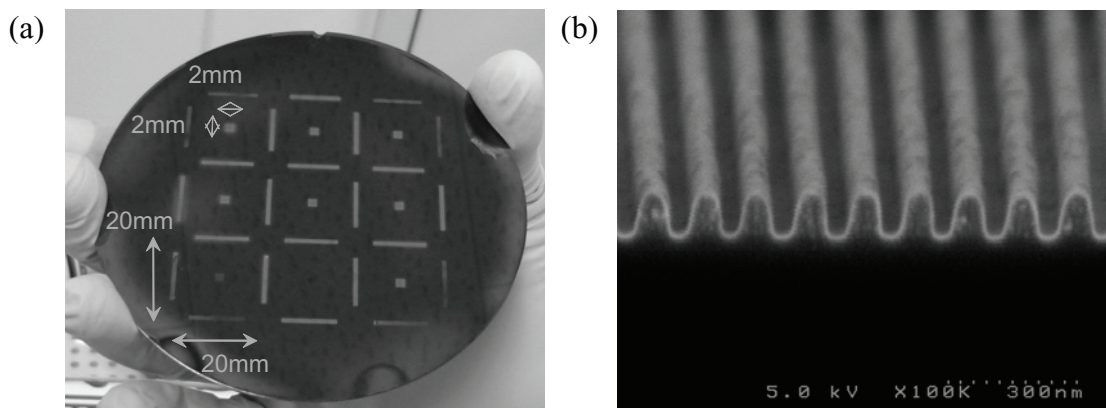


Fig. 11. (a) Photograph of a finished TaN transmission grating on a 4-in. silicon wafer after wet-etching, and (b) SEM image of the cross-sectional view of a 60-nm L/S grating pattern.

Furthermore, to improve the contrast of the interference fringes, the intensity of EUV light transmitted from outside a TaN grating patterned area has to be reduced with an additional resist absorber layer. Thus, a 1- $\mu\text{m}$ -thick ZEP520A resist was spin-coated on a TaN grating pattern, but only the TaN grating patterned area was exposed by the EB writing tool. After the development of the resist, the

residual resist on the TaN grating pattern was removed completely by a CF<sub>4</sub> dry-etch process. Thus, 70-nm-thick TaN and a 1- $\mu\text{m}$ -thick resist were used as an additional absorbers for the outside of a TaN grating patterned area, which has a total absorbance of 99.998% including the TaN and the additional resist layer of ZEP520A.

## 7. Conclusions

Extreme ultraviolet interference lithography was carried out at the long undulator beamline in NewSUBARU. It was confirmed in Young's double slit experiment that the spatial coherence length is 1.1 mm using a 10- $\mu\text{m}$ -wide slit. A 25-nm half-pitch (hp) resist pattern was successfully replicated by EUV-IL utilizing a two-window transmission grating pattern

with a 50-nm line and space (L/S). For the replication of a 20-nm L/S resist pattern and smaller by EUV-IL, we developed a fabrication process suitable for a transmission grating pattern of 40-nm L/S and smaller. Employing a hard-mask process using a silicon dioxide (SiO<sub>2</sub>) layer on a tantalum-nitride (TaN) layer in the fabrication of a two-window transmission grating, a fivefold larger dry-etch

selectivity in comparison with the non-hard-mask process was successfully achieved. As a result, we

confirmed the ability to apply this method to a 40-nm hp grating.

### Acknowledgment

We would like to thank the Japan Society for the Promotion Science for the Grant-in-Aid for Scientific Research.

### References

- 1) H. Kinoshita, K. Kurihara, Y. Ishii, and Y. Torii: *J. Vac. Sci. Technol. B* **7** (1987) 1648.
- 2) ITRS Road map: <http://www.itrs.net/>.
- 3) H. H. Solak, D. He, W. Li, S. Singh-Gasson, F. Cerrina, B. H. Sohn, X. M. Yang, and P. Nealey: *Appl. Phys. Lett.* **75** (1999) 2328.
- 4) H. H. Solak, C. David, J. Gobrecht, V. Golovkina, F. Cerrina, S. O. Kim, and P. F. Nealey: *Microelectron. Eng.* **67** (2003) 56.
- 5) M. Wei, D. T. Attwood, and T. K. Gustafson: *J. Vac. Sci. Technol. B* **12** (1994) 3648.
- 6) P. P. Naulleau, C. N. Anderson, and S. F. Horne: *Proc. SPIE* **6517** (2007) 65172T.
- 7) H. H. Solak: *J. Phys. D: Appl. Phys.* **39** (2007) R171.
- 8) H. Shiotani, S. Suzuki, D. Gun Lee, P. Naulleau, Y. Fukushima, R. Ohnishi, T. Watanabe, and H. Kinoshita: *Jpn. J. Appl. Phys.* **47** (2008) 4881.
- 9) H. H. Solak, D. He, W. Li, and F. Cerrina: *J. Vac. Sci. Technol. B* **17**(6) (1999) 3052.
- 10) S. Suzuki, Y. Fukushima, R. Ohnishi, T. Watanabe, and H. Kinoshita: *J. Photopolym. Sci. Technol.* **21** (2008) 435.
- 11) Y. Ekinci, H. H. Solak, C. Padeste, J. Gobrecht, M. P. Stoykovich, and P. F. Nealey: *Microelectron. Eng.* **84** (2007) 700.
- 12) A. Isoyan, Y.-C. Cheng, F. Jiang, J. Wallace, M. Efremov, P. Nealey, and F. Cerrina: *Proc. SPIE* **6921** (2008) 69212R.
- 13) D. T. Attwood, P. Naulleau, K. A. Goldberg, E. Tejnil, C. Chang, R. Beguiristain, P. Batson, J. Bokor, E. M. Gullikson, M. Koike, H. Medeck, and J. H. Underwood: *IEEE J. Quantum Electron.* **35** (1999) 709.
- 14) S. Hashimoto, A. Ando, M. Nibe, S. Miyamoto, Y. Shoji, Y. Fukuda, T. Tanaka, and Y. Gomei: *Nucl. Instrum. Methods Phys. Res., Sect. A* **467** (2001) 141.
- 15) Y. Nagata, K. Furusawa, Y. Nabekawa, and K. Midorikawa: *Opt. Lett.* **32** (2007) 722.
- 16) H. F. Schouten, T. D. Visser, and E. Wolf: *Opt. Lett.* **28** (2003) 1182.
- 17) P. P. Naulleau, C. H. Cho, E. M. Gullikson, and J. Bokor: *J. Synchrotron Radiat.* **7** (2000) 405.
- 18) <http://www-cxro.lbl.gov/>
- 19) K. Sato, M. Shikida, Y. Matsushima, T. Yamashiro, K. Asaumi, Y. Iriye, and M. Yamamoto: *Sens. Actuators A* **64** (1998) 87.

# High-Precision Analysis for Material Analysis Beamline at BL05 for Industrial Enterprises

T. Hasegawa<sup>1</sup>, M. Uemura<sup>1</sup>, M. Motoyama<sup>2</sup>, S. Matsui<sup>2</sup> and K. Kanda<sup>2</sup>  
1 Synchrotron Analysis L.L.C., Hyogo-ku, Kobe, Hyogo 652-0863 Japan  
2 University of Hyogo, Kamigori, Ako, Hyogo 678-1205 Japan

## Abstract

A material analysis beamline for the industrial enterprises' use was completed at BL05 in March 2008. BL05 consists of two branch lines, one is a double crystal monochromator beamline (BL05A) for the use in the higher-energy region (1300-4000 eV) and the other is a varied line spacing plane grating (VLSPG) monochromator beamline (BL05B) for the use in the lower-energy region (50-1300 eV), which cover the whole energy range of the soft X-ray region from 50 eV to 4000 eV. These two branch lines can be operated simultaneously. The X-ray absorption fine structure (XAFS) measurements in the total electron yield (TEY) and fluorescence yield (FLY) can be performed at BL05A and BL05B. In addition, the X-ray photoelectron spectra (XPS) can be measured at BL05B.

## Introduction

Recently, the needs for material analysis in the soft X-ray region using synchrotron radiation has increased in the analysis industry. A material analysis beamline for the industrial enterprises' use was completed at BL05 in March 2008. The whole useful energy range of the BL05 is the soft X-ray region from 50 to 4000 eV and X-ray absorption spectrum can be measured with a high-energy resolution. BL05 will be managed and maintained by the Synchrotron Analysis L.L.C. (SALLC), which is composed of the industrial companies, in cooperation with the staffs of the Laboratory of Advanced Science and Technology for Industry in University of Hyogo. Industrial users can be assisted by staffs of SALLC in the measurement at BL05. In this paper, we will introduce BL05 and report recent activities.

## Layout of BL05

Bending magnet beamline BL05 consists of two branch lines (BL05A, BL05B) for the use in the wide range from 50 eV to 4000 eV. Photo.1 shows a photograph of BL05. BL05A, which is mounted with a double crystal monochromator, can be used in the energy range of 1300-4000 eV by exchanging several monochromatizing crystals. On the other hand, BL05B is mounted with a varied line spacing plane grating (VLSPG) monochromator, which is designed to cover the energy range 50-1300 eV with three gratings. Because the incident beam from the bending magnet is provided for two branch lines through the different windows of mask, these lines can be operated simultaneously.

## Specifications of BL05A

Toroidal mirrors are used as a pre-mirror and a focusing mirror of BL05A, for the purpose to introduce a high-photon flux to the end station. InSb (111) crystals and Si (111) crystals are prepared for a Golovchenko-type double crystal monochromator. The XAFS measurements in the total electron yield

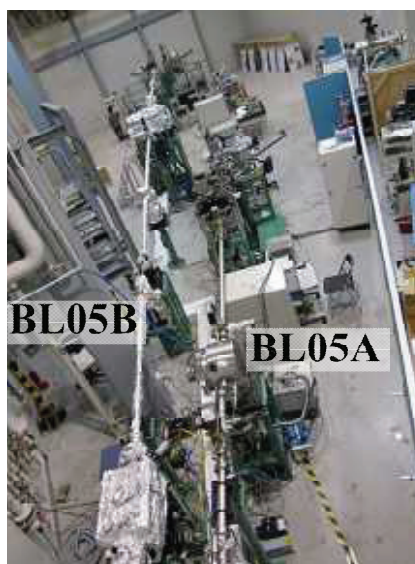


Photo.1 Photograph of beamline BL05.

(TEY) and fluorescence yield (FLY) using SDD (SII, Vortex) can be performed. The fluorescence XAFS spectra can be measured samples at the under an atmospheric pressure by the replacement of an end station to He using Be window. The chamber can maintain 8 samples of 25 mm corner because of industrial use.

## Specifications of BL05B

The constant-deviation monochromator consisting of a demagnifying spherical mirror and VLSPG, which can provide to high resolution, simple wavelength scanning with fixed slits, was mounted on BL05B. The including angle of the monochromator is 175°. VLSPG consists of three gratings (100-, 300- and 800-lines/mm). Fig.1 shows a calculated diffraction efficiency of each grating. Expected resolution ( $E/\Delta E$ ) is 3,000. Two

measurement chambers are prepared at the end station of BL05B. The XAFS spectra in the total electron yield and fluorescence XAFS spectra using SSD (EDAX) can be measurement in the high vacuum chamber. In addition, the X-ray photoelectron spectra (XPS) using spherical electron analyzer (VG Scienta, R3000) can be measured in the ultra high vacuum chamber. These chambers can be replaced each other within 1 hour. Each chamber can maintain 16 samples of 25 mm corner.

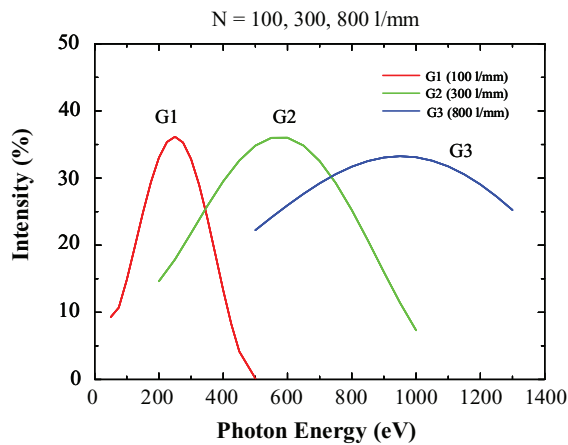


Fig.1 Diffraction efficiency of BL05B.

### Measurement

We measured standard samples by means of the TEY method at BL05B and obtained absorption spectra in each grating, 100- or 300- or 800-lines/mm. Fig.2-4 show boron K-edge, calcium and nickel  $L_{3,2}$ -edge near-edge X-ray absorption fine structure (NEXAFS) spectra of *h*-BN,  $\text{CaF}_2$  powder and Ni sheet. The spectrum have been normalized to  $I_0$  and had a linear pre-edge background removed. For *h*-BN, an intense peak at 191 eV appeared clearly in Fig.3, which is assigned to transition from  $B1s$  to the

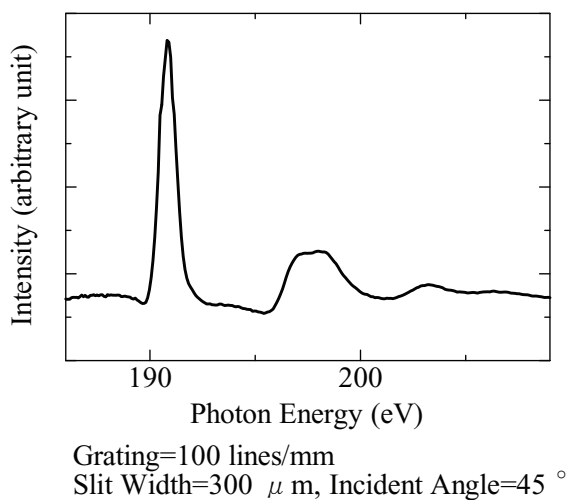


Fig.2 *h*-BN B K-edge NEXAFS spectrum.

unoccupied  $B2p \pi^*$ , the spectrum was the same shape as the one Jiménez et al. reported [1]. Additionally, the calcium  $L_{3,2}$ -edge spectral shape of  $\text{CaF}_2$  almost corresponds to the spectrum reported by Naftel et al. [2]. The nickel  $L_{3,2}$  absorption peaks are observed at 853 and 871 eV, respectively [3].

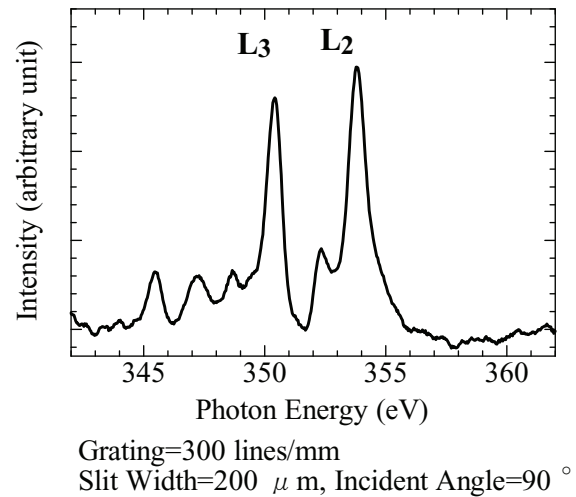


Fig.3  $\text{CaF}_2$  Ca  $L_{3,2}$ -edge NEXAFS spectrum.

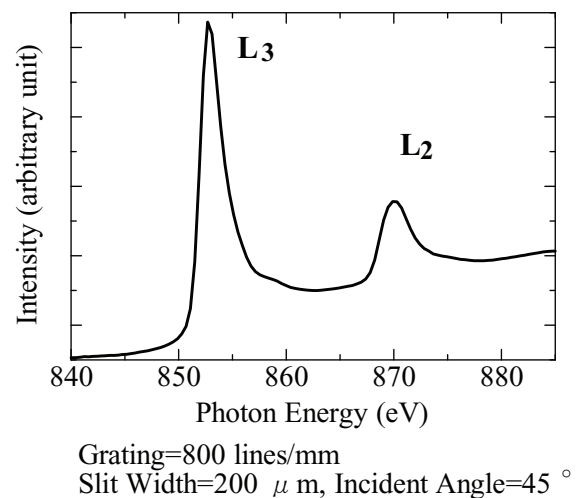


Fig.4 Ni  $L_{3,2}$ -edge NEXAFS spectrum.

### References

- [1] I.Jiménez, A.F.Jankowski, L.J.Terminello, D.G.J. Sutherland, J.A.Carlisle, G.L.Doll, W.M.Tong, D.K. Shuh, F.J.Himpsel: *Phys. Rev.*, **B55**, 12027 (1997).
- [2] S.J.Naftel, T.K.Sham, Y.M.Yiu, B.W.Yates: *J. Synchrotron Rad.*, **8**, 255 (2001).
- [3] J.A.Bearden, A.F.Burr: *Rev. Mod. Phys.*, **39**, 125 (1967).

# Effect of the Soft X-ray on the Highly-Hydrogenated Diamond-Like Carbon Film

Kazuhiro Kanda<sup>1</sup>, Kumiko Yokota<sup>2</sup>, Masahito Tagawa<sup>2</sup>, Mayumi Tode<sup>3</sup>, Yuden Teraoka<sup>3</sup>, Shinji Matsui<sup>1</sup>  
<sup>1</sup>Laboratory of Advanced Science and Technology for Industry, University of Hyogo, <sup>2</sup> Graduate School of Engineering, Kobe University, <sup>3</sup> Japan Atomic Energy Agency  
E-mail: kanda@lasti.u-hyogo.ac.jp; Tel.: +81-791-58-0476

## Abstract

Hydrogen was found to emit from the highly-hydrogenated Diamond-Like Carbon (H-DLC) films by the irradiation of synchrotron radiation (SR) even in the vacuum. The hydrogen content in the H-DLC film decreased exponentially with a soft X-ray exposure dose. In addition, the decrement of hydrogen content was found to decrease with increasing of the initial hydrogen content in the H-DLC film. It was interpreted that the etching rate of H-DLC increased with its hydrogen content.

## Introduction

Diamond-Like Carbon (DLC) films generally have durability against the synchrotron radiation (SR) in the absence of oxygen gas.<sup>1)</sup> Recently, hydrogen was emitted from the highly-hydrogenated DLC (H-DLC) films by the irradiation of soft x-ray even in the vacuum, and increase in the film density, hardness and refractive index were reported.<sup>2)</sup> In the present study, we investigated the departure process of hydrogen from the highly-hydrogenated DLC film by the exposure to soft X-ray in the vacuum using three kinds of highly-hydrogenated DLC thin films, which contained difference hydrogen contents.

## Experiments and Results

Highly-hydrogenated DLC thin films were deposited on Si wafer with 200 nm thickness by amplitude-modulated RF plasma-CVD method.<sup>3)</sup> We called these films H-DLC50, H-DLC40 and H-DLC30, in order of hydrogen content. The irradiation of SR against DLC films was carried out at BL-6 of NewSUBARU.<sup>4)</sup> The SR at the BL-6 sample stage had a continuous spectrum from IR to soft X-ray, which was lower than 1 keV. Rutherford backscattering spectrometry (RBS) and elastic recoil detection analysis (ERDA) are available for evaluating quantitative determination for all elemental composition, specially hydrogen, of thin films with high accuracy, being unnecessary for standard samples. In this study, the hydrogen content of DLC film has been determined by RBS and ERDA techniques using a tandem Pelletron accelerator, SSDH-2 in the Kobe University. Figure 1 depicts the SR dose dependences of hydrogen content estimated using ERDA/RBS techniques. The hydrogen content in the low-hydrogenated DLC film kept constant independent on a soft X-ray exposure dose. On the other hand, that in the high-hydrogenated DLC film decreases exponentially with a soft X-ray exposure dose. Thus, the departure of the hydrogen was observed from high-hydrogenated DLC films, while was not observed from the low-hydrogenated DLC film by soft X-ray irradiation. The mechanism of the departure process of hydrogen from DLC film by SR

exposure was discussed on the basis of the measurements of etching depth and thermal desorption spectra.

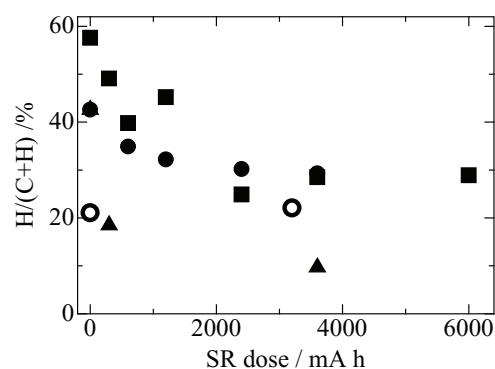


Fig. 1 The SR dose dependences of the hydrogen content. Circle, square, and triangle indicate H-DLC50, H-DLC40 and H-DLC30 respectively. Open circle indicates low hydrogenated DLC film synthesized using PBII/D method.

## References

- [1] H. Kyuragi and T. Urisu, *Appl. Phys. Lett.*, **50** (1987) 1254
- [2] H. Matsuura, et. al., *SEI Technical Review*, **171** (2007) 39 (Japanese)
- [3] T. Nakahigashi, et. al., *Tribology International*, **37** (2004) 907
- [4] K. Kanda, et. al., *Jpn. J. Appl. Phys.*, **42** (2003) 3983

**Acknowledgements:** A part of this work was supported by the New Energy and Industrial Technology Development Organization (NEDO) under the work entitled “Advanced Fundamental Research Project on Hydrogen Storage Materials”. We also thank to use SSDH-2 of Accelerator and Particle Beam Experimental Facility, Faculty of Maritime Sciences, Kobe University for the RBS measurement.

# Photoemission Study of Hydrogenated Amorphous Carbon Thin Films as a Function of Annealing Temperature

Yuichi Haruyama<sup>1</sup>, Masahito Tagawa<sup>2</sup>, Kumiko Yokota<sup>2</sup>, and Shinji Matsui<sup>1</sup>  
<sup>1</sup> Laboratory of Advanced Science and Technology for Industry, University of Hyogo  
<sup>2</sup> Graduate School of Engineering, Kobe University

## Abstract

The electronic structure in hydrogenated amorphous carbon (a-C:H) thin films was investigated as a function of the annealing temperature using photoemission spectroscopy. The photoemission results of the valence band and the C 1s core level suggested that the graphitization of the a-C:H film proceeds by annealing at more than 400 °C. From the photoemission spectra of the C 1s core level, the coordination of C atoms in the a-C:H film were evaluated as a function of the annealing temperature. Based on the evaluations, the electronic structure of the a-C:H film as a function of the annealing temperature is discussed.

## Introduction

Since amorphous carbon thin films have interesting properties such as high hardness, low friction coefficient, and chemical inertness, the study of amorphous carbon thin films has attracted a great deal of attention for wide applications [1-2]. Due to their properties, amorphous carbon films are mainly used in industrial products as coatings for the magnetic heads and media of hard disk drives, the machine parts for mold, the cutting tools, etc. In order to produce good amorphous carbon films, various vapor phase methods have been extensively attempted so far, and the properties of the hydrogenated amorphous carbon (a-C:H) films formed by vapor phase methods have been studied. In the previous studies using Raman and Auger electron spectroscopy, the a-C:H films were thermally stable up to 260 °C. However, it was pointed out that the thermal stability in the a-C:H films was not good at more than 300-400 °C due to the hydrogen desorption and the graphitization of a-C:H films.

Although photoemission spectroscopy studies are important to investigate the electronic structure such as the density of states, the orbital characteristic, the  $sp^2$  and  $sp^3$  contents, etc., there are few reports on photoemission spectra of the valence band region and C 1s core level in the a-C:H films [3-4]. In particular, the evolution of photoemission spectra of the valence band region and C 1s core level in the a-C:H films as a function of the temperature has not been clarified. In this study, we investigated the electronic structure in the a-C:H film as a function of the annealing temperature using photoemission spectroscopy.

## Results and discussion

Figure 1 shows the photoemission spectra of the valence band region in the a-C:H film as a function of the annealing temperature. The annealing temperatures of a-C:H film are denoted beside each spectrum. In the top, the photoemission spectrum in graphite is located for

comparison. After annealing at 200 °C, no clear change was observed as compared to the photoemission spectrum at RT. With increasing the annealing temperature at 400 °C, a small peak at 3.0 eV appeared. With increasing the annealing temperature at 600 °C, several peaks were clearly observed at 19.0, 13.0, 10.0, 7.8, 5.5 and 3.0 eV. With further increasing the annealing temperature at 800-950 °C, a peak at 6.7 eV in addition to the several peaks at 19.0, 13.0, 10.0, 7.8, 5.5 and 3.0 eV were observed. The photoemission spectra after annealing at 600-950 °C are similar to that of graphite except for the peak at 6.7 eV. Therefore, the several peaks at 19.0, 13.0, 10.0, 7.8, 5.5 and 3.0 eV are derived from graphite although the origin of the peak at 6.7 eV is not clear at present. This indicates that the annealing at 600-950 °C causes the graphitization of a-C:H film. In addition, the observation of the peak at 3.0 eV after annealing at 400 °C suggests that the graphitization of a-C:H film starts to arise below this temperature.

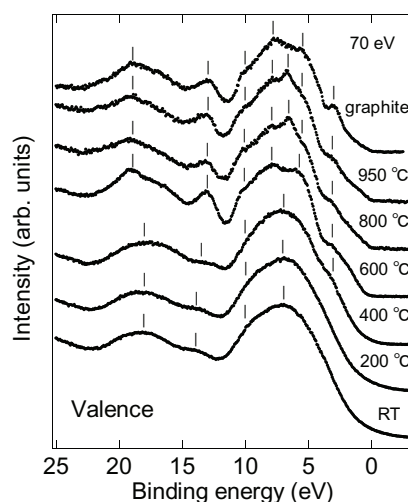


Fig.1 Photoemission spectra of the valence band region in the hydrogenated amorphous carbon film as a function of the annealing temperature.

Figure 2 shows the photoemission spectra (dots) of the C 1s core level in the a-C:H film as a function of the annealing temperature. A shift of the peak position to the lower binding energy side was observed with increase the annealing temperature. In addition, the width of the photoemission spectra of the C 1s core level in a-C:H films were observed to be narrower with increase the annealing temperature. In the photoemission spectrum in graphite, a peak at ~284.4 eV with a wide tail to the higher binding energy side was observed. The photoemission spectrum of the C 1s core level in the a-C:H film after annealing at 950 °C is similar to that of graphite. The broader spectral feature at lower temperature suggests that there are some C 1s components in different chemical environments. In the previous photoemission study of unhydrogenated amorphous carbon films, the photoemission spectra of the C 1s core level were essentially composed of two components positioned at 284.4 and 285.2 eV [5-6]. From the position of the binding energy in graphite and diamond, the two components at 284.4 and 285.2 eV were assigned to the C 1s electrons originating from the  $sp^2$  and  $sp^3$  hybridized carbon atoms, respectively. In the case of a-C:H films, the contribution from the C-H bonded carbon atoms in addition to the  $sp^2$  and  $sp^3$  hybridized carbon atoms would be needed. In the previous photoemission spectrum of the C 1s core level in the hydrogen terminated C(111) surface, only a single peak was observed, indicating that the binding energy of the bulk C 1s component is same as that of C-H bonded C 1s component [7]. This also suggests that the electro-negativity of carbon atoms is similar to that of hydrogen atoms on the hydrogen terminated C(111) surface. Therefore, the C 1s electrons originating from the C-H bonded carbon atoms were tentatively assigned to the component at 285.2 eV. In this case, it is difficult to reliably distinguish between the  $sp^3$  hybridized and the C-H bonded carbon atoms from the photoemission spectra. In the previous study of a-C:H films formed by the vapor phase methods such as the ion plating and ECR plasma methods [4], the  $sp^2$  contents estimated from the XPS spectra were in good correspondence to those estimated from the EXAFS spectra although there is an influence of the C-H bonded carbon atoms on the photoemission spectra of the C 1s core level. This result suggests that there is almost no influence on the estimation of the  $sp^2$  hybridized carbon atoms using the XPS spectra. Therefore, the contents of the  $sp^2$  hybridized carbon atoms and the contents of the sum of the  $sp^3$  hybridized and the C-H bonded ( $sp^3 + C-H$ ) carbon atoms could be estimated using the XPS spectra. For this reason, a curve fitting analysis was performed on the photoemission spectra of the C 1s core level using two components positioned at 284.4 and 285.2 eV. In Fig. 2, the best fitting results (lines) for a-C:H films are shown. The  $sp^2$  and  $sp^3 + C-H$  carbon

contents in a-C:H films, which are evaluated from the area intensity of each component, are summarized in Ref. 8. The error range for evaluation of the  $sp^2$  and  $sp^3 + C-H$  carbon contents was  $\pm 5\%$ . After annealing at 200 °C, almost no change was observed. With increasing the annealing temperature at 400 °C, the  $sp^2$  carbon content increased by 5%. With increasing the annealing temperature at 600 °C, the  $sp^2$  carbon content increased rapidly by 18%. With further increasing the annealing temperature at 800-950 °C, the  $sp^2$  carbon content increased gradually. The  $sp^2$  content in the a-C:H film after annealing at 950 °C was shown to be highest as compared with those after annealing at less than 800 °C. These results indicate that the graphitization of a-C:H films starts below 400 °C and proceeds with increasing the annealing temperature.

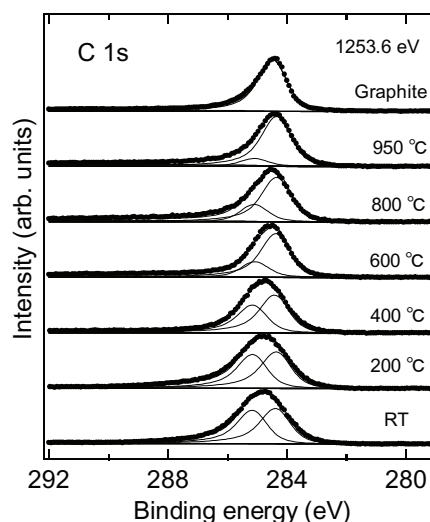


Fig.2 Photoemission spectra (dots) of the C 1s core level in the hydrogenated amorphous carbon film as a function of the annealing temperature. In the top, the photoemission spectrum of graphite is located for comparison. The fitting results (lines) are also plotted in each spectrum.

## References

- [1] J. Ullmann, Nucl. Instrum. Methods Phys. Res., Sect. B **127** (1997) 910.
- [2] H. Tsai and D. B. Bogy, J. Vac. Sci. Technol. A **5** (1987) 3287.
- [3] J. Schafer *et al.*, Phys Rev B **53** (1996) 7762.
- [4] Y. Haruyama *et al.*, Jpn. J. Appl. Phys. **47** (2008) 3380.
- [5] P. Merel *et al.*, Appl. Surf. Sci. **136** (1998) 105.
- [6] J. Diaz *et al.*, Phys. Rev. B **54** (1996) 8064.
- [7] J. F. Morar *et al.*, Phys. Rev. B **33** (1986) 1340.
- [8] Y. Haruyama *et al.*, Jpn. J. Appl. Phys. **48** (2009) 055505-3.

# Control of Oxygen Contamination in BN Thin Film Prepared by Reactive Magnetron Sputtering

Masahito Niibe and Yoshie Maeda  
LASTI, University of Hyogo

## Abstract

To control oxygen contamination in BN thin film prepared by sputtering technique, high purity gases of Ar:6N and N<sub>2</sub>:6N5 were used for magnetron sputtering as well as inserting purifier into the gas line. The vacuum chamber was baked at low temperature of 60 °C for about 17 hrs before thin film preparation. Oxygen concentration was evaluated by B-K edge X-ray absorption spectroscopy (XAS) as well as XPS and XAS analyses. It was found that the amount of oxygen contamination was controlled to be less than 1.4 % in the prepared BN thin film.

## Introduction

For fabrication of metal nitride thin films by reactive sputtering, oxygen contamination becomes often problematic. For example, ultra high vacuum system was proposed to use for preparation of titanium nitride thin film [1]. However, in the thin film fabrication system practically used for coating of mechanical tools, it is necessary to develop the technique to control oxygen contamination for open-air thin film fabrication system. We examined the contamination control technique in preparation of boron nitride (BN) thin film which is one of the easily oxidizing materials.

## Experiments

The BN thin films were fabricated by an RF magnetron sputtering system with open-air type sample changing. The cross-sectional schematic view of the system is shown in Fig. 1. The back ground pressure of the preparation chamber was about  $2 \times 10^{-4}$  Pa. Mixed gas of Ar and N<sub>2</sub> with mixing ratio of 1:1 was used for sputtering. The target was a sintered h-BN with 125 mm in diameter. The substrate temperature was not controlled and was less than 50 °C during the sample preparation. We supposed that the origins of oxygen contamination were residual water vapor in the chamber and also water and

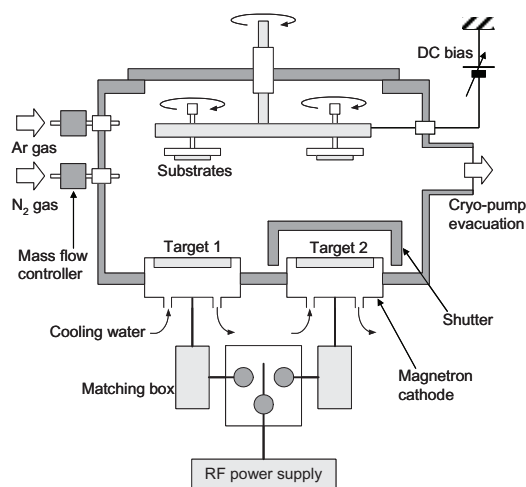


Fig. 1 Cross-sectional schematic view of the RF magnetron sputtering system.

oxygen gas contained in the sputtering gases from the gas cylinders. The purity of used gas was improved from 99.999% to 99.9999% (6N) for Ar and from 99.9995% to 99.99995% (6N5) for N<sub>2</sub> gas in the cylinder. Gas purifiers (PURERON GP-05) were also inserted into the gas introduction lines. The vacuum chamber was baked at low temperature of 60 °C for about 17 hrs before thin film preparation.

Oxygen concentration in the prepared film was evaluated by X-ray photoemission spectroscopy (XPS, Shimazu ESCA-1000) and B-K edge X-ray absorption spectroscopy (XAS) at the BL9 [2] in the NewSUBARU SR facility. The XAS measurement was carried out by total electron yield (TEY) mode with measuring sample current when the photoelectron emitted by soft X-ray absorption. An Auger electron spectroscopy (AES) was also employed for depth analysis.

## Results

Figure 2 shows a B-K edge XAS spectrum of a prepared BN thin film, the oxygen concentration of which was comparatively high. The structure of the BN film was hexagonal (h-BN). Four sharp  $\pi^*$  resonance peaks were observed at the photon energy from 192 to 194eV. These peaks were formerly

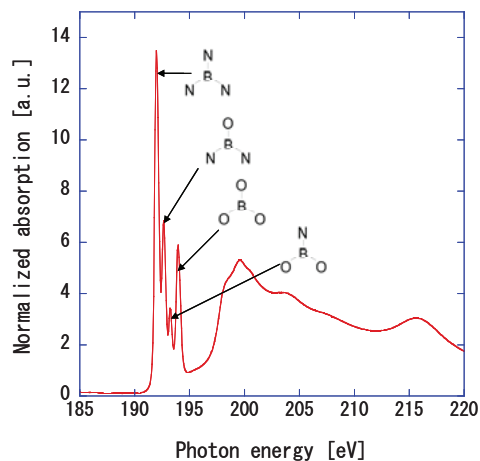
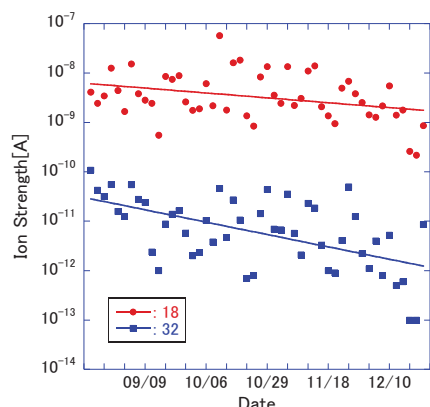


Fig. 2 Typical B-K edge XAS spectrum of a prepared BN thin film.

identified by the authors [3] as B atoms coordinated by three N atoms (192.0 eV), and B atoms bound to one-to-three oxygen atoms substituted for three nitrogen atoms surrounding for higher energy three peaks as shown in the figure.

Figure 3 shows the QMS intensity change of residual H<sub>2</sub>O(18) and O<sub>2</sub>(32) components in the chamber during the long term baking. Although, the data scattered day by day, the average amounts of residual gases in the chamber decreased 79% for H<sub>2</sub>O and 92% for O<sub>2</sub> during four months operation.



**Fig. 3** QMS intensity change of residual H<sub>2</sub>O(18) and O<sub>2</sub>(32) components in the chamber during the long term baking.

B-K edge XAS spectra of prepared BN thin films before and after improvement in vacuum atmosphere is shown in Fig. 4. The intensity of three  $\pi^*$  peaks at the higher energy side decreased remarkably after the improvement. A curve fitting calculation indicates that ratio N and O atoms bonding to the B atoms for the sample of before the improvement was 73% and 27%, respectively. However, the values changed for the sample after improvement as 92% and 8%, respectively.

Depth analysis of the prepared sample was carried out by AES analyzer at the Faculty of Engineering, University of Hyogo, because etching gun for depth

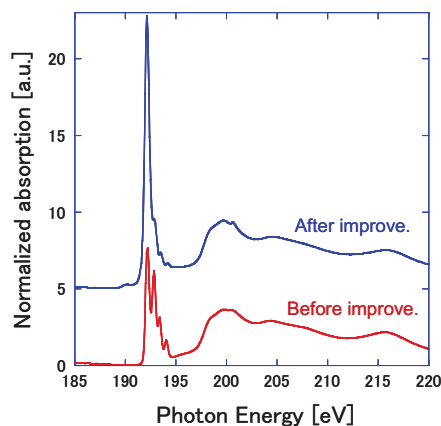


**Fig. 4** B-K edge XAS spectra of prepared BN thin films before and after the improvement in vacuum atmosphere.

analysis was not provided yet for XPA and XAS equipments. Figure 5 show the AES spectra of prepared BN thin film before and after the Ar ion etching. Some amounts of oxygen and carbon were observed on the surface of the thin film as-deposited and exposed to open air. The oxygen concentration at the surface evaluated by AES measurement was about 5 atomic %. However, after the 100 sec etching with Ar ion, the oxygen concentration decreased rapidly to about 1.4%.

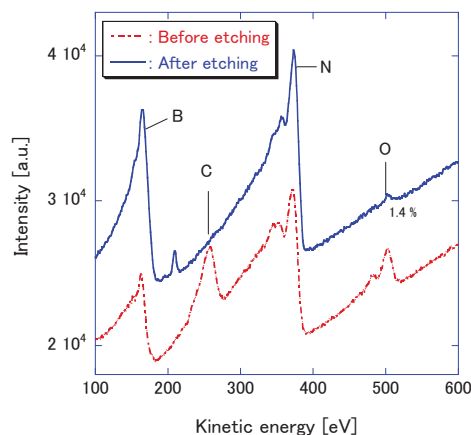


**Fig. 5** AES spectra of BN thin film prepared before and after the Ar ion etching.

## Conclusion

The oxygen contamination was successfully controlled by using high purity sputtering gas and long term baking with low temperature for open air type magnetron sputtering system.

## Acknowledgment

The authors thank to Prof. Shozo Inoue at the University of Hyogo for his support to measure the AES depth profile and the spectra.

## References

- [1] K. Hoshi *et al.*, Proc. ISSP2007 Kanazawa Japan.
- [2] M. Niibe *et al.*, AIP Conf. Proc. **705** 576 (2004).
- [3] M. Niibe *et al.*, Bulletin Soc. Discrete Variational Xa, **21**, 179 (2008).

# Semi-quantitative analysis of carbon contamination on MLMs using high power EUV light

Takahiro Nakayama<sup>a</sup>, Hiroyoshi Kubo<sup>a</sup>, Akira Miyake<sup>a</sup>, Hiromitsu Takase<sup>a</sup>, Shigeru Terashima<sup>a</sup>,  
Shintaro Kawata<sup>b</sup>, Takashi Aoki<sup>b</sup>, Shuichi Matsunari<sup>b</sup>,  
Hiroo Kinoshita<sup>c</sup>, Takeo Watanabe<sup>c</sup>, Masahito Niibe<sup>c</sup>

<sup>a</sup>Canon, 23-10, Kiyohara-Kogyodanchi, Utsunomiya-shi, Tochigi-ken, 321-3298, Japan

<sup>b</sup>Nikon, 1-10-1, Asamizodai, Sagamihara-shi, Kanagawa-ken, 228-0828, Japan

<sup>c</sup>Laboratory of Advanced Science and Technology for Industry (LASTI), Univ. of Hyogo, 3-1-2, Kouto, Kamigori-cho, Ako, Hyogo 678-1205, Japan

## Abstract

It is very important to mitigate oxidation of multilayer mirrors (MLMs) and carbon deposition onto MLMs to extend the lifetime of EUV exposure tool. In this study we focused on carbon deposition on Si-capped multilayer mirror. We made experiments of EUV irradiation to the MLMs using apparatuses connected to an undulator beamline (BL9) of synchrotron radiation facility New SUBARU in the University of Hyogo. This undulator beamline stably gives us high-power EUV light. As the result of experiments, we found that carbon deposition rate was constant until carbon thickness became 2.5 nm.

## Introduction

HVM (High Volume Manufacturing) EUV Scanner is needed to operate for several years without high maintenance cost. In order to estimate a lifetime for HVM, we have to figure out scaling law. We focus on the scaling law of contaminations on multilayer mirrors (MLMs). Carbon deposition on MLMs causes a damage of optical performances. We have to elucidate a photochemical reaction of EUV irradiation to the MLMs and estimate carbon deposition rate for HVM. We have found dependences of carbon deposition rate on average EUV intensity, hydrocarbon partial pressure, characteristics of EUV source<sup>1-3</sup>. We have elucidated these dependences by carbon deposition rate. But we do not know whether carbon deposition rate is constant or not. So we need to make sure if carbon deposition rate is constant to understand the reaction quantitatively.

## Experiments and Results

We made experiments using an apparatuses connected to an undulator beamline (BL9) in NewSUBARU synchrotron radiation facility in the University of Hyogo. Figure 1 shows schematic diagram of the apparatus.

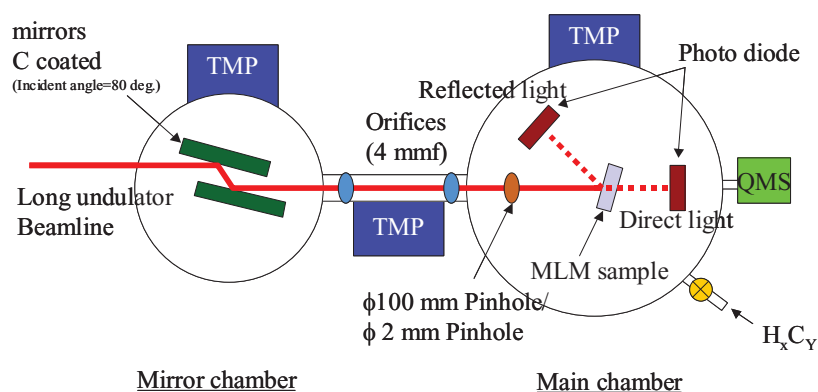


Figure 1. Schematic diagrams of EUV irradiation apparatus

We used X-ray photoelectron spectroscopy (XPS) and obtained carbon deposition quantity from photoelectron intensity of C(1s). We converted photoelectron intensity of C(1s) into a carbon film thickness. Furthermore, we calculated carbon deposition rate by dividing the carbon film thickness by the total irradiation time. The average EUV intensity distribution is shown in Fig. 2. Figure 2 also shows carbon thickness distribution as an example. Dependence of carbon deposition rate on average EUV intensity was figured out using these data. Figure 3 shows the dependence of carbon deposition rate on average EUV intensity. Decane (C<sub>10</sub>H<sub>22</sub>) was injected at the partial pressure of 1E-6 Pa. The carbon deposition rate does not increase proportionally to the average EUV intensity.

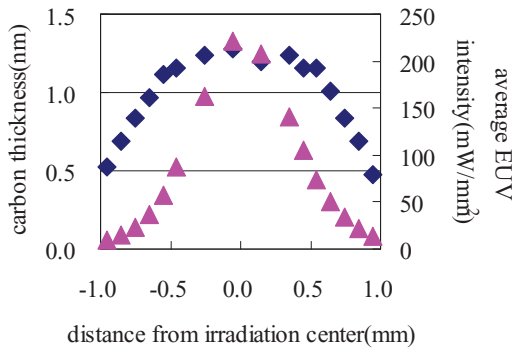


Figure 2. Distribution of Carbon thickness and average EUV intensity

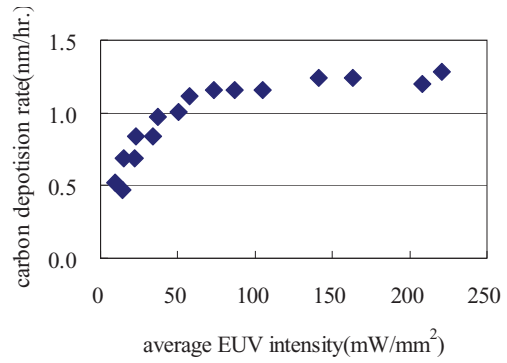


Figure 3. Dependence of carbon deposition rate on average EUV intensity

A standing wave on MLMs affects on generating secondary electrons<sup>4</sup>. It is considered that carbon is deposited by interaction between secondary electrons and adsorbed molecules. So carbon deposition rate must be changed by the standing wave. We made experiments to figure out if carbon deposition rate changes depending on time during EUV irradiation. Experimental results show time dependence of carbon thickness in fig. 4. The result is comparing between two different EUV intensities. Carbon thickness was increasing constantly until it became 2.5 nm. We fitted experimental data by least square method and it was good agreement.

Table 1. Experimental conditions.

Decane partial pressure (Pa)	Irradiation time (min.)
1E-5	5
1E-5	15
1E-5	30

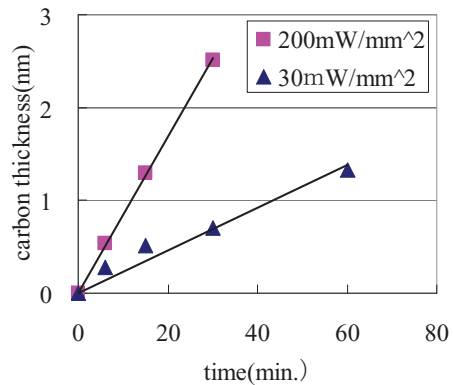


Figure 4. Time dependence of carbon thickness

In conclusion, we made experiments using an undulator beamline (BL9) in NewSUBARU synchrotron radiation facility and figured out dependence of carbon deposition rate on average EUV intensity up to high EUV intensity. We also figured out if carbon deposition rate is constant. The carbon deposition rate does not depend on carbon thickness until it becomes 2.5 nm. The standing wave does not affect on carbon deposition on our MLMs so much. As future works, we need to calculate amount of secondary electrons depending on carbon thickness and compare simulation with experimental results.

#### ACKNOWLEDGMENT

A part of this work was supported by the Ministry of Economy Trade and Industry (METI) and New Energy and Industrial Technology Development Organization (NEDO).

#### REFERENCES

- [1] H. Takase, "Study of Ruthenium-capped Multilayer Mirror for EUV Irradiation Durability", Proc. of SPIE Vol. 6151, 35, 2006
- [2] T. Nakayama, "Phenomenological analysis of carbon deposition rate on the multilayer mirror", Proc. of SPIE Vol. 6921, 3B, 2008
- [3] T. Nakayama, et. al., "Analysis of carbon deposition on multilayer mirrors by using two different beamlines", Proc. of SPIE 7271(2009) 72713P.
- [4] S. B. Hill et. al., "Accelerated lifetime metrology of EUV multilayer mirrors in hydrocarbon environments", Proc. of SPIE 6921,42, 2008

# Electronic State of Ti in Ultra-fine Grained SUS316L-1%TiC

M. Terasawa, T. Mitamura, M. Niibe, LASTI, University of Hyogo  
T. Yamasaki, Dept. of Materials and Chemistry, Graduate School of Engineering, University of Hyogo  
H. Kurishita, Institute for Materials Research (IMR), Tohoku University  
M. Kawai, Institute of Material Structure Science, High Energy Accelerator Research Organization (KEK)

## Abstract

Ultra fine grained (UFG) materials of SUS316L were fabricated by mechanical alloying (MA) and hot isostatic pressing (HIP) treatments. It was found that addition of about 1 % TiC powder was effective to reduce the grain size down to 100 nm, and the materials exhibited superior irradiation resistance and mechanical properties. The electronic states of the TiC in the UFG materials were analyzed by XANES spectroscopy at NewSUBARU BL9.

## Introduction

In the J-PARC program, which is a large accelerator development project in Japan to promote use of secondary particles, such as neutron, pi- and myu-particles, neutrino and so on, very high energy and high current proton beams are utilized. For the neutron source in the J-PARC facility, liquid mercury target enveloped with metallic container is planned to be adopted. The container materials must be tough for heavy irradiation induced by intense proton and neutron flux, in addition to severe erosion due to mercury exposure. One of the candidate materials is ultra fine grained (UFG) SUS316L-1%TiC. It is strongly expected that the materials are developed so as to show tough resistance for such phenomena.

We are developing ultra-fine grained materials of austenitic stainless steel (316L) with addition of small amount of TiC powder. In this work, electronic state analysis of TiC in the UFGSUS316L-TiC materials was investigated by XANES spectroscopy in order to elucidate the effect of TiC addition.

## Experiments and Results

### *Fabrication of ultra-fine grained materials*

Ultra-fine grained materials of austenitic stainless steel (SUS316L) were fabricated by mechanical-alloying (MA) and hot isostatic pressing (HIP) treatments. Powder of SUS316L (an average particle size: 44 – 105  $\mu$  m), combined with TiC (0.57  $\mu$  m), was used as the starting materials.

The SUS316L-1.0wt.% TiC materials with the average grain sizes of 100 nm were obtained by 80 % cold roll and annealing at the temperature of 800°C, after MA and HIP (800°C) treatment. The fabricated materials have exhibited superior resistance to neutron irradiation examined in JMTR up to  $1.14 \times 10^{24}$  n/m<sup>2</sup> ( $E_n > 0.1$  MeV). The hardness increase of the materials after the irradiation is only 6.0 %, though much higher increase (73 %) is shown in the simultaneous irradiation of the standard SUS316L specimens. (Fig.1) The lower void swelling of the

ultra-fine grained materials than standard 316L is also found in 1 MeV electron irradiation, as shown in Fig.2.[1,2]

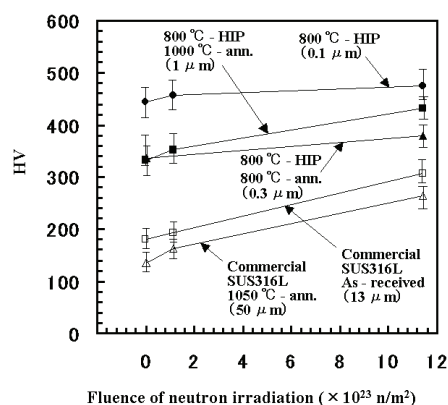


Fig.1 Vickers microhardness of the UFG316L-TiC as a function of neutron irradiation dose ( $E_n > 0.1$  MeV)

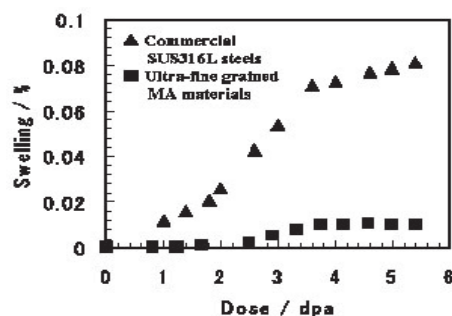


Fig.2 Void swelling of the UFG316L-TiC irradiated by 1 MeV electrons at 400°C

The ultra-fine grained W-1.1wt.% TiC materials with the grain size of 50 – 100 nm have been also obtained by the same fabrication method, and exhibited excellent resistance to the irradiation with neutrons and helium ions. [3,4]

### *Electronic state analysis of TiC in UFG materials*

In the fabrication of the UFG materials, small amount (about 1 wt.%) of TiC addition is found extremely effective to control the grain size, as described above

in both SUS316L and W. Although it is suggested that TiC nano particles act so as to pin the grain boundary during the fabrication process, what kind of interaction of TiC with matrix materials is concerned, and by what mechanism the pinning is governed are not clear.

We tried to measure the electronic states of Ti in the SUS316L-1.0wt.% TiC consolidates, as a preliminary step to elucidate the behavior of Ti or TiC in the fabrication process. XANES spectroscopy was performed at the end-station of the long undulator beamline BL9 in the NewSUBARU SR facility using a high resolution monochromator. The data were collected by a total electron yield (TEY) mode in which the sample current was measured when the photoelectron emitted by soft x-ray absorption. The values were normalized with a simultaneously recorded photoemission signal from a gold mesh, which indicates the soft x-ray intensity incident into the sample. At the present time, XANES spectra of Ti-L and C-K absorption edge of TiC in the SUS316L-1.0wt.% TiC consolidates were measured.

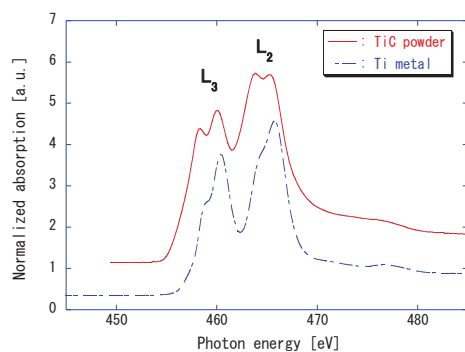


Fig.3. Ti-L<sub>2,3</sub> edge XANES spectra of Ti and TiC

Fig.3 shows Ti-L<sub>2,3</sub> absorption spectra for pure Ti (99.99 %) metal and TiC powders measured for reference before the XANES study for the fabricated SUS316L-TiC materials. A peak of Ti-L<sub>2</sub> (2p<sub>1/2</sub>) and L<sub>3</sub> (2p<sub>3/2</sub>) was observed at 465.9 eV and 461.4 eV, respectively, in the Ti specimen. On the other hand, each of L<sub>2</sub> and L<sub>3</sub> spectral line exhibits twin peak structure with an additional line with a separation of about 1.5 eV for the TiC powder specimen. The spectral variation is reflected by electronic structure due to different chemical state.

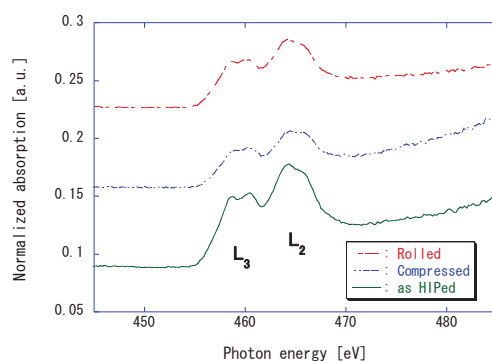


Fig.4. Ti-L<sub>2,3</sub> edge XANES spectra of UFG316L-TiC materials

Fig.4 shows XANES spectra of Ti-L<sub>2,3</sub> for the UFG SUS316L-1.0wt.% TiC specimens. Three kinds of materials, that is, as HIPed, high temperature compressed, and cold-rolled, are examined. The XANES spectra observed show characteristic twin peak structures for both L<sub>2</sub> and L<sub>3</sub>, which are in general agreement with the spectra shown in TiC powders. The NEXAFS spectra are decomposed for TiC powder and for SUS316L-TiC (as HIPed) as shown in Fig.5a and Fig.5b, respectively. The 2p spectra of TiC powder are separated to two peaks (463.4 eV and 465.5 eV) for L<sub>2</sub>, and other two peaks (458.1 eV and 460.0 eV) for L<sub>3</sub>. On the other hand, the 2p spectra of SUS316L-TiC (as HIPed) are separated to two peaks (463.9 eV and 465.9 eV) for L<sub>2</sub>, and other two peaks (458.4 eV and 460.3 eV) for L<sub>3</sub>. The lower energy peak in L<sub>2</sub> is due to t<sub>2g</sub> (π-bonding), and higher energy peak e<sub>g</sub> (σ-bonding). Likewise the lower energy peak in L<sub>3</sub> is due to t<sub>2g</sub>, and higher energy peak e<sub>g</sub>. The energies of the peaks in the UFG materials coincide with the corresponding peaks in the TiC powder. However, the e<sub>g</sub> peaks are smaller than the t<sub>2g</sub> peaks for both L<sub>2</sub> and L<sub>3</sub> in SUS316L-TiC compared with TiC powder. The real reason of this feature is not known at present. It may be concluded almost of all Ti atoms exist in the form of TiC in the UFG materials, but, in the same time, it is suggested other kind of precipitates exist with scarce concentration in the matrix.

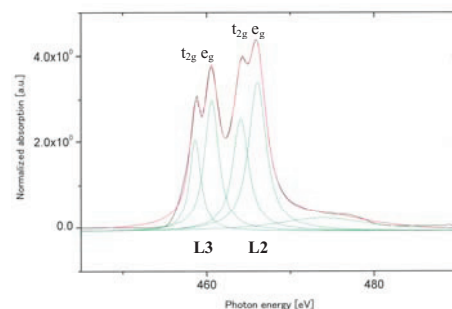


Fig.5a. Ti-L<sub>2,3</sub> NEXAFS for TiC powder

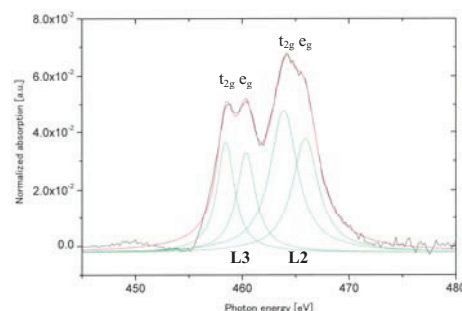


Fig.5b. Ti-L<sub>2,3</sub> NEXAFS for SUS316L-TiC

## References

- [1] Y. Z. Cheng et al, Material Science Forum, **426-432**, pp.1065-1070 (2003).
- [2] H. Matsuoka et al, Proc. ICAPP'05, Seoul, Korea (2005) paper 5687
- [3] H. Kurishita et al, Phys. Scr. T128 (2007) 76-80
- [4] H. Kurishita et al, IWSMT-8 (2006)

# Fabrication of High Aspect Ratio Microcoils

Daiji Noda, Masaru Setomoto, and Tadashi Hattori  
Laboratory of Advanced Science and Technology for Industry, University of Hyogo

## Abstract

Recently, there has been a growing requirement to reduce their size of actuators. Actuators, which held big volume and weight with a part of a product, have been required to reduce their size. However, the miniaturization of electromagnetic actuators has made little progress since it requires three-dimensional micro-fabrication processing and new technologies. We have focused on the fabrication of electromagnetic type microactuators that could be driven at low voltage and with high efficiency but it is well known that existing technologies for miniaturization of these devices are unsuitable because the allowable current path would be too small in microscopic applications. Therefore, we have fabricated a spiral microcoil with narrow pitch and high aspect ratio coil line structures using X-ray lithography and metallization techniques. We have fabricated spiral microcoils at a pitch of 60  $\mu\text{m}$ . Thus, an aspect ratio of coil lines was achieved about 5 as coil lines of 30  $\mu\text{m}$ . By using these techniques, microcoils with narrow pitch and high aspect ratio can be achieved, which are expected to yield high performance.

## Introduction

Recently, reductions in size and increases in sophistication have become desirable for many parts and devices. Actuators, which hold big volume and weight with a part of a product, have been required to reduce their size. However, the miniaturization of actuators has made little progress since it requires three-dimensional (3D) micro-fabrication processing and new technologies. On the other hand, LIGA (German acronym for Lithographite Galvanoformung and Abformung) process [1] can be fabricated nano and micro parts for devices. This technique is possible to make high aspect ratio structure fixed the narrow pitch of coil line and space. For the deep X-ray lithography involved in the LIGA process, we used the NewSUBARU Beamline 11 (BL11), which is a synchrotron radiation (SR) facility owned by our university. The x-ray exposure at BL11 was carried out with the workpiece held in a specially manufactured 'nine parts operation' exposure stage [2]. Thus, this stage makes it feasible to do 3D deep X-ray lithography for microcoils. Therefore, we have fabricated a spiral microcoil with high aspect structure on pipe surface for electromagnetic type microactuators using a 3D deep X-ray lithography and metallization techniques.

## Design of electromagnetic actuator

As the structure of the magnetic circuit, we used the type called *open frame solenoid*, which is open on the sides [3]. The material of electromagnetic core (fixed core and plunger) and shield parts (yoke) were used Permalloy that is a nickel iron alloy, because it has the largest permeability among soft magnetic metals. When the electrical supply to the coil is turned on, a magnetic flux forms in the gap, deforming the magnetic field and producing suction force on the plunger. If the aspect ratio is increased, the cross section area of coil lines is also increased

allowing a greater current path. Then, the magneto motive force is proportional to the squares of current path in the microcoil in this model [3]. This microactuator having the high aspect ratio of coil line is also expected a high performance in spite of miniature size.

## Fabrication process of microcoil

The surface of acrylic pipe for a screw thread structure, this is the coil part, has made using LIGA process. Figure 1 shows the fabrication process of microcoil. First, a cylindrical structure was formed on the surface of acrylic pipe by X-ray lithography. Next, copper was thinly deposited on pipe surface by sputtering in order to use as a seed layer in the electroforming. And, copper was formed into narrow pitch spiral structure by electroforming. Then, pipe surface was completely covered with copper film.

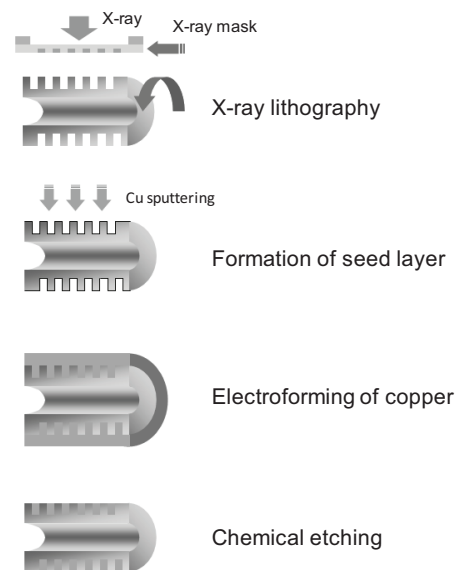
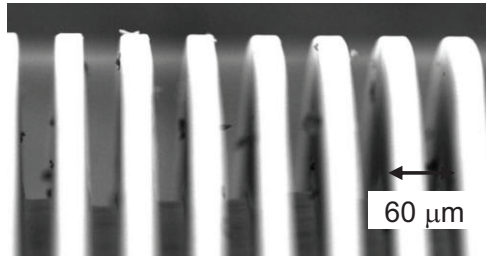


Fig. 1: Process flows of microcoil

Finally, forming Cu layer over the pipe surface was etched until the isotropic portions of wiring were exposed. We have fabricated a spiral microcoil at a pitch of 20  $\mu\text{m}$ , as shown in Fig. 2. Thus, an aspect ratio of coil lines was achieved about 5 as coil lines of 30  $\mu\text{m}$ . Following the seed layer deposition, we



**Fig. 2:** SEM image of coil lines on acrylic pipe with aspect ratio of 5

formed uniform copper electroplating for the current path of microcoils. Here, we proposed and introduced the new technique of reverse pulse current for electroforming in order to form high aspect ratio structures. In this result, it was able to be confirmed that plating developed to reach the bottom surface of the grooves, as shown in SEM image of Fig. 3. Finally, Isotropic copper etching was performed until the insulated portions of the wiring were exposed, as shown in Fig. 4.

#### Measurement of suction force

We have also fabricated a measurement system to measure the suction force of designed electro-

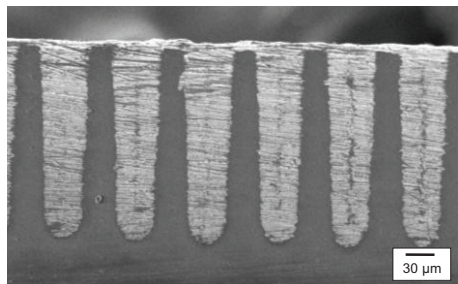


**Fig. 3:** SEM image of coil lines after copper electroforming

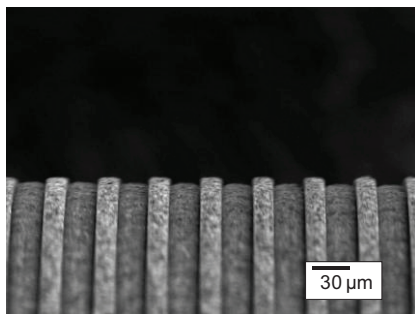


**Fig. 4:** SEM image of coil lines by isotropic copper etching

magnetic type actuators. This system is very simple structure and easy to exchange the coil part. The gap between plunger and fixed core was adjusted X-, Y-stage. The theoretical values by simulation and actual measurement results of suction force generated by the microcoil were compared, as shown in Fig. 5. These results are relatively in good agreement with theoretical values.

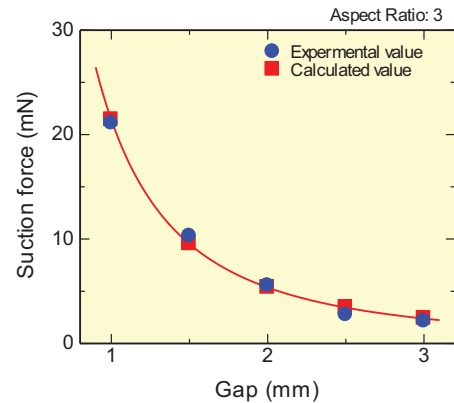


**Fig. 5:** Suction force comparison between measurement values and simulation results

#### Conclusions

We have fabricated microcoils with high aspect ratio using a 3D X-ray lithography and metallization technique in order to produce electromagnetic microactuators. We succeeded in producing a threaded structure with 30  $\mu\text{m}$  in coil lines width and about 5 in the maximum aspect ratio.

On the other hand, we developed a measurement system to measure a suction force. In measurement results, theoretical values by simulation values and actual measurement of suction force were compared. By using these techniques, microcoils with high aspect ratio can be achieved, which are expected to yield high performance. It is anticipated that high performance microcoils could also be manufactured, in spite of their miniature size.

#### Acknowledgment

This research is partially supported by the Grant-in-Aid for Scientific Research on Priority Area, No. 438, "Next-Generation Actuators Leading Breakthroughs", from the Ministry of Education, Culture, Sports, Science and Technology, Japan.

#### References

- [1] E. W. Becker, W. Ehrfeld, P. Hagmann, A. Maner, and D. Munchmeyer, *Microelectron. Eng.*, **4**, pp. 35-56 (1986).
- [2] H. Mekaru, S. Kusumi, N. Sato, M. Yamashita, O. Shimada, and T. Hattori, *Jpn. J. Appl. Phys.*, **43**, 6B, pp. 4036-4040 (2004).
- [3] Y. Matsumoto, M. Setomoto, D. Noda, and T. Hattori, *Microsyst. Technol.*, **14**, 9-11, pp. 1373-1379 (2008).

# Fabrication of X-ray Grating Using X-ray Lithography for X-ray Talbot Interferometry

Daiji Noda<sup>1</sup>, Naoki Takahashi<sup>1</sup>, Megumi Katori<sup>2</sup>, Yasuto Minamiyama<sup>2</sup>, and Tadashi Hattori<sup>1</sup>

<sup>1</sup>Laboratory of Advanced Science and Technology for Industry, University of Hyogo,

<sup>2</sup>Nanocreate Co., Ltd.

## Abstract

X-ray radiographic imaging technique is very important in medical, biological, inspection, material science, and so on. However, it is not enough to obtain clear X-ray images of samples with low absorbance materials, such as biological soft tissues. Then, we have used an X-ray phase imaging method of an X-ray Talbot interferometer. In this method, X-ray gratings were required to have narrow pitch and high aspect ratio structure. Therefore, we have developed and fabricated high aspect ratio X-ray gratings with a pitch of 5.3  $\mu\text{m}$ , a height of 30  $\mu\text{m}$ , and a large effective area of 60 mm  $\times$  60 mm using X-ray lithography and narrow electroforming technique. In this paper, we discuss the fabrication process of new X-ray mask and results of X-ray gratings of X-ray lithography technique.

## Introduction

X-ray radiographic imaging technique is very important in medical, biological, inspection, material science, and so on. However, it is not enough to obtain clear X-ray images of samples with low absorbance materials, such as biological soft tissues. On the other hand, several methods for generating radiographic contrast from the information of X-ray phase shift have been investigated. It is improvement in the high sensitivity by about 1000 times higher than by conventional absorption contrast. Numerous researchers have studied a variety of methods of phase imaging [1,2]. X-ray Talbot interferometer (XTI) is one of the methods of X-ray phase imaging [1]. In order to use 10-40 keV X-ray irradiation, the Au thickness of absorptive material must be over 20  $\mu\text{m}$ . But, it is not straightforward to make this structure with high aspect ratio by conventional techniques. Then, we have tried in fabricating such X-ray gratings particularly with a large area using X-ray lithography technique.

## Fabrication of X-ray mask

The conventional X-ray mask fabrication process was used on Si wafer [3]. In this case, we have used SU-8 as membrane because of large effective area X-ray mask. Therefore, X-ray masks comprising a resin membrane have the disadvantage that, after several cycles of X-ray exposure, they crease and sag due to X-ray-derived heat. As a substitute for the conventional resin membrane, we proposed to fabricate a new X-ray mask using a carbon wafer membrane that has an extremely small thermal expansion coefficient and is easy to process.

Figure 1 shows fabrication process using carbon wafer for membrane material. The fabrication process consists of three steps: (a) depositing a seed layer on the carbon wafer, (b) applying resist over the seed layer to perform patterning by irradiation with UV and development, (c) forming an X-ray absorber, i.e. an Au film, by electrolytic plating. We succeeded

in making new X-ray mask with pitch pattern of 5.3  $\mu\text{m}$  and large effective area of 60  $\times$  60 mm<sup>2</sup>, as shown in Fig. 2. In contrast to conventional silicon substrates, the newly devised mask fabrication process does not require further membrane application, frame adhesion or substrate etching. Thus, this is very simple process.

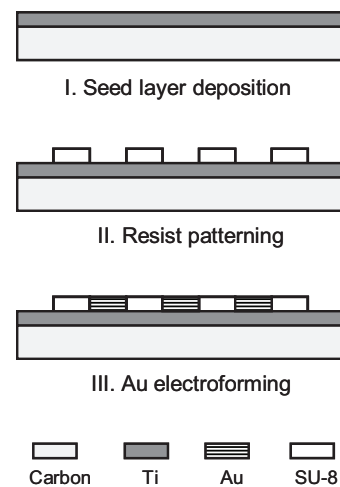


Fig. 1: New fabrication process of X-ray mask

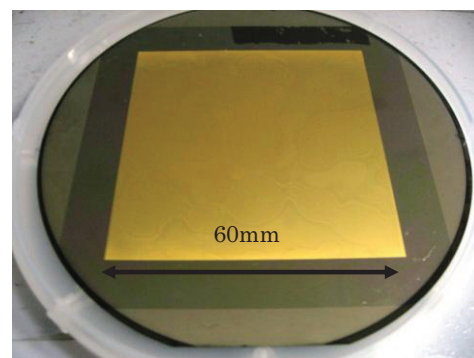


Fig. 2: Picture of carbon X-ray mask

### Fabrication of X-ray grating

X-ray lithography using synchrotron radiation has been utilized for 2.5-dimensional applications on flat substrate. Therefore, we took advantage of this technology to fabricate a high aspect ratio structure required for X-ray gratings with a pitch of several micrometers. For X-ray lithography, we used NewSUBARU beamlines 2, which is the synchrotron radiation facility owned by our university [4]. The beamline 2 has a potential of large area patterning across an A4-size area with a highly uniform pattern thickness.

A target specification of the X-ray grating was 5.3  $\mu\text{m}$  pitch pattern and large effective area of  $60 \times 60 \text{ mm}^2$ . For the deep X-ray lithography, we used a negative photo-resist SU-8. This SU-8 was originally designed for UV lithography. However it could also be used in deep X-ray lithography of high accuracy and high aspect ratio pattern. The pattern quickly collapses when the rinse solution is dried in the development and washing process. In order to solve this problem, we confirmed that line width of a provided cash register strike structure body became big with increase of an exposure a membrane came to be formed overexposure by the space top surface of line & space, as shown in Fig. 3. The X-ray grating was completed by gilding the resist structure of X-ray grating. And, we removed top surface layer using  $\text{O}_2$  plasma, as shown in Fig. 4.

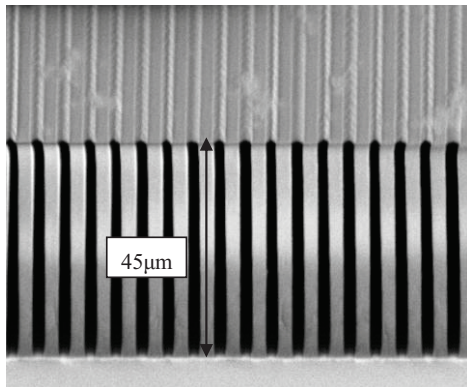


Fig. 3: SEM image of narrow pitch structure with top surface layer

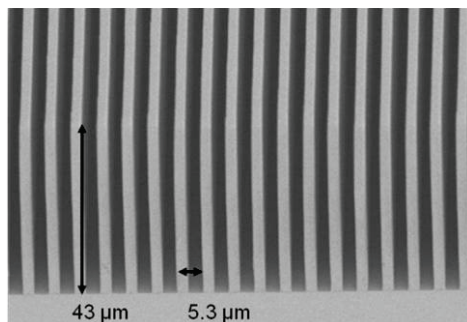


Fig. 4: SEM image of narrow pitch structure without top surface layer

Au absorbing part for the X-ray grating was formed by electroforming. In electroforming, chromium was used as seed film. A non-cyanic based solution was used for Au electroforming. From these results, the designed pitch of 5.3  $\mu\text{m}$  and height of about 40  $\mu\text{m}$  of X-ray grating are realized, as shown in Fig. 5.

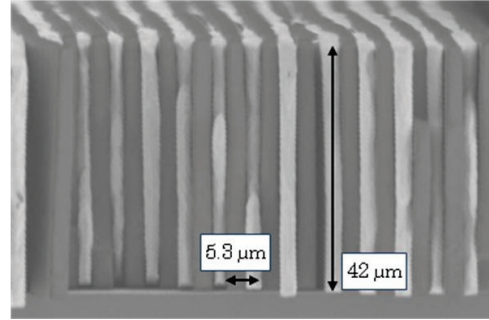


Fig. 5: SEM image of X-ray grating in cross section

### Conclusions

We have fabricated X-ray gratings having a pitch of 5.3  $\mu\text{m}$  and a large effective area of  $60 \times 60 \text{ mm}^2$  for X-ray Talbot interferometry. We were new and devised that we used a carbon wafer as membrane materials of X-ray mask was used to break off a problem by the heat transformation of the membrane which happened at the time of X-rays exposure. To make a higher aspect ratio X-ray grating, we developed the fabrication process composed of X-ray lithography and micro electroforming method. In X-ray lithography, sticking was observed because of surface tension. Therefore, we formed on top surface layer by overexposure. In this result, the resist structure with high aspect ratio and narrow pitch was obtained without surface tension in large area. After Au electroforming, large area and narrow pitch X-ray grating could be fabricated.

This result suggests that XTI is a novel and simple method for phase sensitive X-ray radiography, and promising method for many imaging applications.

### Acknowledgment

This research was supported by the research project “Development of Systems and Technology for Advanced Measurement and Analysis” from the Japan Science and Technology Agency (JST).

### References

- [1] A. Momose, Jpn. J. Appl. Phys., **44**, 9A, pp. 6355-6367 (2005).
- [2] C. David, B. Nöhammer, H. H. Solak and E. Ziegler, Appl. Phys. Lett., **81**, pp. 3287-3289 (2002).
- [3] D. Noda, M. Tanaka, K. Shimada, and T. Hattori, Jpn. J. Appl. Phys., **46**, 2, pp. 849- 851 (2007).
- [4] Y. Utsumi, T. Kishimoto, T. Hattori, and H. Hara, Microsyst. Technol., **13**, 5-6, pp. 417-423 (2007).

# Fabrication of High Hardness Ni Mold with Electroless Ni-B Thin Layer

Yoshitaka Sawa<sup>1</sup>, Kenji Yamashita<sup>2</sup>, Satoshi Nishida<sup>2</sup>, Daiji Noda<sup>3</sup>, and Tadashi Hattori<sup>3</sup>

<sup>1</sup>Sawa Plating Co., Ltd., <sup>2</sup>Nanocreate Co., Ltd.,

<sup>3</sup>Laboratory of Advanced Science and Technology for Industry, University of Hyogo

## Abstract

The nickel electroforming method using a high-concentration nickel sulfamate bath is commonly used to fabricate micro metal molds in the LIGA process; however, this method does not produce micro metal molds of sufficient hardness. In this research, we used a nickel-boron (Ni-B) electroless alloy plating method to obtain a hard nickel plated film having hardness of 832 Hv. It was also ascertained that Ni-B electroless alloy plated film retains its high hardness even during heat treatment in conditions of 250 °C for 1 hour. To deal with the high stresses developed in high-hardness plated films, we proposed double-layer nickel electroforming. This method is covered and used on conventional nickel electroforming layer by high hardness micro mold. High hardness micro metal mold using double-layer was fabricated by nickel electroforming and Ni-B electroless alloy plating method.

## Introduction

Recently, strong demand for the sophistication, downsizing and intensified integration of systems used in such cutting-edge areas industries as advanced information communications, medical care, bioscience, environment and energy has been sharply accelerating microsystem applications. In connection with this market demand, a manufacturing method based on transfer technology using micro metal molds has recently been in the spotlight. In particular, the LIGA (acronym for the German words Lithographie, Galvanoformung, and Abformung) process, based on exposure technologies using ultraviolet (UV) rays or synchrotron radiation (SR), is receiving attention. In the LIGA process, a master of the mold that will be formed into a three-dimensional structure is fabricated by lithography technology, and the master mold is then used to fabricate the micro metal mold by electroforming. This micro metal mold is then used for the molding operation.

The mainstream method for manufacturing micro metal molds using the LIGA process [1] is based on the nickel electroforming method. Because Ni electroforming uses electrolytic deposition depending on the Ni electroforming conditions during micro mold creation, a camber can occur on the plated film due to electrode position stress, rendering the micro mold unsuitable for use in making molds. However, the Ni electroforming layer prepared using this additive-free bath exhibits a low surface hardness value of approximately 200 Hv, which is not sufficiently high, since the injection mold hardness requirement is approximately 400 Hv or more, in common practice.

Suggested ways of improving the Ni electroforming layer hardness are to introduce additives into the plating bath to downsize the crystal grains in the electroforming film, and Ni-based alloy plating based on a eutectic process involving phosphorus, boron or

other elements. Numerous reports are available on improving the mechanical properties of Ni electroforming film. In this study, not all the 4-mm-thick micro metal molds were created using hard Ni plated film; we used double-layer Ni plating to form thin membranes of hard Ni plating as a film to cover the camber-free surface of an existing Ni micro mold, in an attempt to make a micro mold that exhibits minimum camber, yet has high mold surface hardness.

## Investigation of plating bath

We investigated Ni plating baths that can be used to produce the high-hardness Ni plating layer. In this study, we examined Ni-alloy-based plating baths of three types: commonly known nickel-phosphorus (Ni-P) electroless alloy plating, Ni-P alloy electroforming and nickel-boron (Ni-B) electroless alloy plating. Figure 1 shows a SEM image of the mold master after Ni-B electroless alloy plating (bath temperature: 60 °C). The mold master was made under the same conditions as Ni-P electroless alloy plating. Wrinkles creases did not develop on the photoresist structure side of the Ni-B electroless alloy plating layer. The plating temperature of the Ni-P electroless alloy plating bath, which can be as high as

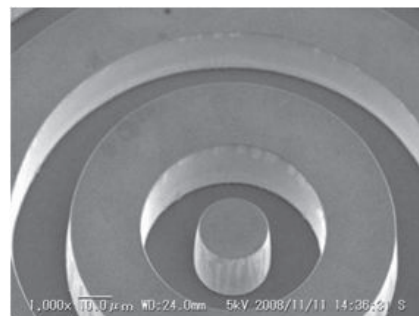


*Fig. 1: SEM image of Ni-B electroless plating*

90 °C, was considered responsible for the development of wrinkle creases on the plating layer. In response to this problem, this study examined use of a Ni-B electroless alloy plating layer to produce a hard Ni plating layer, since that plating process enabled a lower bath temperature. We assessed this layer mechanical property as a metal mold covering layer.

### Results and discussions

The Ni-B electroless alloy plated film was assessed by internal stress, surface hardness, and abrasion examination test. Test samples of approximately 40 μm thick plated film, deposited from the 50 and 60 °C baths, were used.

Figure 2 shows the results of the hardness measurement of Ni-B electroless alloy plated film. The hardness of the plated film deposited from the plating bath at a temperature of 50 °C was 808 Hv and that from the plating bath at a temperature of 60 °C was 832 Hv. The Ni-B electroless alloy plated film did not exhibit any reduction in hardness as a result of heat treatment below 300 °C. The heat treatment at 300 °C yielded hardness values of 904 Hv (for bath temperature of 50 °C) and 960 Hv (for bath temperature of 60 °C), both values being higher than that obtained immediately after deposition without heat treatment.

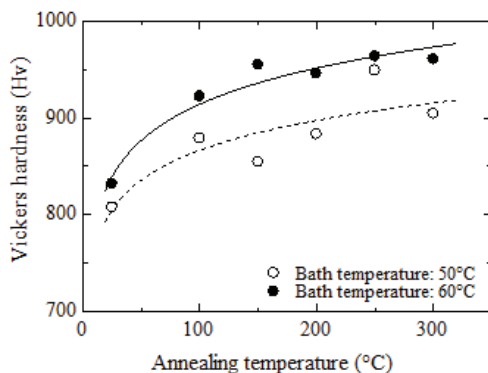


Fig. 2: Measurement results of Vickers hardness

### Fabrication of high hardness micro mold

We prepared a Ni micro mold using the double-layer plating method, which combines a hard Ni plated film, with mold covering layer composed of a Ni-B electroless alloy plated film, and a Ni electroforming layer produced in an additive-free bath. In the present study we used a light guide plate pattern with fine reflecting protrusions [2].

We used a Ni-B electroless alloy plating bath at a temperature of 60 °C to deposit a hard Ni plated film approximately 1 μm thick on this mold master. The surface of the hard Ni plated film, deposited before electroforming in an additive-free bath, was soaked in an organic degreasing agent for one minute as pretreatment, and then soaked in a 10% sulfuric acid

solution for one minute as surface activation treatment. This was followed by electroforming in an additive-free bath to enable deposition of a Ni electroforming layer to be 4 mm thick. Figure 3 shows SEM images of the Ni electroforming mold we prepared and of the truncated-cone-shaped reflecting protrusions of the light guide plate. Also shown are SEM images of a cross section of the truncated-cone-shaped reflecting protrusions.

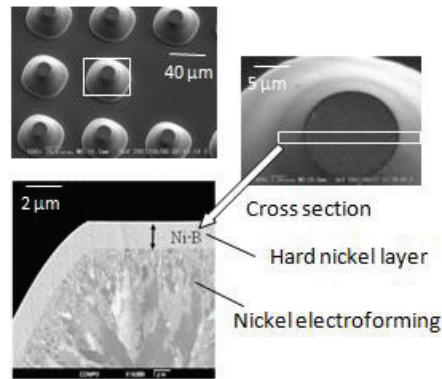


Fig. 3: SEM image of fabricated Ni micro mold with Ni-B double layer

### Conclusions

We have studied electroforming molds based on the LIGA process as a technology for manufacturing 3D fine micro-structures. Since nickel electroforming molds fabricated using an additive-free bath do not meet the hardness requirement associated with injection molding, we studied methods of increasing hardness by means of alloy plating. Thanks to the plated film deposited from the Ni-B electroless alloy plating solution, we successfully obtained a hard plated film with a hardness of 800 Hv or more. These results show that we succeeded in producing double-layer plating consisting of a hard plated film and electroformed film in an additive-free bath, verifying that the hard Ni plated film that served as a mold covering layer covered the entire mold pattern, and in successfully fabricating molds that accurately transfer mold master patterns prepared by UV lithography.

Furthermore, we will apply the current technology to large electroformed molds, with the aim of establishing a process for making large-area micro metal molds.

### References

- [1] E. W. Becker, W. Ehrfeld, P. Hagemann, A. Maner, and D. Munchmeyer, *Microelectron. Eng.*, Vol. 4, pp. 35-56 (1986)
- [2] T. Tanaka, T. Nomura, Y. Funabiki, T. Kitadani, K. Idei, K. Yamashita, D. Noda, and T. Hattori, *Proc. 2006 IEEE Int. Sympo. on Micro-Nano Mechatronics and Human Science*, Nagoya, Japan, pp. 480-485 (2006).

# Fabrication of Light Guide Plate for Ultraviolet Range

Yuta Okayama<sup>1</sup>, Takaya Fujimoto<sup>1</sup>, Kenji Yamashita<sup>1</sup>, Satoshi Nishida<sup>2</sup>, Yoshitaka Sawa<sup>3</sup>,  
Daiji Noda<sup>1</sup>, and Tadashi Hattori<sup>1</sup>

<sup>1</sup>Laboratory of Advanced Science and Technology for Industry, University of Hyogo,

<sup>2</sup>Nanocreate Co., Ltd., <sup>3</sup>Sawa Plating Co., Ltd.

## Abstract

The light guide plate, as part of the backlight unit in a cellular phone or liquid crystal display, has evolved to meet market demands for low power consumption, high-luminance and high-quality displays. Along with the advance of the light guide plate, light emitting diodes have undergone development as light source for light guide plates. In recent years, the ultraviolet light are used as a source of light of the air cleaner, and it is used as a source of light to activate the titanium dioxide which is photocatalyst. However, common ultraviolet light sources are either line or point light sources. Therefore, we studies surface illuminators that incorporate diffusers in the visible light range. Applying our existing technology, we constructed an unprecedented ultraviolet surface illuminator and measured it using a photocatalyst.

## Introduction

In recent years, liquid crystal displays (LCDs) have come to be widely used in cellular phones and TV sets. This popularity has led to growing demand for a higher performance light guide plate as an LCD component. In the light guide plate, light is guided from a light emitting diode (LED) or other point light source to desired locations via total internal reflection rendered by index of refraction differential between air and diffuser material. The light in light guide plate tears a total reflection condition by reflecting in an internal projection (dot) and irradiates the surface [1]. The light guide plate, converts point light source to surface illumination. Figure 1 shows a schematic diagram of a light guide plate. One advantage of the light guide plate is its efficient use of light through the conversion of point light source to surface illumination. To apply our technology to surface illuminators using ultraviolet (UV) light, which have begun to be used recently in home air cleaners and the like, we have embarked on fabricating a light guide plate specifically designed for UV-LEDs.

In this study, optimal bump shape and allocation were derived for UV surface illuminators. Indeed, a light guide plate was fabricated using the molding technology.

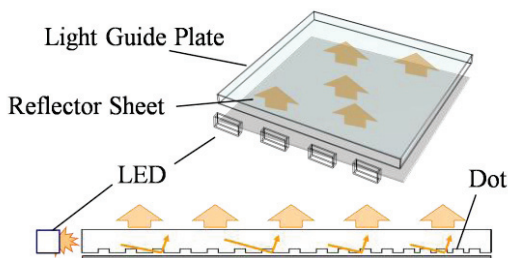


Fig. 1: Schematic diagram of light guide plate

## Design of light guide plate by simulation

The reflection dot of the bottom of light guide plate influences irradiation of the light. Therefore, in

achieving uniform surface illumination with a light guide plate alone, the shape and allocation of reflective bumps are of much importance. Optimization of bump shape and allocation enables the creation of a light guide plate for uniform illumination. First, the optimal bump shape was obtained. The bump shape was transformed from a cylindrical column to a truncated cone, using fixed dimensions of 30  $\mu\text{m}$  height and 52  $\mu\text{m}$  base diameter. Comparisons were made among cylindrical column, from 50 to 80 degree tapered truncated cones, taking heed of visible-light diffuser conditions that the laboratory has studied. Simulation results revealed that strong light was emitted near 60 to 70 degree taper angles, as in the visible light range.

In the next step, optimal bump allocation was derived for the 70 degrees taper angle. In this study, the light guide plate we fabricated had bumps in a 48 mm  $\times$  88 mm area on a 52 mm  $\times$  96 mm  $\times$  2.6 mm board. The optimal bump allocation was determined by thinning filled bumps, on the basis of simulation results. From simulation results, the fully uniform placement of bumps was obtained [3]. Before bump allocation optimization, output characteristics were such that the maximum value was 6.39  $\text{W}/\text{m}^2$  and the minimum value was 1.15  $\text{W}/\text{m}^2$ . After optimization, the maximum value was reduced to 3.23  $\text{W}/\text{m}^2$ , while the minimum value was increased to 1.82  $\text{W}/\text{m}^2$ . The uniformity ratio, which is an indicator of the degree of illumination uniformity, improved from 35 % to 91 %.

## Fabrication of light guide plate

Since the shape was micro sized, the UV-LIGA process was used to fabricate an UV light guide plate, designed as above. As regards the master pattern, a structure was created by lithography, painting with resist that is photosensitive resin wafer. Next, copper was sputtered onto the surfaces of the created master pattern. A mold was then fabricated through Ni electroforming. Consequently, the Ni thickness was set at approximately 4 mm for electroforming. Lastly,

the light guide plate was produced through injection molding using the mold as a cavity [3]. The achieved bump shape was obtained at 10  $\mu\text{m}$  in top diameter, 52  $\mu\text{m}$  in base diameter, 70 degrees in taper angle and 30  $\mu\text{m}$  in height.

### Evaluation of light guide plate

Using a photodiode, the emission characteristics of the fabricated light guide plate were measured to verify that the light guide plate would provide uniform illumination. Energy values were calculated from the spectral response characteristics of the photodiode and the wavelength of the light emitted by the LED. The energy distribution was obtained as closely simulation result, as shown in Fig. 2. In the simulation, the maximum and minimum values were 3.23  $\text{W}/\text{m}^2$  and 1.82  $\text{W}/\text{m}^2$ , respectively, while the molded light guide plate provided maximum and minimum values of 4.25  $\text{W}/\text{m}^2$  and 3.10  $\text{W}/\text{m}^2$ , respectively. The maximum value increase from the simulation results was probably due to some entry angle deviation that occurred at LED mounting. However, the higher minimum value suggests that the fabricated light guide plate was better than the simulated one used for analysis.

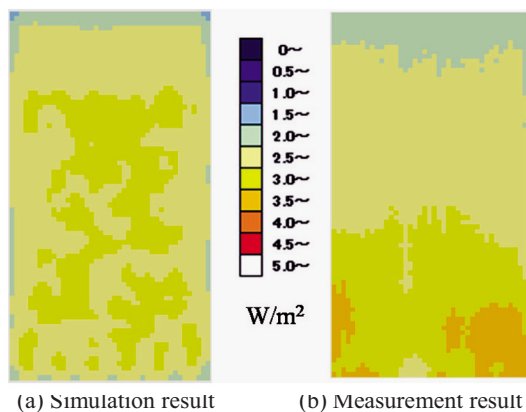


Fig. 2: Energy distribution of light guide plate

### Measurement of photocatalyst

In light of such trends, using the light guide plate fabricated in this study we conducted an experiment involving the processing of toluene gas discharged during printing, or from adhesives. We performed what the repetition experiment that we used an active carbon and photocatalyst for, experiment by the change of the irradiation energy and experiment only by photocatalyst. Deodorization measurements using a photocatalyst are conducted either dynamically, by incorporating an external force to generate air flow, or statically, by using a closed space allowing no air flow. In our study, the experiment of the latter type was in a static environment.

In the first experiment, 100 ppm of toluene gas was injected to the container, and the toluene gas concentration was measured 60 minutes later. On the basis of concentration measurement results, toluene

gas was again added so as to achieve 100 ppm. This cycle was repeated several times. Figure 3 shows experiment results. Since no UV light was irradiated in the initial period, the activated carbon came close to saturation after several cycles, diminishing in toluene-processing capacity. However, after a few hours of UV irradiation, the processing capacity of photocatalyst and activated carbon recovered from approximately 50 % to approximately 90 %.

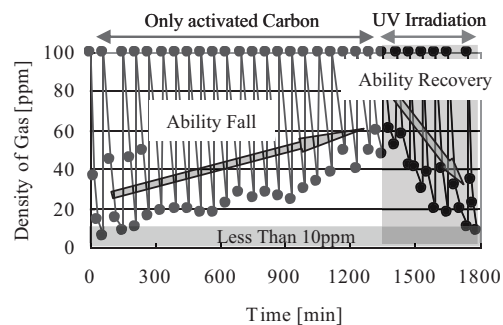


Fig. 3: Results of deodorization measurement for toluene gas

### Conclusions

We fabricated an unprecedented UV surface illuminator and assessed its capacity as a light source for reactivating photocatalysts. Bump shape and allocation for uniform illumination of UV light were derived through simulation, achieving uniformity ratio improvement from 35 % to 91 %. The light guide plate for UV light was fabricated using UV-LIGA process. The fabricated light guide plate presented performance comparable to simulation results, with a minimum value exceeding analysis results, though the uniformity ratio did not reach the simulation results.

We intend to conduct processing measurements similar to the toluene gas decomposition experiment, and to closely assess the relationships between energy value and photocatalyst processing capacity. Moreover, for additional increases in emitted energy value, we will review the UV-light diffuser design through simulation.

### References

- [1] T. Tanaka, T. Nomura, Y. Funabiki, T. Kitadani, K. Idei, K. Yamashita, D. Noda, and T. Hattori, Proc. of the 2006 IEEE Int. Symp. on Micro-Nano Mechatronics and Human Science, Nagoya, Japan, pp. 480-485 (2006).
- [2] Y. Sawa, T. Tanaka, T. Kitadani, H. Ueno, Y. Itoigawa, K. Yamashita, D. Noda, and T. Hattori, Microsyst. Technol., 14, pp. 1559-1565 (2008).
- [3] Y. Okayama, K. Yamashita, D. Noda, and T. Hattori, Proc. the 2008 IEEE Int. Symp. on Micro-Nano Mechatronics and Human Science, Nagoya, Japan, pp. 408-413 (2008).

# Fabrication of Micro Capacitive Inclination Sensor by Resin Molding Method

Hiroaki Miyake<sup>1</sup>, Kazufumi Nishimoto<sup>1</sup>, Satoshi Nishida<sup>2</sup>, Daiji Noda<sup>1</sup>, and Tadashi Hattori<sup>1</sup>

<sup>1</sup>Laboratory of Advanced Science and Technology for Industry, University of Hyogo,

<sup>2</sup>Nanocreate Co., Ltd.

## Abstract

In various leading-edge technology industries, there is a growing need to reduce the weight and increase the energy saving performance of various electronics products. It is now under development to enable the production of less expensive MEMS devices for low costly production technology. Then, the LIGA process is a technology, which is considered to be suited for mass production, enabling the creation of a microstructure by transferring a pattern from this master mold to a resin. In this study, we fabricated a micro capacitive inclination sensor by using combination of a resin forming method and a mold. We could fabricate and successfully package a resin sensor by molding technique that can be made at low cost production. If a small inclination sensor, having a size of several millimeters, could be made using a resin forming method, production costs could be substantially reduced compared to sensors made with the conventional MEMS process.

## Introduction

In various leading-edge technology industries, there is a growing need to reduce the weight and increase the energy saving performance of various electronics products. Although MEMS (Micro Electro Mechanical Systems) technology [1] is not suited for mass-produced sensors since silicon is brittle and expensive and its processing is complicated, involving many processes. On the other hand, the LIGA process is a technology, which is considered to be suited for mass production, enabling the creation of a microstructure by transferring a pattern from this master mold to a resin.

In this study, we fabricated a micro capacitive inclination sensor [2] by using combination of a resin forming method and a mold. If a small inclination sensor, having a size of several millimeters, can be made using a resin forming method, production costs can be substantially reduced compared to sensors made with the conventional MEMS process. Since the dimensions of its sensing region are  $7 \times 7 \times 3$  mm<sup>3</sup>, which are much smaller than the dimensions of conventional sensors, this inclination sensor is expected to be widely used in the field where efficient and reliable attitude control is a primary factor to be considered.

## Micro capacitive inclination sensor

This is working principle of a micro capacitive inclination sensor that two semicircular opposing electrodes are set above one circular common electrode [2]. Therefore, two capacitors are formed. The region between the opposing electrodes and common electrode is half filled with oil. The oil inside maintains its level due to gravity when the sensor inclines, so that the amount of oil changes in each capacitor. As a result, the capacitances change, and the angle of inclination of the sensor can be detected, based on this change in the capacitance

values. Capacitance change of the capacitor on the one side of the electrodes  $\Delta C$  is expressed the proportional inclination angle  $\theta$  [2].

## Fabrication process of sensor

Figure 1 shows the fabrication process for the micro capacitive inclination sensor. In the first step, a mold to be used for forming was prepared by UV (ultraviolet) lithography and Ni electroforming (Figs. 1(A) to (F)). The spacer part of this mold was transferred to a resin by hot embossing molding (Figs. 1(G) and (H)) [3]. The common electrode was formed on a structure having projections and recesses (Figs. 1(I) to (M)). The opposing electrodes, formed by transferring the pattern, were then attached to the common electrode, oil was injected, and the injection port was then sealed to complete the fabrication of the inclination sensor (Figs. 1(N) to (P)). Specifically, an electrode film was formed, only at the recesses on the slit-structured surface having projections and recesses. A patterning method using a mask would be a viable method for forming an electrode at a specified position. Using this method, however, it is very difficult to bring a mask into proper alignment with a non-flat surface; this method also has a drawback in respect of cost. In the case of the process that is the subject of this paper, a significant cost reduction is possible, since an electrode film can be formed without using a mask.

## Formation of electrode on resin molding

The inclination sensor comprises two electrodes, i.e., a common electrode and opposing electrode, to form a capacitor. Figure 2 shows images of the cross section of a molding on which resist had been coated, using a spin/spray coating system. As shown in this

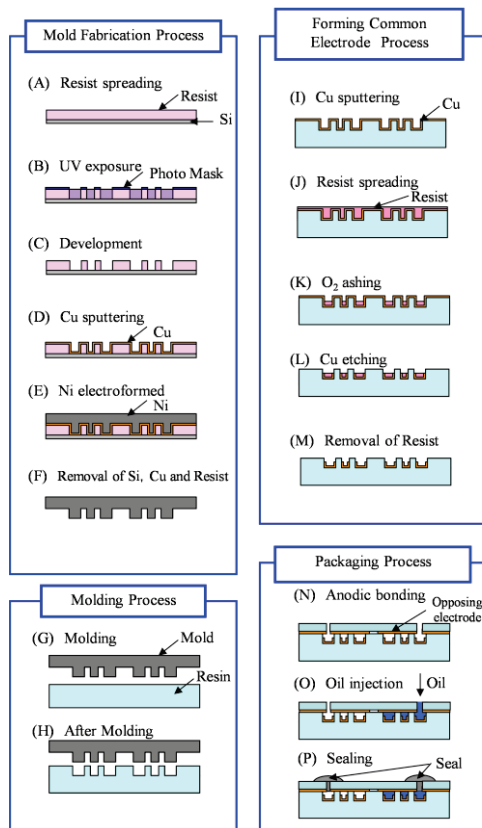


**Fig. 1:** Fabrication process for sensor using molding

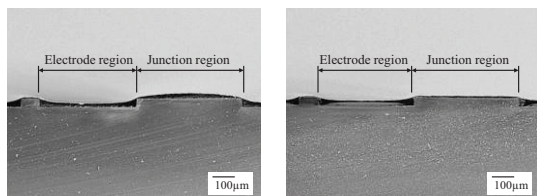


**Fig. 2:** SEM image of pattern in cross section

image, resist smoothly followed the projections and recesses in the pattern. After resist coating, the thickness of the resist film on the electrode region was the same at that of the film on the junction region. Therefore, if  $O_2$  ashing were performed on a molding having a uniform thickness of resist, resist could not remain only in the recess in the electrode region. Therefore, we placed a resist-coated sample in a container filled with solvent vapor so that resist, exposed to solvent vapor, would melt and be planarized. As is evident from Fig. 2b, the resist coating on the junction part was very thin, compared with a sample, shown in Fig. 2a, which had not yet been planar. Cu electrode was thus formed successfully, only in the recess in the structure, using the proposed new process.

We successfully fabricated a micro inclination sensor as a molded product [4]. In future, we will carry out wiring to complete this inclination sensor,

and then conduct performance evaluations, as shown in Fig. 3.

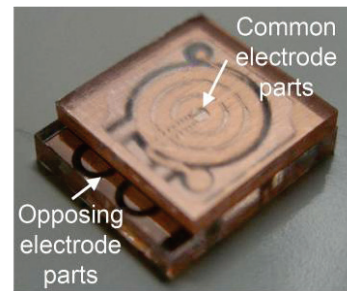


**Fig. 3:** Picture of completed sensor

### Conclusions

Based on low cost molding techniques suited for mass production, we have fabricated a micro capacitive inclination sensor by using a resin molded component. We prepared a mold by UV lithography and Ni electroforming. In addition, using the hot embossing molding technique, we fabricated a structure in which our pre-designed projections and recesses were realized.

We proposed a new process for forming electrodes, only in the recesses in a fabricated resin molded component, without using a mask, and successfully fabricated the common electrode of an inclination sensor. The process proposed and established in this study requires no alignment and makes possible a substantial cost reduction. Although we faced a difficult task of planarizing resist in this process, we used solvent vapor for planarization with satisfactory results. We successfully fabricated a micro inclination sensor as a molded product. In future, we will carry out wiring to complete this inclination sensor, and then conduct performance evaluations.

The techniques using resin-molded parts have the potential to be applied to the production of, not only inclination sensors, such as the one fabricated in this study, but also MEMS devices. If the techniques using resin-molded parts are introduced to the mass-production of MEMS devices, including sensors, at low cost, the range of their applications will further expand to new areas of technology and industry.

### References

- [1] F. Kohsaka, J. Liang, T. Matsuo, and T. Ueda, *IEEJ Trans. SM*, **127**, 10, pp. 431-436 (2007).
- [2] H. Ueda, H. Ueno, K. Itoigawa, and T. Hattori, *IEEJ Trans. SM*, **126**, 12, pp. 637-642 (2006).
- [3] N. Ishizawa, K. Idei, T. Kimura, D. Noda, and T. Hattori, *Microsyst. Technol.*, **14**, 9-11, pp. 1381-1388 (2008).
- [4] H. Miyake, K. Nishimoto, H. Ueda, H. Ueno, K. Itoigawa, S. Nishida, D. Noda, and T. Hattori, *IEEJ Trans. SM*, **129**, 9, pp. 283-288 (2009).

# **List of Publications**



# List of publications

## (1) Papers

1. K. Imasaki, D. Li, S. Miyamoto, S. Amano T. Mochizuki, and Y. Asano  
**"Gamma-ray Beam Transmutation"**  
Energy Conversion and Management **49** , pp.1922-1927 (2008).
2. Shuji Miyamoto  
**"Laser Compton Gamma-ray Generation"**  
ICFA Panel on Advanced and Novel Accelerators Newsletter, Dec. 2009, pp.17-22(2009).
3. D. Li, K. Imasaki, S. Miyamoto, K. Horikawa, S. Amano, and T. Mochizuki  
**"Positron generation through laser Compton scattering gamma ray"**  
Appl. Phys. Lett., **94**, 091112, March (2009).
4. Akihisa Nagano, Sho Amano, Shuji Miyamoto, Takayasu Mochizuki  
**"Extream Ultraviolet Source Using Laser-Produced Li Plasma"**  
EEJ Transactions on Electronics, Information and Systems, C, vol. **129**, No.2, pp. 249- 252 (2009) (Japanese).
5. Sho Amano, Ken Horikawa, Kazuki Ishihara, Shuji Miyamoto, Takehito Hayakawa, Toshiyuki Shizuma, and Takayasu Mochizuki  
**"Several-MeV  $\gamma$ -ray generation in NewSUBARU by laser Compton backscattering"**  
Nuclear Instruments and Methods in Physics Research A, Vol. **602**, Issue 2, 21 April 2009, Pages 337-341(2009).
6. Akira Heya, Yasuyuki Takanashi, Sho Amano, Naoto Matsuo, Shuji Miyamoto, and Takayasu Mochizuki  
**"Effect of Laser Plasma X-ray Irradiation on Nucleation in Amorphous Silicon Film"**  
Japan. J. Appl. Phys., Vol. **48**, 050208 (2009).
7. Dazhi Li, Kazuo Imasaki, Ken Horikawa, Shuji Miyamoto, Sho Amano and Takayasu Mochizuki  
**"Iodine Transmutation through Laser Compton Scattering Gamma Rays"**  
J. Nuclear Science and Technology, Vo. **46**, No.8, pp.831-835(2009).
8. Yoshihiko Shoji  
**"Generating coherent THz radiation in electron storage rings using an ac sextupole magnet and a vertical kicker magnet"**  
Phys. Rev. ST Accel. Beams **13**, 060702 (2010).
9. Yoshihiko Shoji,  
**"Design of a Multi-Element Corrector Magnet for the Storage Ring NewSUBARU"**  
IEEE Transactions on Applied Superconductivity, Vol.**20**, No.3, pp.230-233 (2010).
10. Yoshihiko Shoji  
**"Transient bunch lengthening by a betatron motion along bending sections"**,  
Nuclear Instr.& Meth. in Physics Research A, in press (available online 10 Feb. 2010).
11. S. Amano, Y. Inaoka, H. Hiraishi, S. Miyamoto, T. Mochizuki  
**"Laser-plasma debris from a rotating cryogenic-solid-Xe target"**  
Rev.Sci.Instrum., Vol.**81**, 023104 (2010)
12. Mitsuyoshi Kishihara, Yoshiaki Ukita, Shigeaki Yamamoto, Isao Ohta, Yuichi Utsumi  
**"SR Direct Etching of PTFE and Its Application to Millimeter-Wave PTFE-Filled Waveguide"**  
IEEJ Transactions on Electronics, Information and Systems, **129**, 2, pp. 259-266 (2009).
13. Saki Kondo, Yoshiaki Ukita, Kuniyo Fujiwara, Yuichi Utsumi  
**"A Novel Micromixer with Three-Dimensionally Cross-Linked Capillary Array Structure Fabricated by**

***Deep X-ray Lithography***

IEEJ Transactions on Electronics, Information and Systems, **129**, 2, pp. 277-281 (2009).

14. Tsunamasa Saiki, Katsuhide Okada, Yuichi Utsumi  
***“Fabrication and Estimation of Novel Micro Liquid Rotor that Operates with Surface-Acoustic-Wave”***  
IEEJ Transactions on Electronics, Information and Systems, **129**, 2, 219-224 (2009).
15. Shigeaki Yamamoto, Yoshiaki Ukita, Kozo Mochiji, Yuichi Utsumi  
***“Microfabrication of Poly(tetrafluoroethylene) Using SR Direct Etching”***  
IEEJ Transactions on Electronics, Information and Systems, **129**, 2, 244-248 (2009).
16. Daisuke Fukuoka, Tomohiro Ikeda, Yuichi Utsumi  
***“Development of Multi-Analytes DNA Microchip by Using 3-D Nanoprototyping Fabrication Method”***  
IEEJ Transactions on Electronics, Information and Systems, **129**, 2, 272-276 (2009).
17. Akinobu Yamaguchi, Keiichi Motoi, Hideki Miyajima, Atsufumi Hirohata, Takehiro Yamaoka, Tsuyoshi Uchiyama, and Yuichi Utsumi  
***“Current manipulation of a vortex confined in a micron-sized Fe19Ni81 disk”***  
Applied Physics Letters, **95**, 122506-112508 (2009).
18. Yuichi Utsumi, Shigeaki Yamamoto, Tomoyuki Kuroki, and Masaaki Okubo  
***“Direct bonding of PFTF sheets assisted by synchrotron radiation induced surface modification”***  
Microsystem Technologies, **16**, 8-9, pp.1495-1500 (2010).
19. Yoshiaki Ukita, Saki Kondo, Chiwa Kataoka, Masahiro Takeo, Seiji Negoro, and Yuichi Utsumi  
***“Immunoassay using poly-tetrafluoroethylene microstructure in organic solvent”***  
Microsystem Technologies, **16**, 8-9, pp.1465-1470 (2010).
20. Tsunemasa Saiki, Katsuhide Okada and Yuichi Utsumi  
***“Micro liquid rotor operated by surface-acoustic-wave”***  
Microsystem Technologies, **16**, 8-9, pp.1589-1594 (2010).
21. Saki Kondo, Tsukasa Azeta, Yoshiaki Ukita, Yuichi Utsumi  
***“Vertical Liquid Transportation Through Capillary Bundle Structure Using Centrifugal Force”***  
Microsystem Technologies, **16**, 8-9, pp.1577-1580 (2010).
22. Yuichi Utsumi, (Invited paper)  
***“Proposal of 3D Micro prototyping Using Synchrotron Radiation and Its Application to Bio-Microsystems”***  
Service Robotics and Mechatronics (Springer), 7-14, (2010).
23. Akinobu Yamaguchi, Keiichi Motoi, Hideki Miyajima, Tsuyoshi Uchiyama, and Yuichi Utsumi  
***“Detection of Nonlinear Spin Dynamics in Artificial magnets Using Rectification of Planar Hall Effect”***  
Journal of the Magnetics Society of Japan , **34**, 73-77 (2010).
24. Tsuyoshi Uchiyama, Akinobu Yamaguchi, and Yuichi Utsumi  
***“Noise Characterization of Coil Detection Type Magnetic Field Sensor Utilizing Pulse Excitation Amorphous Wire Magneto-Impedance Element”***  
Journal of the Magnetics Society of Japan , **34**, 533-536 (2010).
25. Makoto Okada, Masayuki Iwasa, Ken-ichiro Nakamatsu, Kazuhiro Kanda, Yuichi Haruyama, and Shinji Matsui,  
***“Nanoimprinting using Release-agent-coated Resins”***  
Microelectronic Engineering, **86**, 673-675 (2009).
26. Makoto Okada, Masayuki Iwasa, Ken-ichiro Nakamatsu, Kazuhiro Kanda, Yuichi Haruyama, and Shinji Matsui,  
***“Durability of Antisticking Layer Against Heat in Nanoimprinting Evaluated using Scanning Probe Microscopy”***  
Microelectronic Engineering, **86**, 657-660 (2009).

27. Makoto Okada, Ken-ichiro Nakamatsu, Yuji Kang, Kanda Kanda, Yuichi Haruyama, and Shinji Matsui, **“Characteristics of Antisticking Layer Formed by  $\text{CHF}_3$  Plasma Irradiation for Nanoimprint Molds”** Jpn. J. Appl. Phys., **48**, 06FH15-1 – 06FH15-4 (2009).
28. Makoto Okada, Yuji Kang, Ken-ichiro Nakamatsu, Masayuki Iwasa, Kazuhiro Kanda, Yuichi. Haruyama, and Shinji Matsui, **“Characterization of Nanoimprint Resin and Antisticking Layer by Scanning Probe Microscopy”** J. Photopolym. Sci. Tech, **22**, 167-169 (2009).
29. Yuji Kang, Makoto Oakada, Ken-ichiro Nakamatsu, Kazuhiro Kanda, Yuichi Haruyama, and Shinji Matsui, **“Room-temperature nanoimprint using sol-gel ITO film”** J. Photopolym. Sci. Tech, **22**, 189-192 (2009).
30. Yuji Kang, Makoto Oakada, Ken-ichiro Nakamatsu, Kazuhiro Kanda, Yuichi Haruyama, and Shinji Matsui, **“Room-temperature nanoimprint using liquid-phase hydrogen silsesquioxane with PDMS mold”** J. Photopolym. Sci. Tech, **22**, 193-194 (2009).
31. Yuji Kang, Makoto Okada, Ken-ichiro Nakamatsu, Kazuhiro Kanda, Yuichi Haruyama, and Shinji Matsui, iroshi Hirohsima, **“UV irradiation effect on sol-gel indium tin oxide nanopatterns replicated by room-temperature nanoimprint”** J. Vac. Sci. Technol. B, **27(6)**, 2805-2809 (2009).
32. Kazuhiro Kanda, Jun-ya Igaki, Noriko Yamada, Reo Kometani, and Shinji Matsui **“Graphitization of thin films formed by focused-ion-beam chemical-vapor-deposition”** Diamond & Related Materials **18** (2009) 490-492.
33. Ken-ichiro Nakamatsu, Toshinari Ichihashi, Kazuhiro Kanda, Yuichi Haruyama, Takashi Kaito, and Shinji Matsui, **“Nanostructure Analysis of Nanosprings Fabricated by Focused-Ion-Beam Chemical Vapor Deposition”** Japanese Journal of Applied Physics **48** (2009) 105001.
34. Y. Haruyama, M. Tagawa, K. Yokota, and S. Matsui **“Photoemission Study of Hydrogenated Amorphous Carbon Thin Films as a Function of Annealing Temperature”** Jpn. J. Appl. Phys. Vol. **48**, 055505-3 (2009).
35. Y. Haruyama, T. Kitagawa, S. Matsui, N. Toyoda, and I. Yamada **“Photoelectron Spectroscopy Study of the Valence Band Region in Diamond-like Carbon Thin Films”** Jpn. J. Appl. Phys. Vol. **48**, 092301-4 (2009).
36. Keigo Koida and Masahito Niibe: **“Study on contamination of projection optics surface for extreme ultraviolet lithography”** Appl. Surf. Sci., **256**, 1171-1175 (2009).
37. Masahito Niibe and Keigo Koida: **“Competitive reaction of carbon deposition and oxidation on the surface of Mo/Si multilayer mirrors by EUV irradiation”** SPIE Vol. **7361**, 73610L-1-8 (2009).
38. Daiji Noda, Hiroshi Tsujii, Naoki Takahashi, and Tadashi Hattori, **“Fabrication of X-ray Grating Using X-ray Lithography Technique for X-ray Talbot Interferometer”** Journal of the Electrochemical Society, Vol. 156, No.5, pp. H299-H302, 2009
39. Yoshitaka Sawa, Kyo Tanabiki, Daiji Noda, and Tadashi Hattori, **“Fabrication of the 3 Dimension Resist “Microstructure Using X-ray Diffraction and Applying to LIGA Process”** Journal of Solid Mechanics and Materials Engineering, Vol. 3, No. 5, pp. 721-728, 2009
40. Yoshitaka Sawa, Kenji Yamashita, Takeshi Kitadani, Daiji Noda, and Tadashi Hattori, **“Development of High “Hardness Micro Metal Mold by Double Layered Electroforming”**

Journal of the Society of Plant Engineers Japan, Vol. **21**, No. 1, pp. 7-12, 2009

41. Hiroaki Miyake, Kazufumi Nishimoto, Hiroyasu Ueda, Hiroshi Ueno, Koichi Itoigawa, Satoshi Nishida, Daiji Noda, and Tadashi Hattori  
**"Fabrication of a Micro Capacitive Inclination Sensor by Resin Molding"**  
IEEJ Transaction on Sensors and Micromachines, Vol. **129**, No.9, pp. 283-288, 2009
42. Yoshitaka Sawa, Kenji Yamashita, Takeshi Kitadani, Daiji Noda, and Tadashi Hattori  
**"Fabrication of High Hardness Micro Metal Mold by Nickel-Boron Electroless Plating Method"**  
Journal of the Society of Plant Engineers Japan, Vol. **21**, No. 2, pp. 21-25, 2009
43. Daiji Noda, Kazufumi Nishimoto, Hiroaki Miyake, Satoshi Nishida, and Tadashi Hattori  
**"Fabrication of Micro Capacitive Inclination Sensor"**  
Journal of the Society of Plant Engineers Japan, Vol. **21**, No. 2, pp. 26-30, 2009
44. Kenji Yamashita, Yoshitaka Sawa, Daiji Noda, and Tadashi Hattori  
**"Fabrication of Ultraviolet Range Light Guide Plate and Applies to Photocatalyst Source of Light"**  
Journal of the Society of Plant Engineers Japan, Vol. **21**, No. 2, pp. 38-42, 2009
45. Teppei Kimura, Tomohiro Ishida, and Tadashi Hattori  
**"Mechanical Characteristics Evaluation of MEMS Probe"**  
Journal of the Society of Plant Engineers Japan, Vol. **21**, No. 2, pp. 49-53, 2009
46. Yoshitaka Sawa, Kenji Yamashita, Takeshi Kitadani, and Tadashi Hattori  
**"Fabrication of High Hardness Micro Metal Mold by Double Layer Nickel Electroforming"**  
Transactions of the Japan Society of Mechanical Engineers, Vol. **75**, No. 759, pp. 3076-3081, 2009
47. Tadashi Hattori  
**"Fabrication of Micro Structure Surface by Etching Method"**  
Journal of Japanese Society of Tribologists, Vol. **55**, No. 2, pp. 83-88, 2010

## (2) International Meetings

1. S.Miyamoto, K. Horikawa, S. Amano, S. Hashimoto, D. Li, K. Imasaki, T. Hayakawa, T. Shizuma, T. Shima, H. Utsunomiya, H. Akimune, Y. Asano, H. Ohkuma, Y. Takagi and T. Mochizuki  
**"Laser Compton Scattering Gamma-ray Source on NewSUBARU"**(oral)  
Int'l Conf. on Ultra-Short Electron & Photon Beams: Techniques and Applications, September 7-11 in Shaanxi-Xi'an, China (2009).
2. Y. Shoji  
**"Transient Bunch Lengthening by a Betatron Motion Along Bending Sections"**  
Int'l Conf. on Ultra-Short Electron & Photon Beams: Techniques and Applications, September 7-11 in Shaanxi-Xi'an, China (2009).
3. Yoshihiko Shoji  
**"Design of a Multi-Element Corrector Magnet for the Storage Ring NewSUBARU"**  
21th Int'l Conf. on Magnet Technology, Oct. 18-23, Hefei, China (2009).
4. S.Amano, K.Horikawa, S.Miyamoto, and T. Mochizuki  
**"Laser-Compton Gamma-Ray Source at Beamline (BL1) in NewSUBARU"**  
10th Int'l Conf. on Synchrotron Radiation Instrumentation (SRI09), Melbourne, #363 (2009).
5. S.Isoda, A.Heya, S.Amano, S.Miyamoto, N.Matsuo and T. Mochizuki,  
**"Low-Temperature Thermal Crystallization of a-Si Film Irradiated by Laser Plasma Soft X-ray"**  
6th Int'l Thin-Film Transistor Conference (ITC'10), (Himeji,2010) , P4.

6. Akinobu Yamaguchi, Keiichi Motoi, Hideki Miyajima, Atsufumi Hirohata, Takehiro Yamaoka, Tsuyoshi Uchiyama, and Yuichi Utsumi  
**“Current manipulation of a vortex confined in a micron-sized Fe19Ni81 disk”**  
 Applied Physics Letters, 95, 122506-112508 (2009).
7. Munehiko Kato, Eric Blasius, Yoshiaki Ukita, Kunihiko Mabuchi, and Yuichi Utsumi  
**“Fabrication of stacked electrodes for multiplex neural interface”**  
 Int’l Conf. on Electronics Packaging 2009 (ICEP2009), pp955-958, (2009), April 14-16, Kyoto, JAPAN
8. Akinobu Yamaguchi, Keiichi Motoi, Hideki Miyajima, Tsuyoshi Uchiyama and Yuichi Utsumi  
**“Permeability and permittivity of single layered Ni81Fe19 micron-scale wire in ferromagnetic resonance state”**  
 IEE Int’l Magnetic Conference (INTERMAG009), May4-8, Sacramento, California, USA (2009)
9. Yuichi Utsumi, Shigeaki Yamamoto, Tomoyuki Kuroki, and Masaaki Okubo  
**”Direct bonding of PFTF sheets assisted by synchrotron radiation induced surface modification”**  
 8th Int’l Workshop on High-Aspect-Ratio Micro-Structure Technology 2009 (HARMST2009), pp151-152, June 25-28, (2009), Saskatoon, Canada
10. Yoshiaki Ukita, Saki Kondo, Chiwa Kataoka, Masahiro Takeo, Seiji Negoro, and Yuichi Utsumi  
**“Immunoassay using poly-tetrafluoroethylene microstructure in organic solvent”**  
 8th Int’l Workshop on High-Aspect-Ratio Micro-Structure Technology 2009 (HARMST2009), pp143-144 , June 25-28, (2009), Saskatoon, Canada
11. Yoshiaki Ukita, Shigeaki Yamamoto, and Yuichi Utsumi  
**“Synchrotron radiation induced smoothing effect of poly-tetrafluoroethylene”**  
 8th Int’l Workshop on High-Aspect-Ratio Micro-Structure Technology 2009 (HARMST2009), pp97-98 , June 25-28, (2009), Saskatoon, Canada
12. Yoshiaki Ukita, and Yuichi Utsumi  
**“Fluoroplastic mold for UV embossing fabricated by synchrotron radiation (SR) direct etching process”**  
 8th Int’l Workshop on High-Aspect-Ratio Micro-Structure Technology 2009 (HARMST2009), pp123-124, June 25-28, (2009), Saskatoon, Canada
13. Tsunemasa Saiki, Katsuhide Okada and Yuichi Utsumi  
**“Micro liquid rotor operated by surface-acoustic-wave”**  
 8th Int’l Workshop on High-Aspect-Ratio Micro-Structure Technology 2009 (HARMST2009), pp233-234 , June 25-28, (2009), Saskatoon, Canada
14. Saki Kondo, Tsukasa Azeta, Yoshiaki Ukita, Tomoya Omukai and Yuichi Utsumi  
**“Vertical Liquid Transportation Through Capillary Bundle Structure Using Centrifugal Force”**  
 8th Int’l Workshop on High-Aspect-Ratio Micro-Structure Technology 2009 (HARMST2009), pp207-208 , June 25-28, (2009), Saskatoon, Canada
15. Yuichi Utsumi  
**“Development of 3D Micro Prototyping Process using Synchrotron Radiation and Its Application to Bio-Micro-Systems”**  
 Int’l Symposium of East Asian Young Scientists Follow-up Program on Environmental- and Bio-Engineering 2009, pp7, September 7-8, (2009), Himeji, Japan.
16. Yuichi Utsumi, Tsukasa Azeta, Saki Kondo, Yoshiaki Ukita, Masahiro Takeo, and Seiji Negoro  
**“High Sensitive Detection of Endocrine Disrupter Using Enzyme Linked Immunosorbent Assay with Vertical Flow Operation”**  
 19th Academic Symposium of MRS-Japan 2009, pp79, September 7-9, (2009), Tokyo, Japan
17. Yoshiaki Ukita, Saki Kondo, Tsukasa Azeta, Chiwa Kataoka, Masahiro Takeo, Seiji Negoro, and Yuichi Utsumi  
**“Enzyme-Linked Immunosorbent Assay using Antibody Bound Fluoroplastic Microstructure”**  
 19th Academic Symposium of MRS-Japan 2009, pp80, September 7-9, (2009), Tokyo, Japan

18. Saki Kondo, oshiaki Ukita, Tsukasa Azeta, and Yuichi Utsumi  
***“Fluid Flow Behaviors of Threedimensional Micro Fluidics Device Using Centrifugal Force”***  
 19th Academic Symposium of MRS-Japan 2009, pp74, September 7-9, (2009), Tokyo, Japan.
19. Tomoya Omukai, Atsushi Kinoshita, Fusao Komada, and Yuichi Utsumi  
***“Usefulness of PMMA Micro 3D Scaffold by Deep X-ray lithography for High Density Cell Culture”***  
 19th Academic Symposium of MRS-Japan 2009, pp73, September7-9, (2009), Tokyo, Japan
20. Munehiko Kato, Mitsuhiro Yoshida, Eric Blasius, Yoshiaki Ukita, Kunihiko Mabuchi, and Yuichi Utsumi  
***“Fabrication of stacked electrodes for multiplex nerval interface”***  
 19th Academic Symposium of MRS-Japan 2009, pp80, September7-9, (2009), Tokyo, Japan
21. Tsunemasa Saiki, Takeshi Komoto, and Yuichi Utsumi  
***“High efficiency Liquid Flow Actuator Operated by Surface Acoustic Waves”***  
 19th Academic Symposium of MRS-Japan 2009, pp74, September7-9, (2009), Tokyo, Japan
22. Tsunemasa Saiki, Katsuhide Okada, and Yuichi Utsumi  
***“High efficiency mixing and pumping of continuous liquid flow using surface acoustic wave”***  
 13th Int’l Conf. on Miniaturized Systems for Chemistry and Life Sciences 2009 (μTAS2009) , pp58-60,  
 Jeju, Korea, November 1-5 (2009) .
23. Yoshiaki Ukita, Saki Kondo, Chiwa Kataoka, Masahiro Takeo, Seiji Negoro, and Yuichi Utsumi  
***“Environmental analysis by using antibody-bound fluoroplastic 3D capillary bundle microstructures”***  
 13th Int’l Conf. on Miniaturized Systems for Chemistry and Life Sciences 2009 (μTAS2009) , pp1931-  
 19332, Jeju, Korea, November 1-5 (2009).
24. Tomoya Omukai, Atsushi Kinoshita, Fusao Komada, and Yuichi Utsumi  
***“High density cell culture using 3D scaffold with capillary bundle structure”***  
 Digest of Papers, 2009 Int’l Microprocess and Nanotechnology Conference (MNC2009), pp40-41,  
 November 16-19, (2009).
25. Tsunemasa Saiki, Katsuhide Okada, and Yuichi Utsumi  
***“High Efficiency Micro Reactor Operated by Surface Acoustic Wave”***  
 Digest of Papers, 2009 Int’l Microprocess and Nanotechnology Conference (MNC2009), pp388-389,  
 November 16-19, (2009).
26. Munehiko Kato, Eric Blasius, Yoshiaki Ukita, Kunihiko Mabuchi, and Yuichi Utsumi  
***“Fabrication of electrodes for multiplex nerval interface”***  
 Digest of Papers, 2009 Int’l Microprocess and Nanotechnology Conference (MNC2009), pp708-709,  
 November 16-19, (2009).
27. Yoshiaki Ukita, Saki Kondo, Chiwa Kataoka, Masahiro Takeo, Seiji Negoro, and Yuichi Utsumi  
***“Immunoassay using antibody-bound poly-tetrafluoroethylene capillary-bundle structure for environmental analysis”***  
 Digest of Papers, 2009 Int’l Microprocess and Nanotechnology Conference (MNC2009), pp712-713,  
 November 16-19, (2009).
28. Shinji Matsui,  
***“Room Temperature Nanoimprint using HSQ and SOG”***  
 The 2nd Asian Symposium on Nanoimprint Lithography (Taipei), Oct.7(2009).
29. Yuji Kang, Makoto Okada, Ken-ichiro Nakamatsu, Kazuhiro Kanda, Yuichi Haruyama, and Shinji Matsui  
***“Effect of UV Irradiation on Sol-Gel ITO Nanopatterns Replicated by Room-Temperature Nanoimprint”***  
 54th Int’l Conf. on Electron, Ion and Photon Beam Technology and Nanofabrication(EIPBN2009), (Florida,  
 USA), May 28 (2009).
30. Makoto Okada, Yuji Kang, Ken-ichiro Nakamatsu, Masayuki Iwasa, Kazuhiro Kanda, Yuichi Haruyama, and  
 Shinji Matsui  
***“Characterization of Nanoimprint Resin and Antisticking Layer by Scanning Probe Microscopy”***  
 The 27th Int’l Conf. of Photopolymer Science and Technology (Chiba), Jul.2(2009).

31. Yuji Kang, Makoto Okada, Ken-ichiro Nakamatsu, Kazuhiro Kanda, Yuichi Haruyama, and Shinji Matsui, ***“Room-temperature nanoimprint using sol-gel ITO film”***  
27th Int’l Conf. of Photopolymer Science and Technology (Chiba), Jul.2(2009).
32. Yuji Kang, Makoto Okada, Ken-ichiro Nakamatsu, Kazuhiro Kanda, Yuichi Haruyama, and Shinji Matsui, ***“Room-temperature nanoimprint using liquid-phase hydrogen silsesquioxane with PDMS mold”***  
27th Int’l Conf. of Photopolymer Science and Technology (Chiba), Jul.2(2009).
33. Makoto Okada, Shinichi Nakano, Shinichiro Kawahara, and Shinji Matsui  
***“Nanoimprint using side chain crystalline polymer”***  
22nd Int’l Microprocesses and Nanotechnology Conference (MNC2009), (Hokkaido, Sapporo), Nov.17(2009).
34. Makoto Okada, Ken-ichiro Nakamatsu, Yuji Kang, Yuichi Haruyama, Kazuhiro Kanda, and Shinji Matsui  
***“Characteristics of Antisticking Layer Formed by Plasma Irradiation using Mixture Gas with CHF<sub>3</sub> and O<sub>2</sub> for Nanoimprint”***  
54th Int’l Conf. on Electron, Ion and Photon Beam Technology and Nanofabrication(EIPBN2009), (Florida, USA), May.27(2009).
35. Makoto Okada, Takshi Kishiro, Kori Yanagihara, Masahi Ataka, Norimichi Anazawa, and Shinji Matsui  
***“Fabrication of Large Area Mold by Electron Beam Stepper”***  
35th Int’l Conference on Micro and Nano Engineering(MNE2009), (Ghent, Belgium), Sep.29(2009).
36. Makoto Okada, Mayuko Shibata, Kazuhiro Kanda, Yuichi Haruyama, Yoshihiko Hirai, and Shinji Matsui  
***“Cross-sectional Observation of Nanoimprint Resins Filled in SiO<sub>2</sub>/Si Mold Pattern by Scanning Electron Microscopy”***  
35th Int’l Conf. on Micro and Nano Engineering(MNE2009), (Ghent, Belgium), Sep.30(2009).
37. Makoto Okada, Yuji Kang, Takahiro Nakayama, Yuichi Haruyama, Kazuhiro Kanda, and Sshinji Matsui  
***“Direct Patterning on Sol-Gel Low-k Porous Silica by Nanoimprint”***  
Asian Symposium on Nano Imprint Lithography 2009 (ASNIL2009), (Taipei, Taiwan), Oct.7(2009).
38. Makoto Okada, Shinichi Nakano, Shinichiro Kawahara, and S. Matsui  
***“Characteristics of side Chain Crystalline Polymer in Nanoimprint”***  
Asian Symposium on Nano Imprint Lithography 2009 (ASNIL2009), (Taipei, Taiwan), Oct.7(2009).
39. Yuji Kang, Makoto Okada, Kazuhiro Kanda, Yuichi Haruyama, and Shinji Matsui  
***“Room-temperature nanoimprint using liquid-phase HSQ with h-PDMS mold”***  
Asian Symposium on Nano Imprint Lithography 2009 (ASNIL2009), (Taipei, Taiwan), Oct.7(2009).
40. Yasuki Nakai, Yuji Kang, Makoto Okada, Yuichi Haruyama, Kazuhiro Kanda, and Shinji Matsui  
***“Thermal durability of antisticking layer formed by fluorinated-trichlorosilane in nanoimprint”***  
Asian Symposium on Nano Imprint Lithography 2009 (ASNIL2009), (Taipei, Taiwan), Oct.7(2009).
41. Shinya Omoto, Makoto Okada, Yuji Kang, Kazuhiro Kanda, Yuichi Haruyama, and Shinji Matsui  
***“UV nanoimprinting using a template with HSQ patterned fabricated by electron beam lithography”***  
Asian Symposium on Nano Imprint Lithography 2009 (ASNIL2009), (Taipei, Taiwan), Oct.7(2009).
42. Makoto Okada, Hiroto Miyake, Kei Kuramoto, Masayuki Iwasa, Yuichi Haruyama, Kazuhiro Kanda, and Shinji Matsui  
***“Adhesion Evaluation of Radical-, Cation-, and Hybrid-UV Nanoimprint Resins”***  
8th Int’l Conf. on Nanoimprint and Nanoprint Technology 2009 (NNT2009), (California, USA), Nov.12(2009).
43. Yuji Kang, Makoto Okada, Chiaki Minari, Kazuhiro Kanda, Yuichi Haruyama, and Shinji Matsui  
***“Nanostructure fabrication by room-temperature nanoimprint using liquid-phase HSQ with PDMS mold”***  
8th Int’l Conf. on Nanoimprint and Nanoprint Technology 2009 (NNT2009), (California, USA), Nov.12(2009).

44. Yuji Kang, Makoto Okada, Kazuhiro Kanda, Yuichi Haruyama, and Shinji Matsui  
**“Large area Room-Temperature Nanoimprint using Liquid-Phase HSQ with PDMS mold”**  
 American Vacuum Society 56th international symposium & exhibition, (California, USA), Nov.10(2009).
45. Makoto Okada, Yuji Kang, Takahiro Nakayama, Yuichi Haruyama, Kazuhiro Kanda, and Shinji Matsui  
**“Nanoimprint on Sol-Gel Low-k Porous Silica”**  
 22nd Int’l Microprocesses and Nanotechnology Conference (MNC2009), (Hokkaido, Sapporo),  
 Nov.19(2009).
46. Yuji Kang, Makoto Okada, Chiaki Minari, Kazuhiro Kanda, Yuichi Haruyama, and Shinji Matsui  
**“Room-temperautre nanoimprint using liquid-phase HSQ with h-PDMS mold”**  
 22nd Int’l Microprocesses and Nanotechnology Conference (MNC2009), (Hokkaido, Sapporo),  
 Nov.19(2009).
47. Kazuhiro Kanda, Makoto Okada, Yuji Kang, Tsuneo Suzuki, and Shinji Matsui,  
**“Departure Process of Ga from DLC Films Fabricated using Ga Focused Ion Beam Assisted Deposition  
 by Heat Treatment”**  
 16th Int’l Conf. on Surface Modification of Materials by Ion Beams (SMMIB2009), (Odaiba, Tokyo) Sep. 13  
 - 18, (2009).
48. Kazuhiro Kanda, Makoto Okada, Yuji Kang, Masahito Niibe, Tsuneo Suzuki, and Shinji Matsui,  
**“Structural Changes in the DLC Films Fabricated using Ga Focused Ion Beam Assisted Deposition by  
 Heat Treatment”**  
 22nd Int’l Microprocesses and Nanotechnology Conference (MNC2009), (Hokkaido, Sapporo), Nov.19,  
 (2009).
49. T. Kaito, H. Oba, Y. Sugiyama, A. Yasaka, J. Fujita, T. Suzuki, K. Kanda, and S. Matsui,  
**“Deposition yield and physical property of carbon deposited by FIB-CVD”**  
 22nd Int’l Microprocesses and Nanotechnology Conference (MNC2009), (Hokkaido, Sapporo), Nov.19,  
 (2009).
50. Kazuhiro Kanda, Makoto Okada, Yuji Kang, Masahito Niibe, and Shinji. Matsui,  
**“NEXAFS study of the annealing effect on the DLC films fabricated using Ga focused ion beam assisted  
 deposition”**  
 23<sup>rd</sup> Diamond Symposium, (Tsudanuma, Chiba), Nov. 18-20 (2009).
51. Y. Haruyama, M. Tagawa, K. Yokota, and S. Matsui  
**“NEXAFS study on annealing temperature dependence of hydrogenated amorphous carbon films”**  
 14th Int’l Conf. on Xay Absorption Fine Structure (XAFS 2009), July, PS1.36, Camerino, Italy
52. Y. Haruyama, Y. Teraoka, and S. Matsui  
**“Electronic structure near the surface region in the ternary transition metal alloy  $Ti_{35}V_{25}Cr_{40}$  by  
 photoemission spectroscopy”**  
 The 11-th Int’l Conference on Electronic Spectroscopy & Structure (ICESS11), 6AP09, October, Nara, Japan
53. M. Niibe, K. Koida, T. Nakayama, S. Terashima, A. Miyake, H. Kubo, Y. Kakutani, S. Matsunari, T. Aoki, S.  
 Kawata  
**“Inhibition of deposition and removal of carbon films on the multilayer surface by EUV irradiation in the  
 presence of water vapor, oxygen and ozone gases”**  
 2009 Int’l Symposium Extreme Ultraviolet Lithography, Prague, Czech Republic, Oct. 19-Oct. 21 (2009).
54. K. Kanda, M. Okada, Y. Kang, M. Niibe, S. Matsui:  
**“Electronic structure near the surface region in the ternary transition metal alloy  $Ti_{35}V_{25}Cr_{40}$  by  
 photoemission spectroscopy”**  
 23<sup>rd</sup> Diamond Symposium (2009).
55. Masahito Niibe, Masanori Kayahara, and Shozo Inoue  
**“Electronic structure and photocatalytic activity of titania thin films prepared by magnetron sputtering  
 with glancing angle deposition technique”**  
 11<sup>th</sup> Int’l. Conf. Electron Spectroscopy and Structure, Nara, Japan, Oct. 6-10 (2009).

56. R. Kawakami, T. Inaoka, K. Tominaga, M. Niibe, T. Mukai, A. Takeichi and T. Fukudome:  
**"Synergy Effect of Xenon Plasma Ions and Ultraviolet Lights on GaN Etch Surface Damage and Modification"**  
 16th Int'l Conf. on Surface Modification of Materials by Ion Beams (SMMIB2009), Tokyo, Sept. 13-18 (2009).
57. Masahito Niibe and Keigo Koida:  
**"Competitive reactions of carbon deposition and oxidation on the surface of Mo/Si multilayer mirrors by EUV irradiation"**  
 SPIE Europe 2009, Prague, Czech Republic, 20-23 Apr. (2009).
58. Yasuyuki Fukushima, Takeo Watanabe, Testuo Harada, and Hiroo Kinoshita  
**"The Photo-absorption Coefficient Measurement of EUV Resist"**  
 26<sup>th</sup> Int'l Conf. of Photopolymer Science and Technology, Chiba, Japan, June 30- July 3 (2009).
59. Takeo Watanabe and Hiroo Kinoshita  
**"Actinic Defect Inspection Technology for EUVL Masks" (Panelist, Invited Panelist)**  
 2009 Int'l Workshop on EUV Lithography, Waikiki, Hawaii, USA, Jul. 13-17 (2009).
60. Hiroo Kinoshita, Nagata Yutaka, Tetsuo Harada, and Takeo Watanabe  
**"Development of Ultra-Fine Structure Metrology System Using Coherent EUV Source"**  
 2009 Int'l Workshop on EUV Lithography, Waikiki, Hawaii, USA, Jul. 13-17 (2009).
61. Hiroo Kinoshita, Yoshito Kamaji, Kei Takase, Takashi Sugiyama, Toshiyuki Uno, Tetsuo Harada, and Takeo Watanabe  
**"Study of Critical Dimensions of Printable Phase Defects Using an Extreme Ultraviolet microscope"**  
 2009 Int'l Workshop on EUV Lithography, Waikiki, Hawaii, USA, Jul. 13-17 (2009).
62. Takeo Watanabe, Tae Geun Kim, Tetsuo Harada, Yasuyuki Fukushima, and Hiroo Kinoshita  
**"EUV Interference Lithography in NewSUBARU"**  
 2009 Int'l Workshop on EUV Lithography, Waikiki, Hawaii, USA, Jul. 13-17 (2009).
63. Daiju Shiono, Hideo Hada, Kazufumi Sato, Yasuyuki Fukushima, Takeo Watanabe and Hiroo Kinoshita  
**"Decomposition and Roughness Analysis of Chemically Amplified Molecular Resist for Reducing LWR"**  
 21<sup>th</sup> Microprocesses and Nanotechnology Conference, Sapporo, Hokkaido, Japan, Nov.16-19, 2009.
64. I. Aratani, S. Matsunaga, T. Kajiyashiki, T. Watanabe, and H. Kinoshita  
**"Evaluation of Novel Resist Materials for EUV Lithography"**  
 SPIE's 34<sup>th</sup> Annual Int'l Symposium on Advanced Lithography, San Jose, CA, USA, Feb. 22 - Feb. 27 (2009).
65. D. Shiono, T. Watanabe, and H. Kinoshita  
**"Decomposition analysis of molecular resists to further CD control"**  
 SPIE's 34<sup>th</sup> Annual Int'l Symposium on Advanced Lithography, San Jose, CA, USA, Feb. 22 - Feb. 27, 2009.
66. Tetsuo Harada, Junki Kishimoto, Takeo Watanabe, Hiroo Kinoshita, and Dong Gun Lee  
**"Mask observation results using coherent EUV scattering microscope at NewSUBARU"**  
 The 53rd Int'l Conference on Electron, Ion and Photon Beam technology and Nanofabrication, Marco Island, FL, USA, May 25-31, 2009.
67. Takeo Watanabe, Yasuyuki Fukushima, Tetsuo Harada, and Hiroo Kinoshita  
**"Resist Transmission Measurement using EUV Light"**  
 2009 Int'l Workshop on EUV Lithography, Waikiki, Hawaii, USA, Jul. 13-17, 2009.
68. H. Kinoshita, N. Yutaka, T. Harada, T. Watanabe, D.Lee  
**"Development of Ultra-Fine Structure Metrology System using Coherent EUV Source"**

- 8<sup>th</sup> EUVL Int'l Symposium 2009, Prague, Oct. 18-21, 2009.
69. T. Watanabe, Y. Fukushima, N. Sakagami, Y. Kamaji, T. Iguchi, Y. Yamaguchi, M. Tada, T. Harada, T. Mochizuki, H. Kinoshita  
**“EUV Interference Lithography in New SUBARU”**  
 8<sup>th</sup> EUVL Int'l Symposium 2009, Prague, Oct. 18-21, 2009.
  70. Y. Fukushima, T. Watanabe, T. Harada, H. Kinoshita  
**“Resist Transmittance Measurement using EUV Light”**  
 8<sup>th</sup> EUVL Int'l Symposium 2009, Prague, Oct. 18-21, 2009.
  71. N. Sakagami, Y. Fukushima, Y. Kamaji, T. Iguchi, Y. Yamaguchi, M. Tada, T. Harada, T. Watanabe and H. Kinoshita  
**“Development of the Extreme Ultraviolet Interference Lithography System”**  
 21<sup>th</sup> Microprocesses and Nanotechnology Conference, Sapporo, Hokkaido, Japan, Nov. 16-19, 2009.
  72. Daiji Noda, Hiroshi Tsujii, Naoki Takahashi, and Tadashi Hattori  
**“Fabrication of High Precision X-ray Mask for X-ray Grating of X-ray Talbot Interferometer”**  
 8th Int'l Workshop on High-Aspect-Ratio Micro-Structure Technology (HARMST 2009), Saskatoon, Canada, June 25-28, 2009
  88. Naoki Takahashi, Hiroshi Tsujii, Megumi Katori, Kenji Yamashita, Daiji Noda, and Tadashi Hattori  
**“Fabrication of X-rays Mask with Carbon Membrane for Diffraction Gratings”**  
 8th Int'l Workshop on High-Aspect-Ratio Micro-Structure Technology (HARMST 2009), Saskatoon, Canada, June 25-28, 2009
  89. Hiroaki Miyake, Kazufumi Nishimoto, Satoshi Nishida, Daiji Noda, and Tadashi Hattori  
**“Fabrication of Micro Capacitive Inclination Sensor by Resin Molding”**  
 8th Int'l Workshop on High-Aspect-Ratio Micro-Structure Technology (HARMST 2009), Saskatoon, Canada, June 25-28, 2009
  90. Yashitaka Sawa, Kenji Yamashita, Takeshi Kitadani, Daiji Noda, and Tadashi Hattori  
**“Fabrication of High Hardness Ni Mold with Electroless Nickel-Boron Thin Layer”**  
 8th Int'l Workshop on High-Aspect-Ratio Micro-Structure Technology (HARMST 2009), Saskatoon, Canada, June 25-28, 2009
  91. Daiji Noda, Masaru Setomoto, Yuki Kobayashi, and Tadashi Hattori  
**“Fabrication of Microcoils with Narrow and High Aspect Ratio Coil Lines”**  
 8th Int'l Workshop on High-Aspect-Ratio Micro-Structure Technology (HARMST 2009), Saskatoon, Canada, June 25-28, 2009
  92. Yuta Okayama, Kenji Yamashita, Yoshitaka Sawa, Daiji Noda, and Tadashi Hattori  
**“Fabrication of Ultraviolet Range Light Guide Plate”**  
 8th Int'l Workshop on High-Aspect-Ratio Micro-Structure Technology (HARMST 2009), Saskatoon, Canada, June 25-28, 2009
  93. Daiji Noda, Masaru Setomoto, and Tadashi Hattori  
**“Fabrication of High Aspect Ratio Microcoils for Electromagnetic Actuators”**  
 2009 IEEE Int'l Symposium on Micro-Nano Mechatronics and Human Science (MHS 2009), Nagoya, Japan, November 8-11, 2009
  94. Takaya Fujimoto, Yuta Okayama, Kenji Yamashita, Satoshi Nishida, Yoshitaka Sawa, Daiji Noda, and Tadashi Hattori  
**“Examination of High Luminance Light Guide Plate by Accumulating Method”**  
 2009 IEEE Int'l Symposium on Micro-Nano Mechatronics and Human Science (MHS 2009), Nagoya, Japan, November 8-11, 2009
  95. Daiji Noda and Tadashi Hattori  
**“Development of a New Nano-Micro Solid Processing Technology Based on a LIGA Process and a Next-**

*Generatic Micro Actuator*"

3rd Int'l Symposium on Next-Generation Actuators Leading Breakthroughs, Tokyo, Japan, January 25-26, 2010

### **(3) Awards**

1. Professor Hiroo Kinoshita  
*"Lifetime Achievement Award"*  
"2009 International Workshop on EUV Lithography", Sheraton Waikiki Beach, Honolulu, Hawaii, USA, July 15, 2009.



# **Academic Degrees**



## Academic Degrees

<b>Degree</b>	<b>Name</b>	<b>Doctor's Thesis</b>
Doctor of Engineering	<b>Akihisa Nagano</b> (University of Hyogo)	<i>Studies on laser-produced plasma EUV source by using Lithium and Xenon</i>
Doctor of Engineering	<b>Yoshitaka Sawa</b> (University of Hyogo)	<i>Fabrication of High Hardness Electroformed Micro Mold by LIGA Process, and Research on the Its Application</i>

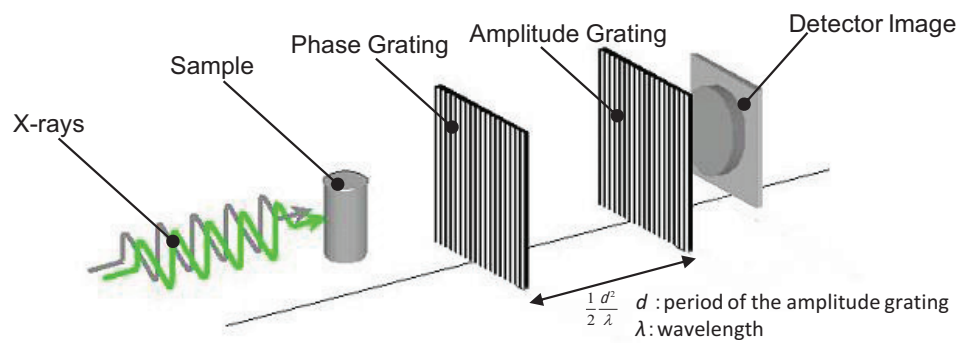
<b>Degree</b>	<b>Name</b>	<b>Master's Thesis</b>
Master of Engineering	<b>Tomoaki Inoue</b> (University of Hyogo)	<i>Study on a high-repetition-rate pulse laser plasma soft x-ray source system and its applications</i>
Master of Engineering	<b>Saki Kondo</b> (University of Hyogo)	<i>Proposal of 3D Micro-chemical Chip and Its Application to ELISA</i>
Master of Engineering	<b>Tomoya Omukai</b> (University of Hyogo)	<i>High Density Cell Cultivation of Hep G2 Using High Aspect Ratio Micro Scaffold</i>
Master of Engineering	<b>Munehiko Kato</b> (University of Hyogo)	<i>Investigation of fabrication Process of Flexible Electrode for Neural Interface</i>
Master of Engineering	<b>Naoki Sakagami</b> (University of Hyogo)	<i>Development of EUV Interference Lithographic Exposure Tool and Fine Pattern Replication</i>
Master of Engineering	<b>Yoshito Kamaji</b> (University of Hyogo)	<i>Definition of Pit-Type Phase-Defects Criteria between Printable and Non Printable of EUV Mask</i>
Master of Engineering	<b>Kei Takase</b> (University of Hyogo)	<i>Refinement of EUV Mask Defects Observation Utilizing EUV Microscope</i>
Master of Engineering	<b>Yuta Okayama</b> (University of Hyogo)	<i>Fabrication of High Luminance Ultraviolet Range Light Guide Plate</i>
Master of Engineering	<b>Masaru Setomoto</b> (University of Hyogo)	<i>Fabrication and Estimation of Microcoil Using X-ray Lithography</i>
Master of Engineering	<b>Naoki Takahashi</b> (University of Hyogo)	<i>Fabrication of Diffraction Gratings for Talbot Interferometer Using New Carbon X-ray Mask</i>
Master of Engineering	<b>Hiroaki Miyake</b> (University of Hyogo)	<i>Fabrication and Estimation of Micro Capacitive Inclination Sensors by Resin Molding</i>

## Cover photograph

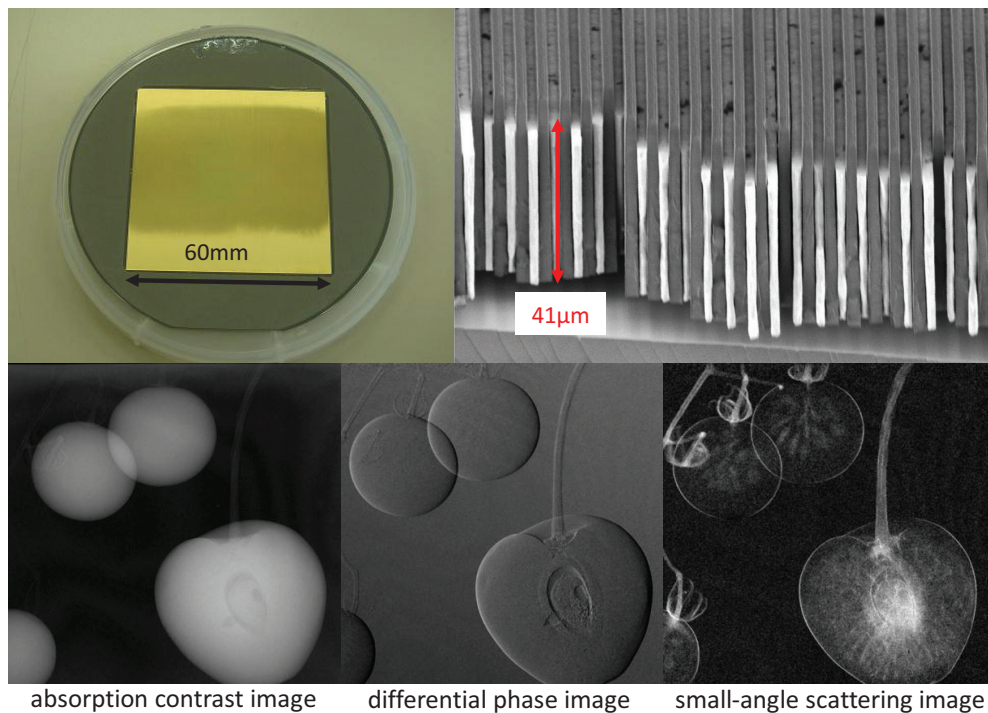
### X-ray Talbot-Lau interferometry Imaging

The cover photograph shows the X-ray grating for Talbot-Lau interferometry and images taken by the system. X-ray Talbot-Lau interferometry system for X-ray phase imaging is shown below. The system was constructed using X-ray grating of a gold pattern 5.3  $\mu\text{m}$  pitch and 40  $\mu\text{m}$  in height. This high aspect ratio X-ray grating is fabricated by X-ray lithography on the BL02 and gold electroforming technique.

Cherry and micro tomato images were obtained in this phase imaging method by Konica Minolta Medical & Graphic, Inc. These results suggest that X-ray Talbot-Lau interferometry would be a promising tool in detecting soft tissues in the human body. This study is supported by the project "Development of Systems and Technology for Advanced Measurement and Analysis" of JST.



X-ray Talbot interferometry



## **LASTI Annual Report 2009**      **Vol.10(2009)**

---

2010.8 Published by

Laboratory of Advanced Science and Technology for Industry, University of Hyogo  
3-1-2 Kouto, Kamigori-cho, Ako-gun, Hyogo, 678-1205 JAPAN  
TEL: +81-791-58-0249 / FAX: +81-791-58-0242

***Editorial board***

**Editor in Chief**  
**Editors**

**Shuji Miyamoto**  
**Masahito Niibe**  
**Yoshihiko Shoji**  
**Kazuhiro Kanda**  
**Yuichi Utsumi**  
**Takeo Watanabe**

---